

TALLINN UNIVERSITY OF TECHNOLOGY
DOCTORAL THESIS
29/2020

Combination of SLM-SPS Approaches for Tribological, Antibacterial and Biomaterial Applications

RAMIN RAHMANI AHRANJANI



TALLINN UNIVERSITY OF TECHNOLOGY

School of Engineering

Department of Mechanical and Industrial Engineering

This dissertation was accepted for the defence of the degree 21/04/2020

Supervisor: Dr. Maksim Antonov
Department of Mechanical and Industrial Engineering
School of Engineering, Tallinn University of Technology
Tallinn, Estonia

Co-supervisor: Dr. Lauri Kollo
Department of Mechanical and Industrial Engineering
School of Engineering, Tallinn University of Technology
Tallinn, Estonia

Opponents: Prof. Michael Gasik
Department of Chemical and Metallurgical Engineering
School of Chemical Engineering, Aalto University
Espoo, Finland

Assoc. Prof. Audrius Žunda
Institute of Power and Transport Machinery Engineering
Vytautas Magnus University
Kaunas, Lithuania

Dr. Sergei Vlassov
Faculty of Science and Technology
Institute of Physics, University of Tartu
Tartu, Estonia

Defence of the thesis: 26/08/2020, Tallinn

Declaration:

Hereby I declare that this doctoral thesis, my original investigation and achievement, submitted for the doctoral degree at Tallinn University of Technology has not been submitted for doctoral or equivalent academic degree.

Ramin Rahmani Ahranjani

signature



European Union
European Regional
Development Fund



Investing
in your future

Copyright: Ramin Rahmani Ahranjani, 2020

ISSN 2585-6898 (publication)

ISBN 978-9949-83-570-6 (publication)

ISSN 2585-6901 (PDF)

ISBN 978-9949-83-571-3 (PDF)

Printed by Koopia Niini & Rauam

TALLINNA TEHNIKAÜLIKOOL
DOKTORITÖÖ
29/2020

**Kombineeritud SLM-SPS meetod
triboloogiliste, antibakteriaalsete ja
biosobivate materjalide valmistamiseks**

RAMIN RAHMANI AHRANJANI



Contents

List of Publications	7
Author's contribution to the publications.....	8
Introduction	9
Approbation of the research outcomes.....	10
List of abbreviations	11
1 State of the art of SLM and SPS processes	12
1.1 SLM process	12
1.2 SPS process	12
1.3 Ti6Al4V and 316L metallic powders.....	13
1.4 Diamond particles	14
1.5 Cellular lattice structures.....	15
1.6 Objectives of the study	16
2 Materials, methods and lattice printing.....	17
2.1 Fabrication of gradient structure.....	17
2.2 Diamond-metal composite printing.....	19
2.3 Post-processing procedures.....	20
2.4 Unit cell design.....	22
3 Modelling and simulation study.....	24
3.1 Design of gradient structure	24
3.2 CAD modelling of gradient structure	25
3.3 Simulation of compression test	26
3.4 Simulation of impact test.....	27
3.5 Simulation of abrasion test.....	28
4 Results and discussion.....	31
4.1 Antibacterial application.....	31
4.1.1 Structural study	31
4.1.2 Antibacterial assay.....	31
4.1.3 Prospective applications.....	32
4.2 Biomedical application.....	33
4.3 Tunneling study.....	34
4.3.1 Overview of TBM components manufactured by 3D printing.....	34
4.3.2 Mapping of impact-abrasive wear performance.....	35
4.4 Tribology study	36
Conclusions	38
Future works	39

References.....	40
Acknowledgment	47
Abstract	48
Lühikokkuvõte.....	49
Appendix	51
Curriculum Vitae	134
Elulookirjeldus.....	135

List of Publications

The list of author's publications, on the basis of which thesis has been prepared:

- I. **R. Rahmani**, M. Brojan, M. Antonov, K. G. Prashanth, Perspectives of metal-diamond composites additive manufacturing using SLM-SPS and other techniques for increased wear-impact resistance, *International Journal of Refractory Metals and Hard Materials* 88 (2020) 1-13.
- II. **R. Rahmani**, M. Rosenberg, A. Ivask, L. Kollo, Comparison of mechanical and antibacterial properties of TiO₂/Ag ceramics and Ti6Al4V-TiO₂/Ag composite materials using combining SLM-SPS techniques, *Metals* 9 (2019) 1-13.
- III. **R. Rahmani**, M. Antonov, L. Kollo, Y. Holovenko, P. K. Gokuldoss, Mechanical Behavior of Ti6Al4V Scaffolds Filled with CaSiO₃ for Implant Applications, *Applied Sciences* 9 (2019) 1-11.
- IV. **R. Rahmani**, M. Antonov, L. Kollo, Selective Laser Melting of Diamond-Containing or Postnitrided Materials Intended for Impact-Abrasive Conditions: Experimental and Analytical Study, *Advances in Materials Science and Engineering* (2019) 1-11.
- V. **R. Rahmani**, M. Antonov, L. Kollo, Wear Resistance of (Diamond-Ni)-Ti6Al4V Gradient Materials Prepared by Combined Selective Laser Melting and Spark Plasma Sintering Techniques, *Advances in Tribology* (2019) 1-12.
- VI. **R. Rahmani**, M. Antonov, N. Kamboj, Modelling of impact-abrasive wear of ceramic, metallic, and composite materials, *Proceedings of the Estonian Academy of Sciences* 68 (2019) 191-197.

Author's contribution to the publications

Author's work/contribution to the papers in this thesis is:

- I. First and corresponding author. Modelling and production of 3D printed gradient lattice structures. Simulation by Comsol software. Polishing and coating post-processing. Manuscript preparation.
- II. First and corresponding author. Modelling and production of 3D printed lattice structures. Simulation by Ansys software. Sintering of antibacterial samples. Manuscript preparation.
- III. First and corresponding author. Modelling and production of 3D printed lattice structures. Modelling by SolidWorks and simulation by Ansys software. Analysis of mechanical properties. Preparation of biomedical samples. Manuscript preparation.
- IV. First and corresponding author. Modelling and production of 3D printed gradient lattice structures. Analysis of numerical results. Simulation by SolidWorks/Ansys software. Manuscript preparation.
- V. First and corresponding author. Design of 3D printed lattice structures. Modelling by SolidWorks and simulation by Ansys software. Mechanical Characterization. Manuscript preparation.
- VI. First and corresponding author. Modelling of 3D printed lattice structures and composites. Analysis of numerical results. Simulation by SolidWorks/Ansys software. Manuscript preparation.

Introduction

Rapid development of additive manufacturing (AM) in the recent decade is tangible due to the ability to produce complex geometrical configuration from lattice structure to scaffolds, triply periodic minimal surface (TPMS) and bulk solid shapes. AM using powder bed is an incremental layer-upon-layer and/or point-by-point manufacturing and this technology commonly uses spherical powders as feedstock, which is selectively melted by a focused laser source and consolidated in-situ. AM has been widely studied in different industries, crucial constructions, theoretical comprehensions and for biomedical applications [1-3].

Metallic cellular lattice structures with the purpose of combination with proper ceramics can be produced and the result, which is refractory cermet, can be applied for industrial (tunneling and mining), biomedical (bone implants), antibacterial, aerospace and tribological applications. AISI 316L stainless steel, Ti6Al4V titanium and AlSi10Mg aluminum are three highly demanded metallic lattice structures due to their applicability and availability, ductility, corrosion resistance (316L), strength to weight ratio (Ti6Al4V), and lightness (AlSi10Mg). Functionally Graded Lattice (FGL) enables an exceptional capability to substitute multi-layer structures (including porous or ceramic materials) instead of uniform solid materials; however, it is necessary to survey their manufacturability as well as mechanical properties [4-6].

Presence of selective laser melting (SLM) and spark plasma sintering (SPS) devices in Tallinn University of Technology (TalTech) was a precious opportunity to develop research in the above fields. Due to low manufacturing speed of SLM and quite high expense procedure of SPS methods, we need to focus on special fields or alloys, such as in vivo medium, bionic components for aerospace, complex TPMS surfaces, and medical equipment. Combination of aforementioned approaches with the help of extra post-processing procedures (including carburizing, nitriding, coating, blasting, and polishing) enables us to manufacture biocompatible samples with high densification, wear resistance, and lifetime [7, 8]. The central role of strut diameter and unit cell size of the lattice structures in all above applications is inevitable. For this reason, the present thesis focused on the development of lattice structures such as matrix in metal-ceramic composition and post-processing procedures to improve mechanical properties, and their simulations to decrease the production costs [9, 10].

In the present thesis, SLM and SPS techniques combined toward the optimization of wear and impact resistant composite materials with functionally graded structures due to their novelties, desired distribution of metal and ceramic in the longitudinal or circumferential directions, and almost full densification has been applied as an outcome of the modern powder metallurgy field. 3D printing of gradient structure along with post-processing procedures (nitriding, coating, blasting, filling, surface covering, and hard-materials adding to lattice structures) are introduced in tribological, antibacterial, biomedical fields and related papers. Coupled experimental and analytical results show that the FGL structure allows a more accurate and favourable distribution of diamond particles across the structure and our finite element simulations showed increased ductility and impact energy absorption.

Approbation of the research outcomes

- I. **R. Rahmani**, M. Antonov, L. Kollo, Modelling of impact-abrasive wear processes and materials. 45th Leeds-Lyon Symposium on Tribology, 4-7 September 2018, Leeds Trinity University, Leeds, United Kingdom.
- II. **R. Rahmani**, M. Antonov, L. Kollo, Wear simulation of hybrid composite obtained by combined selective laser melting and spark plasma sintering technologies. The 6th Asia International Conference on Tribology, 17-20 September 2018, University of Malaya, Kuala Lumpur, Malaysia.
- III. **R. Rahmani**, M. Antonov, L. Kollo, 3D printed cermet hand watch produced by combined SLM and SPS approaches, YCAM 2018 symposium and forum on Additive Manufacturing of Ceramics, 3-4 May 2018, University of Padua, Italy.
- IV. **R. Rahmani**, M. Antonov, 3D printing technology to address tribological applications. Second Asia-Pacific International Conference on Additive Manufacturing (APICAM 2019), 30th June - 3rd July 2019, RMIT University, Melbourne, Australia.
- V. **R. Rahmani**, M. Antonov, L. Kollo, Modelling of Ti6Al4V triply periodic minimal surface manufactured via selective laser melting for biomaterial application. The EPMA journal publication, EURO PM2019, 13-16 October 2019, Maastricht, the Netherlands.
- VI. **R. Rahmani**, M. Antonov, N. Kumar, Modelling of impact-abrasive wear of ceramic, metallic and composite materials, 23-26 April 2019, Modern Materials and Manufacturing (MMM 2019), Tallinn University of Technology, Estonia.

List of abbreviations

AM	Additive Manufacturing
AP	Armour Piercing
BCC	Body-centered cubic
CAD	Computer-aided Design
CVD	Chemical Vapor Deposition
DGD	Deep Geothermal Drilling
EDS	Energy-dispersive Spectroscopy
ET	Exposure Time
FCC	Face-centered cubic
FE	Finite Element
FGL	Functionally Graded Lattice
IATD	Impact Abrasive Tribo-Device
LC	Laser Current
MMC	Metal Matrix Composite
OSP	Optical Surface Profiler
PCD	Polycrystalline Diamond
PD	Point Distance
SEM	Scanning Electron Microscopy
SLM	Selective Laser Melting
SPS	Spark Plasma Sintering
TaTech	Tallinn University of Technology
TBM	Tunnel Boring Machine
TPMS	Triply Periodic Minimal Surface
VF	Volume Fraction
VFN	Vacuum Furnace Nitriding
XRD	X-ray diffraction

1 State of the art of SLM and SPS processes

Additive manufacturing (AM) has an enormous potential to develop new classes of materials that are macro- and microstructures engineered for specific applications and conditions. Combining selective laser melting (SLM) and spark plasma sintering (SPS) empowers the production of metal, ceramic or cermet composites using gradient structures with continuous metallic lattices for improved ductility and filled hard materials for hardness [11, 12]. The drag bits for deep geothermal drilling (DGD) or the tunnel boring device (TBM) [13, 14] in hard medium impact/abrasive wear is an excellent example of application to assess the potential of AM methods specifically and 3D printing of metallic and composite materials with diamond particles or tungsten carbide inclusions [15, 16].

1.1 SLM process

SLM is a rapid prototyping technology based on the powder bed fusion process with the high heating/cooling rate that allows the manufacture of complex parts/assemblies directly from computer-aided design (CAD) models to final production. The feeder piston is used to supply agglomerated powders in front of a powder recoater that sweeps the powder on the building area to form a thin uniform layer. The minimal possible thickness of the spread layer depends on the flowability/sphericity of powder, and machine settings and precision. SLM process is shown schematically in Fig. 1.1. The laser then melts the powder on the fabricating area to form a solid object. With this system, the objects are built layer-upon-layer on, e.g., titanium or steel platform with the help of a servomotor driven elevator that moves downwards by a distance equal to the layer thickness and this is repeated after every wiping and melting sequence. The process is carried out in an argon protective environment with a pressure usually higher than 6 mbar and an oxygen level less than 0.50 % [17]. Powders are consolidated on previous layers as a solid part with the defined thickness, between 0.25 to 0.50 μm for Realizer SLM50 [18]. Unmelted/nonconsolidated powders inside or outside the platform wiped out during the printing or after finishing the job can be sieved, which is a benefit of the AM technology regarding the utilization of high efficiency powder [19]. Another advantage of SLM is the capability to use a wide range of metals from Ti-, Fe-, Al-, Ni-, Co- to Cu-based powders [20].

1.2 SPS process

The SPS process is a modern powder metallurgy consolidation technique with simultaneous application of a low voltage, high pulse current, and uniaxial pressure-assisted punch electrodes [21]. The key advantages of this sintering method over the hot isostatic pressing (HIP) method include high densification level obtained in a short time and a wide range of sintering temperature (up to 2000 °C), fast heating rate (up to 1000 °C/min) compared to the conventional powder metallurgy methods (Fig. 1.2). The electrical direct current pulsed in a vacuum chamber generates the spark discharge, passing through graphite mold and powder particles [22, 23]. The pressure is controlled by a hydraulic system manipulating the piston, thermocouple control (TC) or pyrometer control (PC) is applied for temperature control [24]. SPS is developed for the consolidation of a wide range of metals, ceramics, cermets, oxides and composites in different dimensions (depends on the mold shape).

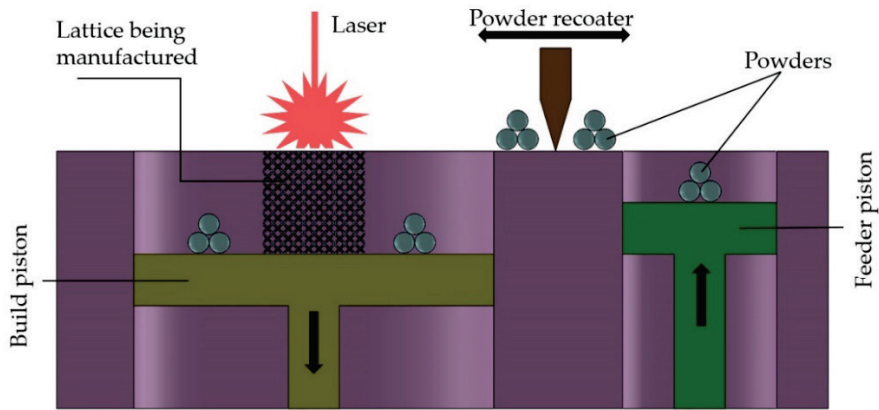


Figure 1.1 Schematic of a selective laser melting (SLM) device.

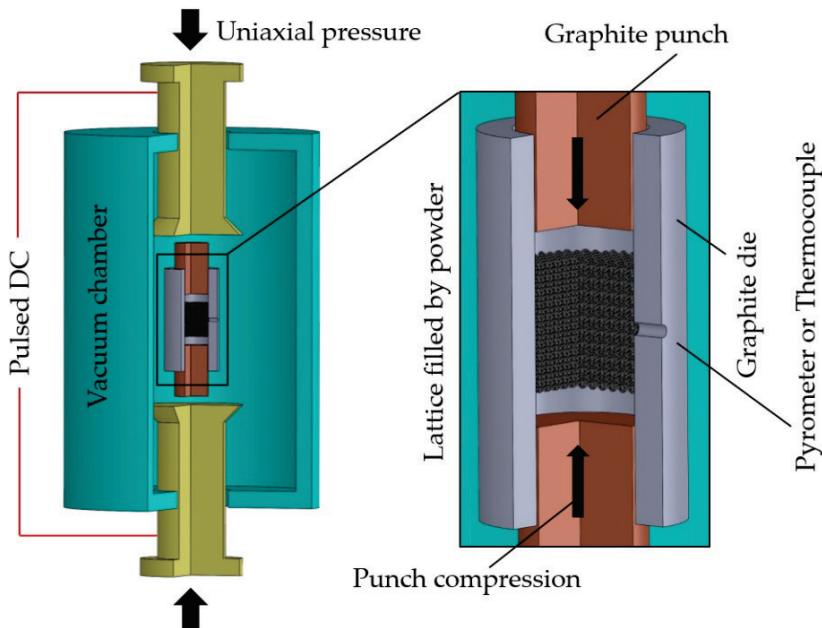


Figure 1.2 Schematic of a spark plasma sintering (SPS) device with graphite punches, mold and lattice/sample configuration.

1.3 Ti6Al4V and 316L metallic powders

Argon atomized titanium alloys have been extensively applied for aerospace structures, antibacterial surfaces, biomedical engineering, and orthopedic implants (i.e., femur bone as lattice, pelvic girdle as bulk, hip, vertebra and skull) because of excellent biocompatibility, flowability/sphericity, strength-to-weight ratio, wear and corrosion resistance in comparison with other metal alloys (Fig. 1.3) [25-29]. Ti6Al4V grade 5 containing 5.5-6.75 wt. % aluminum and 3.5-4.5 wt. % vanadium with density of 4.43 g/cm^3 ,

particle size $\leq 45 \mu\text{m}$ and melting point $\geq 1600 \text{ }^\circ\text{C}$ has excellent strength, stiffness, low density and high wear resistance [30, 31].

Apart from biomedical and chemical applications of stainless steel, it is counted as exceptional concerning its excellent powder fluidity in the SLM approach, corrosion resistance, and strength at high temperatures. Excellent mechanical properties and wear resistance of 316L and Ti6Al4V alloys motivated us to mix them and improve the mechanical characterization. The 316L powder (with density 7.95 g/cm^3) is an austenitic low-carbon stainless steel containing 16-18 wt. % chromium, 10-14 wt. % nickel and 2-3 wt. % molybdenum. 316L stainless steel can be applied for a wide range of applications, e.g., biotechnology, medical/surgical instruments, metallurgy, tribology, and tissue engineering [32-35]. The approval of 316L alloy was influenced either by the satisfactory or excellent mechanical properties or/and fair cost. It is usually recommended for a wide industrial application of parts and assemblies. The lower carbon content and non-magnetic effect of the material makes it suitable for corrosion and wear resistant applications [36, 37].

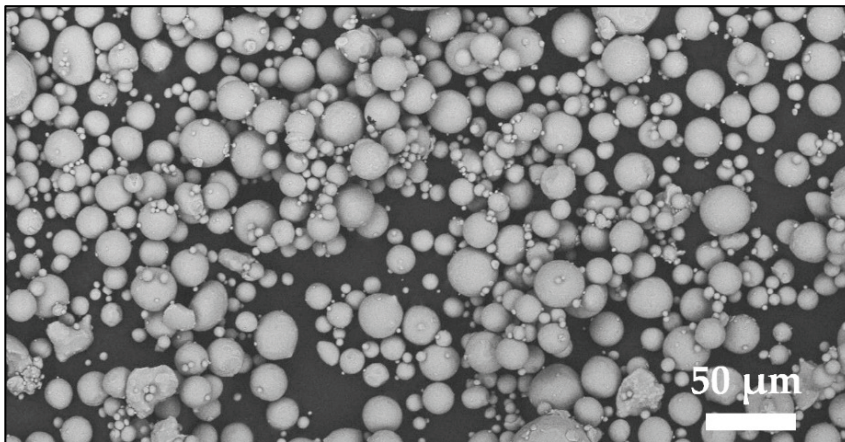


Figure 1.3 SEM micrograph of Ti6Al4V powders.

1.4 Diamond particles

Printing diamond particles is a big challenge and edge of AM craftsmanship that has up to now only reported as a patent from Lockheed-Martin company. However, printing pure diamond particles or mixed with metal powders depends on the ability of laser power and other 3D printer's parameters. One such route is via metal-coated polycrystalline diamond (PCD), which is also used in our research. The coating is usually based on cobalt, nickel, aluminum, and copper, or their alloys (Fig. 1.4). It is commonly used for its good thermal conductivity in electronic components and/or wear resistance in tunneling equipment. It was shown in recent literature/patents that optimized content of 316L, Ti6Al4V and diamond powders can be mixed or/and sintered as solid via different approaches. The final result has surveyed uniform distribution of diamond particles throughout the specimen and the role to improve the wear rates and improved crack resistance [38-42]. However, SLM-SPS combined method in the current thesis is a totally new idea to replace older methods.

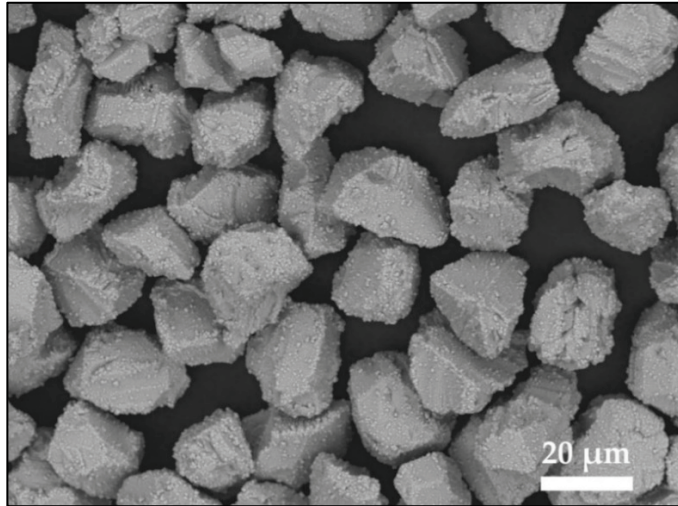


Figure 1.4 Diamond particles coated by 30% nickel.

1.5 Cellular lattice structures

Cellular metallic lattices/scaffolds are integrated structures with designed periodic voids and struts. The mechanical properties of lattices are a function of the volume fraction (VF, the weight/density ratio of the metallic lattice relative to the weight/density of the base material or occupied solid volume), the unit cell size and strut diameter [43]. Nowadays, focus is shifted towards three patterns repeating in perpendicular directions, known as triply periodic minimal surface (TPMS) that has complicated mathematic equations [44, 45]. TPMS structures are continuous surfaces and of relevance in natural science, which is interesting for mathematicians, architects and engineers. Cellular lattice and TPMS structures (including continuous surfaces and continuous rods/struts) have been applied in many engineering fields, such as in tissue engineering and structural engineering [46-48]; they have proved to process required strength and stiffness, optimal thermal and electrical conductivities, fluid permeability, and biocompatibility. Some of titanium alloy lightweight printed scaffolds are shown in Fig. 1.5.

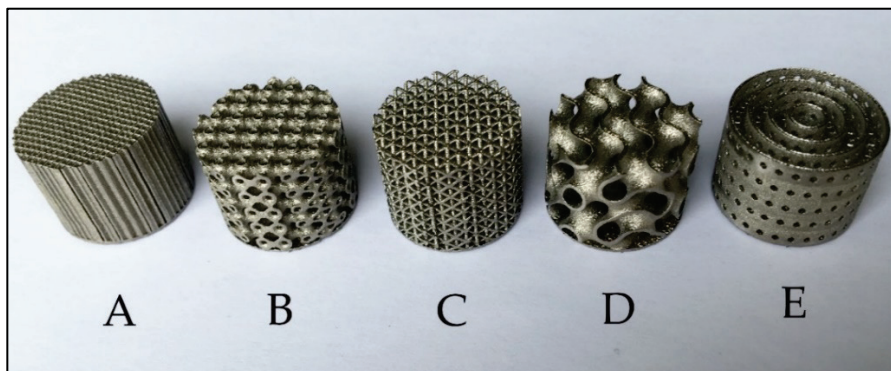


Figure 1.5 Type of manufactured TPMS structures using the SLM method: A) Rectangular, B) Primitive, C) Lattice, D) Gyroid, E) Honeycomb (dimension of samples is 20 mm in diameter and 15 mm in height; weight of samples is between 3.30-5.50 g).

1.6 Objectives of the study

The main aim of the present study is to introduce and develop the production of the metal-ceramic composite to have ductility of metal and hardness of ceramic with the help of SLM and SPS techniques. Objectives of this thesis are:

- To design and manufacture functionally gradient lattice structures, including metal, ceramic and mixed/embedded layers that enable higher weldability/ductility at the bottom layer (more metal) and higher hardness at the top (more ceramic) for tribological applications.
- To add the different percentage of diamond particles to metal alloys (10 wt.% and 5 wt.% PCD particles in the 316L or Ti6Al4V powders) for 3D printing for the first time to investigate brittleness of struts, to consolidate diamond particles in situ and to provide a potential possibility for filling by other hard materials in SPS.
- To improve the compression strength and damage tolerance of the titania-titanium composite (SLM manufactured Ti6Al4V lattice filled with TiO₂-Ag powders and consolidated by SPS) for antibacterial applications.
- To conduct the mechanical-biomedical characterization of different types of lightweight metallic structures (rectangular, primitive, lattice, gyroid and honeycomb) made by titanium-wollastonite for transporting oxygen and to convey the fluid, growth of cells, load-bearing, and bone replacements.

2 Materials, methods and lattice printing

Functionally graded lattices (FGL) manufactured by a SLM metal printer and filled with hard materials such as diamond particles, WC-Co, or cubic BN that are later sintered with the SPS are proposed as the approach to fabricate parts with improved abrasion-impact wear resistance. A schematic of such FGL structure with a fully-metal region at the bottom for better weldability/ductility, gradient interlayers (metal-ceramic or metal-metal composite for industrial applications) and wear resistance (high hardness and damage tolerance) at the top is illustrated in Fig. 2.1. These scaffolds/lattices can be consolidated via SPS with various types of hard materials [49], ceramics, metals or oxides for antibacterial [50], biocompatibility [51, 52], and tribological [53] applications.

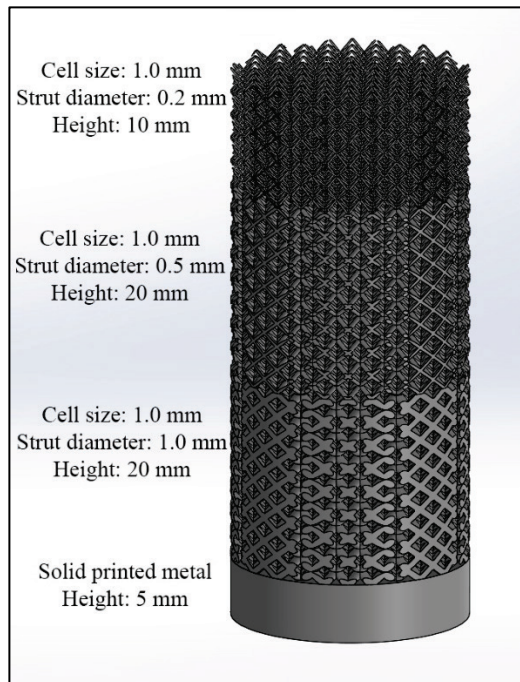


Figure 2.1 FGL structure with a dense metal region at the bottom for better weldability and ductility, interlayers gradient metallic and highly ceramic layer at the top. Sample with 20 mm diameter was designed for corresponding SPS mold [Publication 1].

2.1 Fabrication of gradient structure

The sketch of the FGL structure obtained by combined SLM-SPS routes is given in Fig. 2.2. From bottom to top, Ti6Al4V or 316L metallic lattice content/share decreases and diamond particles contents increase. The three most important parameters for the printing of metallic lattices by the SLM method are as follows: laser current (LC=3000 mA, corresponding to 72 W power), exposure time (ET=600 μ s), and point distance (PD=1 μ m, only solid parts, not used for lattice structures) [54]. In addition, we use the platform made from the same material as metallic lattice to be printed. The thickness of every layer was 25-50 μ m and the supports were used to connect the printed part to the platform (depends on the machine and desired part densification).

Argon or nitrogen was applied as a protective gas during a process inside the printing chamber [55].

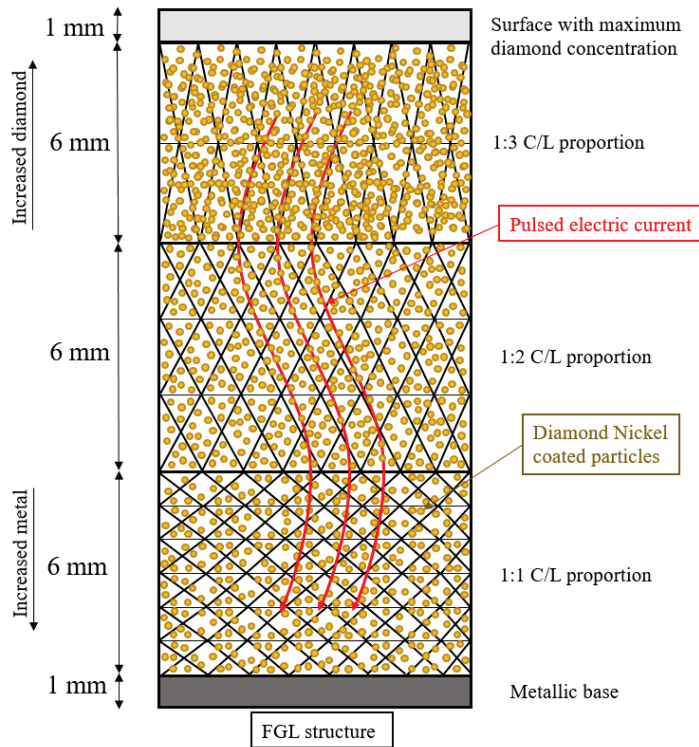


Figure 2.2 Schematic of material with FGL structure (during preparation before sintering) [Publication 5].

Three fabricated FGLs made from Ti6Al4V by the SLM technique are shown in Fig. 2.3. The size and the diameter of the SPS mold used can be varied depending on the application (tribological, mining, tunneling, etc. [56, 57]). The structure of the specimens is denser (higher volume fraction) at the bottom and decreases gradually towards the top, with 42 %, 30 %, and 16 % volume fraction of metal sequentially. The outer dimensions of the specimens are $\varnothing 20 \times 18$ mm, $\varnothing 30 \times 24$ mm, and $\varnothing 50 \times 30$ mm. However, the quality of manufactured lattice depends on the machine design and is influenced by the properties of the powders. The best route to find out the optimized printing parameters (LC, ET, and PD) is to investigate the powder micrographs and characterizations from supplier companies [58-63].

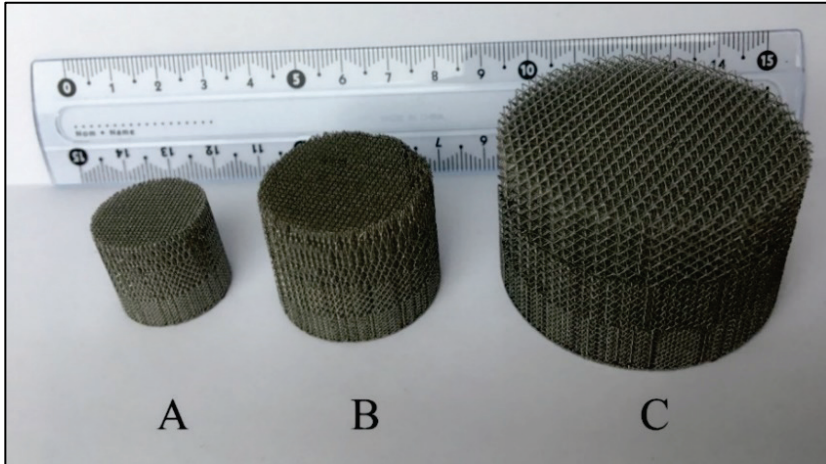


Figure 2.3 Demonstration of the possibility of fabrication of Ti6Al4V lattices of required size functionally graded from bottom to top in three metal volume fraction stages (42, 30, and 16 %). The diameters and heights of samples are: A) $\text{\O}20 \times 18$ mm, B) $\text{\O}30 \times 24$ mm, C) $\text{\O}50 \times 30$ mm [Publication 1].

2.2 Diamond-metal composite printing

It is also possible to manufacture composite materials including diamond particles during the SLM. 3D printed struts with a mixture of sintered Ti6Al4V and diamond particles with 5 wt. % and 10 wt. % of diamond are shown in Fig. 2.4. In the case of 10 wt. % diamond particles mixture, the stickiness/adhesion of the struts is relatively weak (due to weaker bonding between diamond and metals; the diamond particles are not melting during the printing procedure), which leads to a more brittle scaffold structure. The problem can be solved relatively by decreasing the fraction of the diamond particles in the cross-section of the strut (thicker metallic lattice rods). Ti6Al4V lattice structure in desired unit cells with 10 % diamond particles was printed on 70 mm diameter and 40 mm height Realizer SLM50 platform, including two failed jobs (Fig. 2.5). As shown in Fig. 2.5, the lattices are brittle with an increase in the diamond content, and printed samples can collapse during the manufacturing process [56, 57].

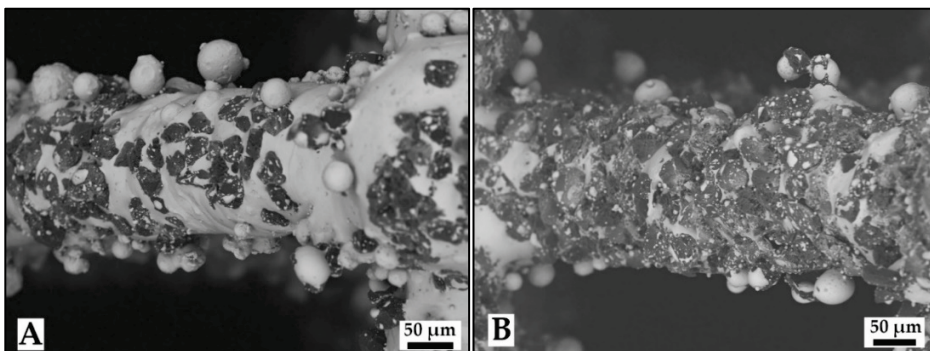


Figure 2.4 3D printed Ti6Al4V lattice with A) 5 % and B) 10 % diamond particles of volume content. The unit cell size is 1 mm and the strut diameter 0.2 mm in both cases [Publication 1].

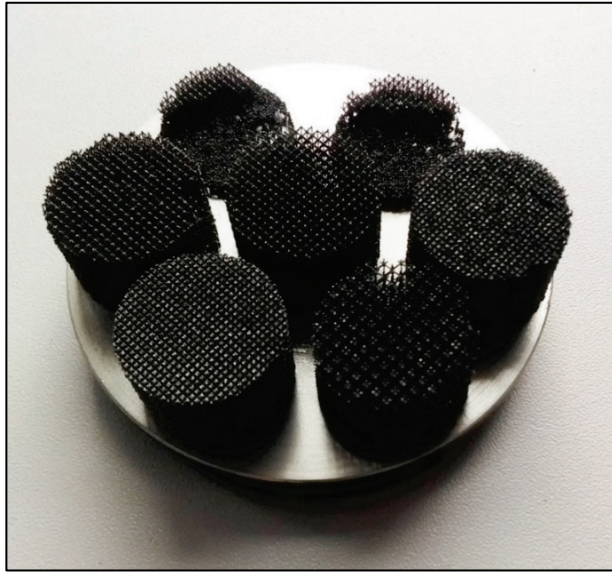


Figure 2.5 Ti6Al4V lattice structure in different unit cells with 10 % diamond of the volume content on the 70 mm diameter SLM50 platform.

2.3 Post-processing procedures

Nitriding, carburizing, PVD coating of lattice blasting by alumina nanopowders, polishing, and SPSing along with hard materials are known as post-processing of metallic lattices after the SLM route. The alumina nanoparticle blasting/cleaning can treat the 3D printed Ti6Al4V struts. The results of the process are shown in Figs. 2.6 and 2.7 for different strut diameters. Nano-particle post-blasting has a crucial role to avoid single inclusions weakly stuck to the main structure surfaces/struts that are especially important for biomedical applications with precisely defined void/strut dimensions because separation of uncontrollable metallic powders is not desirable in vivo. The effect of pore region and strut geometry [64] is becoming more important when a gradient bio-structure is applied with different pores sizes [65] and treatment/modification of surface is definitely needed [66].

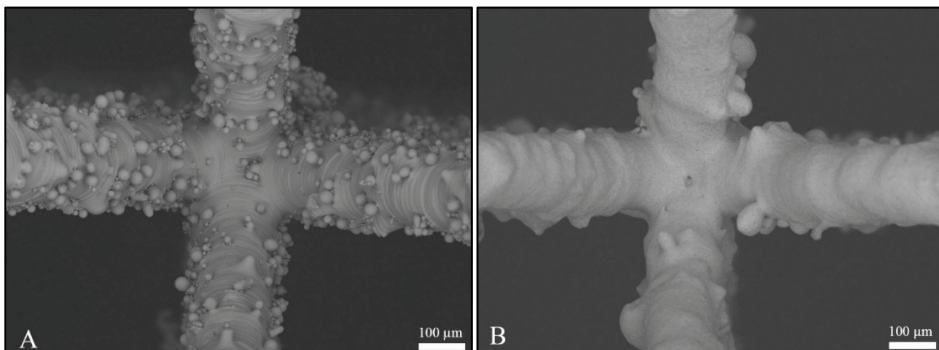


Figure 2.6 Ti6Al4V lattice structures with 1.5 mm cell size and 0.2 mm strut diameter A) after printing and B) after blasting with alumina nanoparticle [Publication 1].

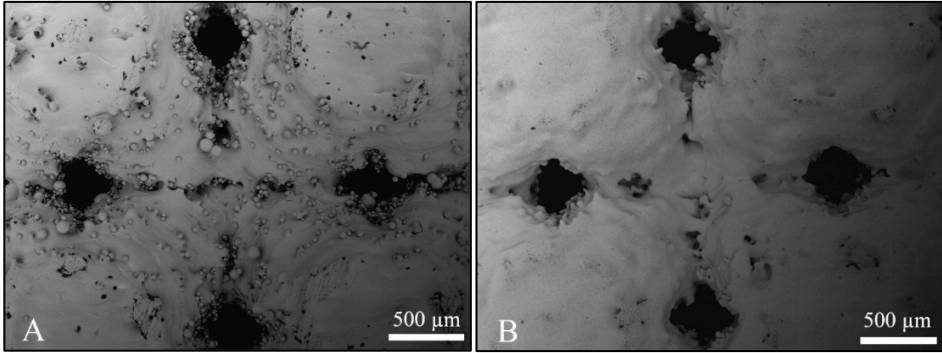


Figure 2.7 Ti6Al4V lattice structures with 2.0 mm cell size and 1 mm strut diameter A) after printing and B) after alumina nanoparticle blasting [Publication 1].

In this study, the design, simulation, and the test of TBM parts including cutterhead, drag bits, inserts, and buttons are considered against impact-abrasion [67-69]. The TBM's insert made by conventional powder metallurgy methods (first pressing and then sintering) and 3D printed structure prepared for filling/consolidating by HIP or SPS are presented in Fig. 2.8. Nitriding of titanium alloy lattice (to obtain TiN) as reinforcement can provide improvement in the wear and corrosion resistance of materials is still going on. Nitriding idea is applied to create hard face, instead of using diamond. The Ti6Al4V lattice (argon-atomized powders that are sintered in the SLM50 chamber under vacuum pressure of argon) was heated in vacuum nitriding furnace (VNF) under constant nitrogen gas, flowing with a 10 °C/min heating rate and 90 min holding time at the nitriding temperature mentioned below. Digital photos of nitriding Ti6Al4V lattice structures with 2 mm cell size, 2 μm strut diameter, and different nitriding temperatures (750 °C, 900 °C, 1050 °C) are shown in Fig. 2.9.

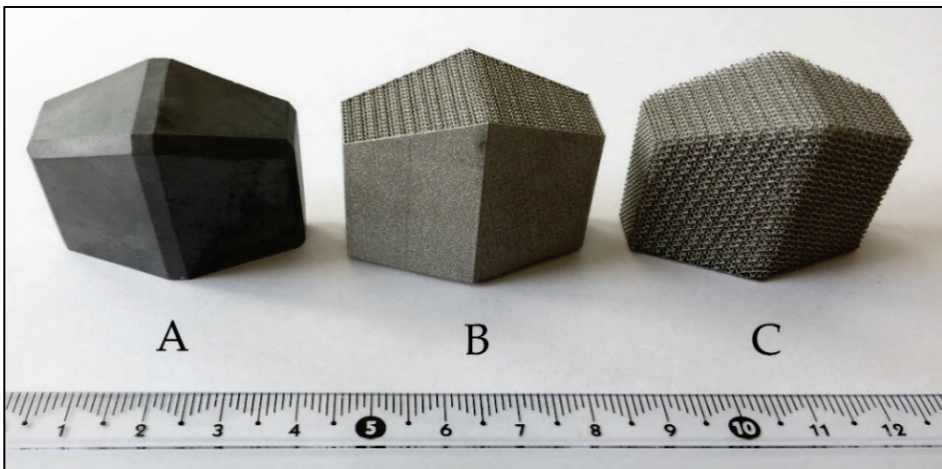


Figure 2.8 Tunnel boring machine insert produced by the conventional powder metallurgy method (A), 3D printed structure for HIP (B), 3D printed structure ready for filling and following consolidation by SPS (C) (length, width and height of sample is 36×16×30 mm) [Publication 4].

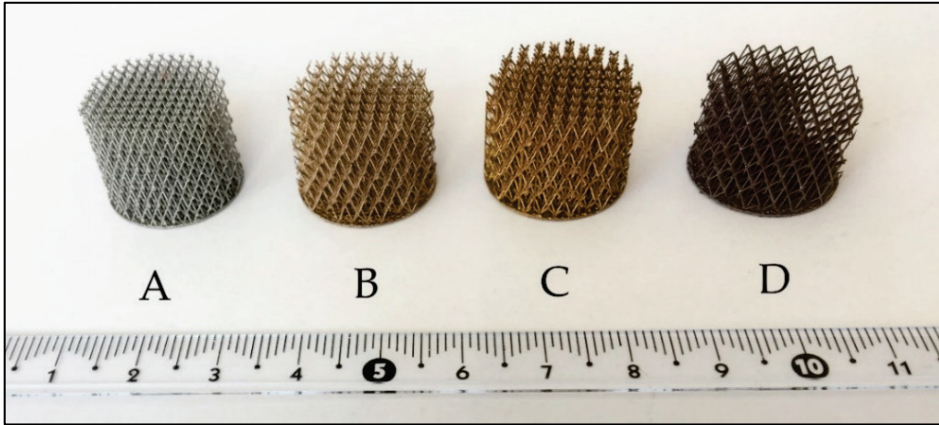


Figure 2.9 Manufactured untreated Ti6Al4V lattice (A), heated and nitrided Ti6Al4V lattices at 750 °C (B), 900 °C (C) and 1050 °C (D). Metal volume fraction and unit cell size are 6 % and 2 mm, respectively (diameter of lattice structures is 20 mm and height is 15 mm) [Publication 4].

2.4 Unit cell design

Metallic lattices can be produced uniformly or gradually by metal or ceramics for impact absorption or armor piercing (AP) applications. A metal-ceramic functionally gradient structure is proposed to gain high metal content at the bottom (best ductility), composed of metal-ceramic (Al_2O_3 sintered inside printed Ti6Al4V lattice) interlayers, and pure ceramic at the top (highest hardness). In addition, the mixed Ti-Al composite (titanium has higher density and strength than aluminum) can be developed based on weight and application. This fact can be controlled by cell sizes and strut diameters. Selected design of unit cell type/architecture of lattice regarding the application is shown in Figs. 2.10 and 2.11 as SolidWorks/CAD designed and 3D printed. For impact absorption cases, body-centered or face-centered cubic (BCC or FCC) structure can be investigated [70-72].

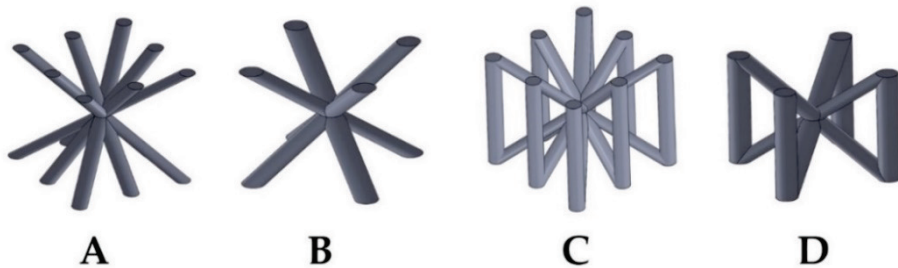


Figure 2.10 SolidWorks design of unit cells to absorption of impact energy (for example trap the ballistic bullet) and resistance against buckling/compression [Publication 6].

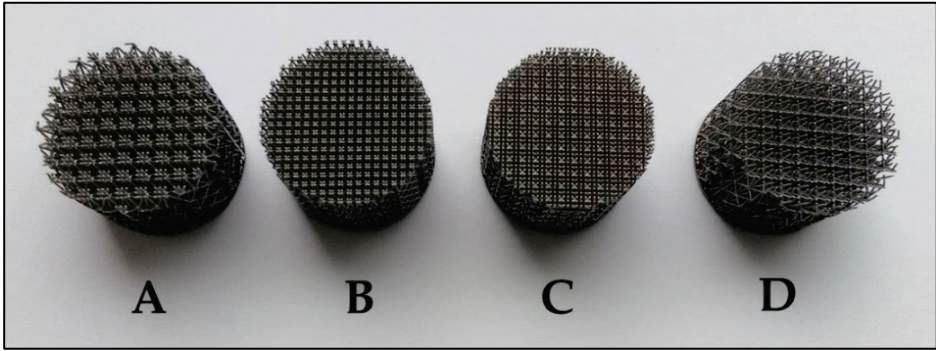


Figure 2.11 Manufactured scaffolds from different cellular lattice cells to absorb the impact energy (see Fig 2.10 for the unit cell structure). Different unit cells lead to different volume fraction and proportion of lattice structure in sintered/filled solid sample (diameter of lattice structures is 20 mm and height is 15 mm) [Publication 6].

3 Modelling and simulation study

In this study, in the case of prototype lattice structures or composite solid samples, SolidWorks, Ansys and COMSOL software were applied to assess the behavior of materials under impact, compression and abrasive loadings [50-57, 73, 74].

3.1 Design of gradient structure

A SLM50 Realizer device with a laser power of 75 W was applied for the fabrication of Ti6Al4V alloy (Gd5 powders with size $\leq 45 \mu\text{m}$ and density 4.43 g/cm^3 supplied by TLS Technik GmbH) in configuration of functionally graded lattice (FGL) structures, namely, uniform lattice, FGL in the longitudinal direction (bottom to top) and circumferential directions (inner to outer) with 1, 1.5, and 2 mm cell sizes (Fig. 3.1). Finer mesh lattice (such as bottom layer in Longitudinal FGL or inner layer in Circumferential FGL) has higher resistance and lower shrinkage when subjected to compression during the SPS process. The sintered samples are manufactured by SPS after filling by pure Aluminum (or Al alloys like 7075 or AlSi10Mg) and fixing inside a graphite mold (Fig. 3.2) for different protective applications, e.g., against ballistic impact [75], multi-layered metallic plates against projectile [76], perforation comparison of Al-alloy with Fe-alloy [77], and Ti6Al4V/ceramic/ AlSi10Mg armor piercing [78].

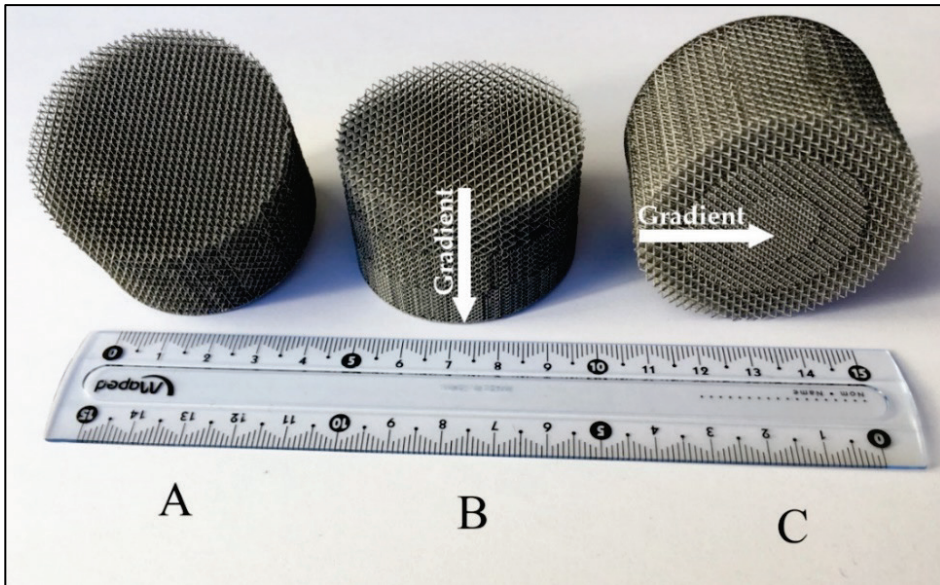


Figure 3.1 Ti6Al4V lattices: A) Uniform with 1.5 mm cell size, B) Longitudinal gradient, C) Circumferential gradient (gradient structures have 1 mm and 45 %, 1.5 mm and 30 %, and 2 mm and 15 % cell sizes and volume fraction (VF), respectively. All lattices have 50 mm diameter and 30 mm height). Final weights of Ti6Al4V lattices are A) 20 g, B) 30 g, C) 25 g. Arrows show increased VF directions in metallic lattices.

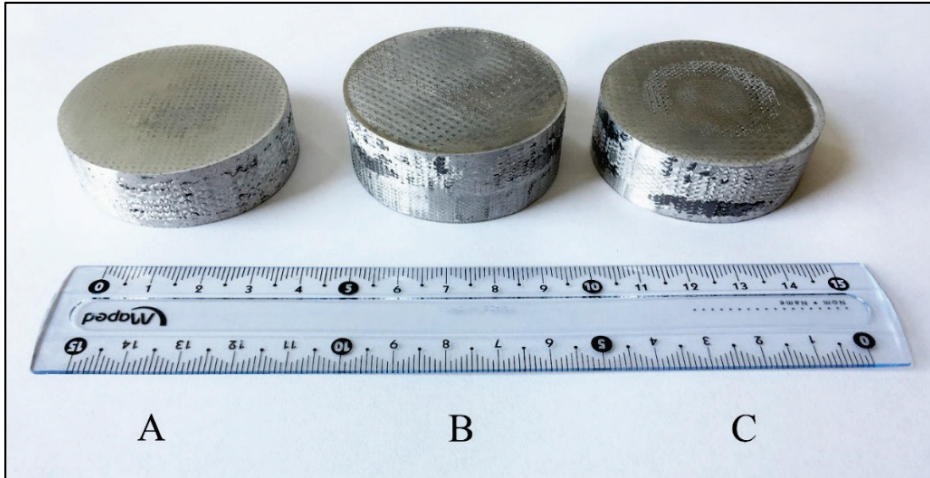


Figure 3.2 Ti6Al4V-Aluminum samples after SPSing (see Fig 3.1 for lattice structures): A) Uniform, B) Longitudinal gradient, C) Circumferential gradient (final heights of samples are 14, 18 and 16 mm, respectively). Final weight of samples is around 80 g after polishing, namely A) 20 g + 60 g, B) 30 g + 50 g, C) 25 g + 55 g of Ti6Al4V lattice and Al filled powder.

3.2 CAD modelling of gradient structure

Four lattice-included cylindrical samples ($\varnothing 12 \times 15$ mm) modelled in identical conditions (fixed in the end and free deformation in axial direction) via SolidWorks CAD software are shown in Fig. 3.3. The first and second samples were modeled by a uniform embedded/distributed lattice structure throughout the sample in 3 mm (coarse mesh, Fig. 3.3A) and 1 mm (fine mesh, Fig. 3.3B) unit cell size. For all samples, lattice structures were made by Ti6Al4V titanium alloy filled inside plain Al, to have strength, impact absorption ability, lightweight and ductile structure. Two last samples were reinforced with longitudinal/axial (Fig. 3.3C) and circumferential/radial (Fig. 3.3D) FGL structure gradually designed by 1 mm, 2 mm and 3 mm unit cell sizes and lattice-free volume at the top or around of the sample.

Instead of metal-metal hybrid samples it is possible to apply a metal-ceramic composite in the uniform or axial/radial gradient configuration [79-82]. Then, Ansys Workbench analyzer and AUTODYN solver can display deformation and Von Mises stress for samples subjected to compression, impact and abrasion. This method demonstrates the difference between the plain samples, uniform lattice (in course and fine mesh) and FGL structures (in vertical and horizontal directions). The aim is to develop a method to predict the mechanical characterization of new metallic structures or plain ceramics.

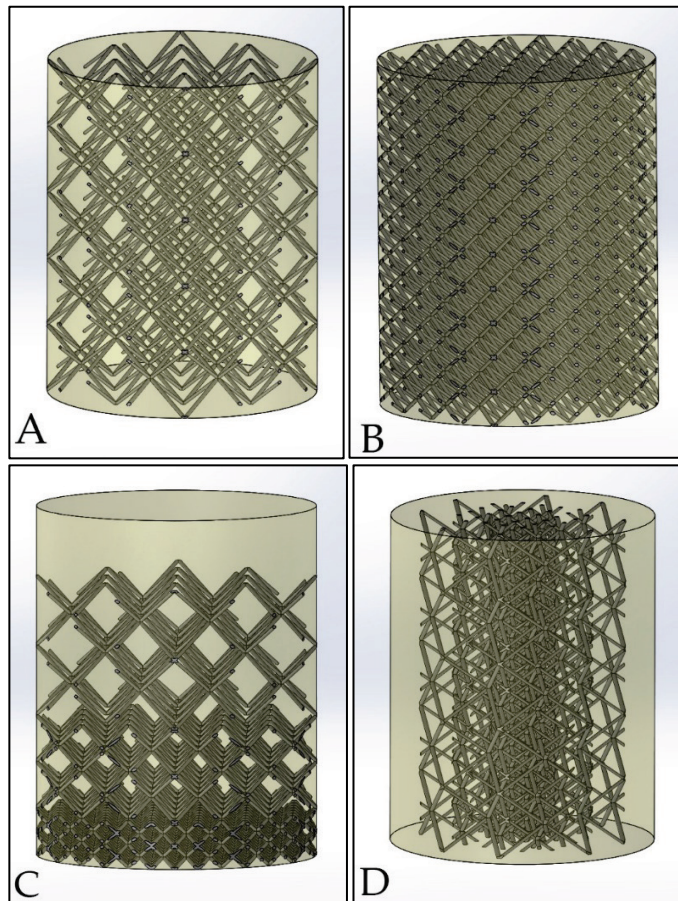


Figure 3.3 Samples designed by SolidWorks as lattice-included composites: A) Uniform 3 mm cell size, B) Uniform 1.5 mm cell size, C) Longitudinal gradient, D) Circumferential gradient.

3.3 Simulation of compression test

The composite structure where TiO_2 -Ag-doped was embedded inside titanium lattice modelling showed not only increased damage tolerance but also increased ultimate compressive strength as compared to unreinforced and plain ceramics. The compression test results showed large lost pieces in the case of ceramics, whereas ceramics in the metal-ceramic sample was fractured into sub-micrometric particles (Fig. 3.4). Numerical simulation prepares an estimation of cermet composites strength produced by combining SLM and SPS techniques subjected to impact, abrasion and compression loading. The finite element can decrease the cost of mechanical characterization for focusing only on antibacterial analyses. The results illustrate a fracture for pure ceramic at 500 MPa while buckling for metallic lattice-included starts from 1200 MPa (Fig. 3.5). Damage tolerance of Ti6Al4V- TiO_2 composite was influenced significantly by the density of ceramic (layer thickness definition in SLM device) and strength of metal-ceramic bonding (pressure and temperature adjustments in the SPS device) [83-85].

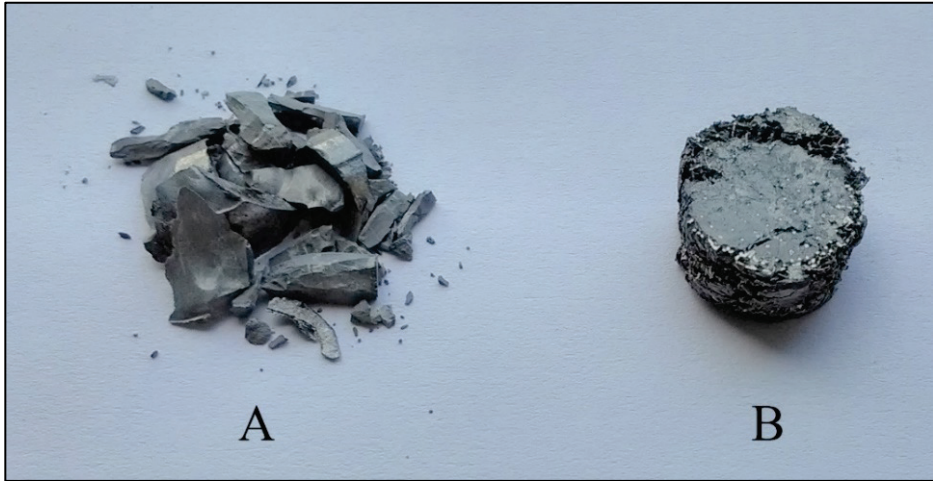


Figure 3.4 Appearance of (a) TiO_2 , (b) composite structure with TiO_2 - Ti6Al4V hybrid after compressive testing (sample diameter is 10 mm) [Publication 2].

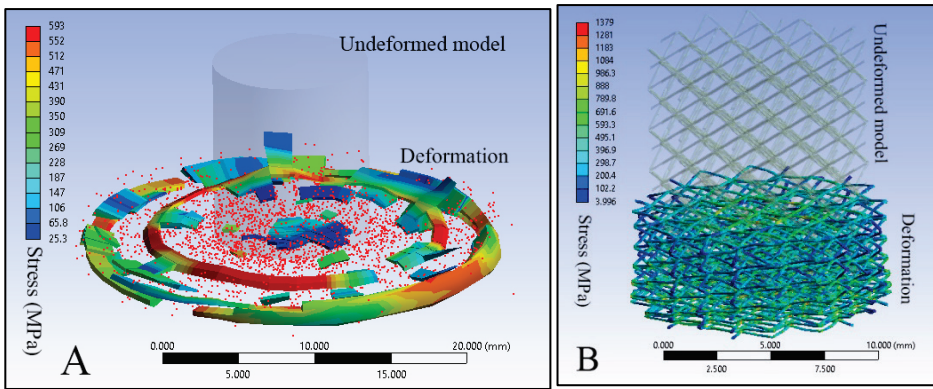


Figure 3.5 Compressive strength modelling of A) Plain TiO_2 ceramic; B) Ti6Al4V lattice structure performance including TiO_2 ceramic. Simulation condition and dimension are identical for the ceramic and the lattice structure [Publication 2].

3.4 Simulation of impact test

Pure TiO_2 and TiO_2 embedded into Ti6Al4V lattice structure were compared under high-speed impeller to investigate the shock absorption. The experiment was designed in SolidWorks software (20 mm diameter and 4 mm thickness for sample and $2 \times 2 \times 2$ mm cell size for lattice structure) and it was analyzed by Ansys software (explicit dynamic nonlinear simulation of 1 s impacting process, 100 m/s impeller velocity). As can be seen in Fig. 3.6, the sample with TiO_2 embedded into the Ti6Al4V lattice structure is fixed and the impeller blade will be crashed to the middle of the sample. Comparison between Figs. 3.7A and 3.7B illustrates the resistance of the lattice structure against the impact. At the same impact time, boundary condition and speed, titania (ceramic) is split into two parts but titania-titanium (cermet) absorbed the stroke of the impeller without disjunction of ceramic. Von Mises stress is decreased in the contact region of the lattice-included sample and the stress concentration is located in the lattice structure, not in the ceramic.

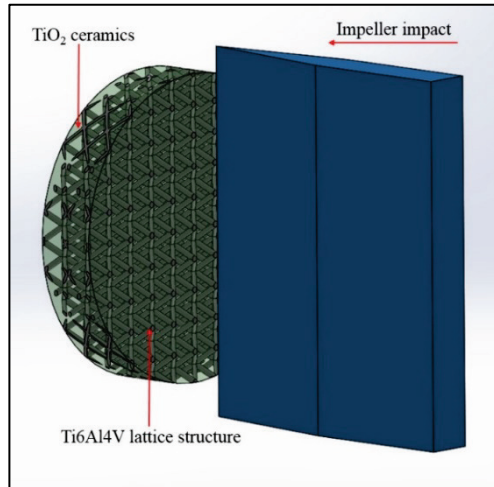


Figure 3.6 SolidWorks design of the sample and the impeller.

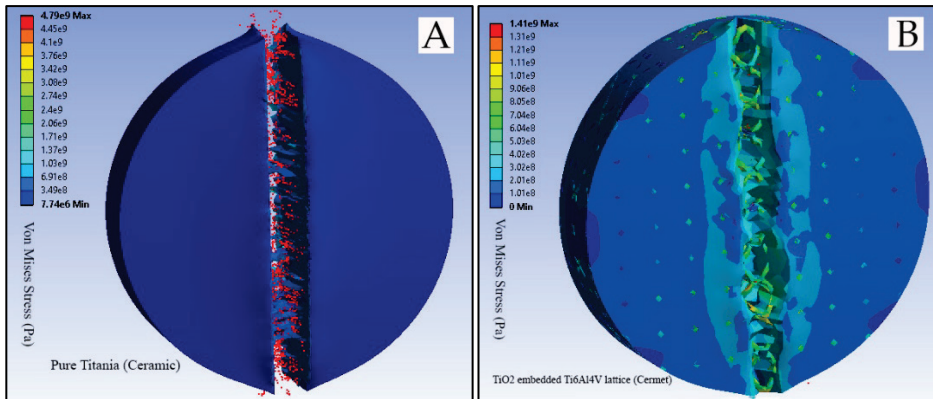


Figure 3.7 Ansys analysis of A) Pure TiO_2 without lattice; B) TiO_2 embedded Ti6Al4V lattice structure samples subjected to impact.

3.5 Simulation of abrasion test

A finite element model to show the benefits of the lattice-included structure of TBM drag bit inserts against abrasion (scratching or sliding) (Fig. 3.8) was designed/simulated by SolidWorks/Ansys software. The results show the ability of the lattice structure to absorb energy and decrease the rising of local stresses. Plain diamond sample (without lattice) and diamond with Ti6Al4V lattice were compared in the case of Von Mises stress distribution.

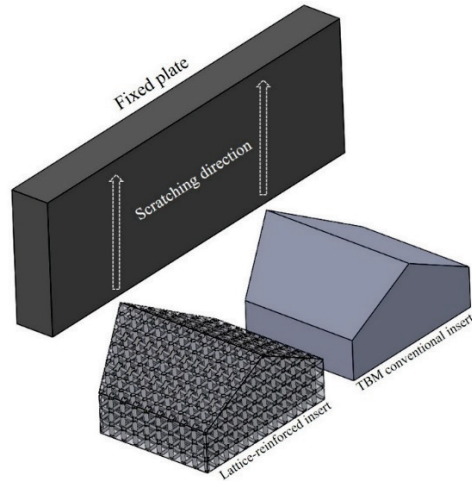


Figure 3.8 SolidWorks design of consolidated diamond particles with and without lattice structures.

The steel (as wall) was chosen to illustrate the behavior in the critical conditions. The components were meshed and the boundary conditions were defined with the help of Ansys workbench analyzer and AUTODYN solver, as can be seen in Fig. 3.8. The strut diameter of the modelled lattice structure was $200\ \mu\text{m}$ and the unit cell size was $1\times 1\times 1\ \text{mm}^3$. Sliding speed was set at $1\ \text{m/s}$ and distance was $1\ \text{m}$. Stress distribution of diamond particles at the end of abrasion is demonstrated in Fig. 3.9. It is shown that the lattice-free sample is broken in tip during the sliding while the diamond with lattice experienced mainly minor deformation with some loss of extruded metal lattice (diamond particles are not lost, Fig. 3.9). Fig. 3.10 shows that separated particles are Ti6Al4V parts, not diamond particles.

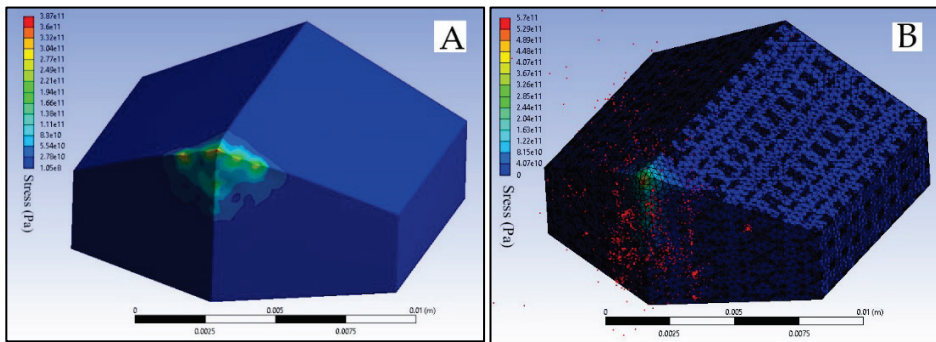


Figure 3.9 Ansys analysis of Von Mises stress distribution of TBM inserts: A) Conventional plain, B) SLM lattice consolidated by SPS.

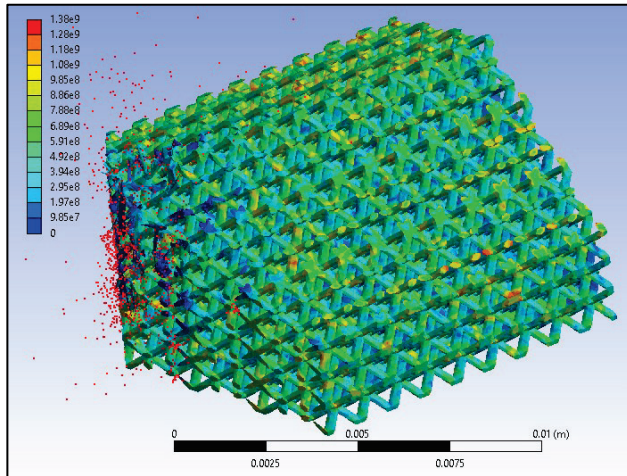


Figure 3.10 Ansys analysis of stress distribution on the lattice embedded into diamond plain (red dots are separated particles during the sliding).

4 Results and discussion

Interdisciplinary application is supposed to be obtained from the combination of SLM-SPS routes. However, preliminary outlook has been depicted for the future perspective of AM, as well as the study of antibacterial, biomedical, mining/tunneling, and tribological applications.

4.1 Antibacterial application

4.1.1 Structural study

The appearance of ZrO_2 , TiO_2 Anatase, 50% ZrO_2 and 50% TiO_2 , TiO_2 and 2.5% Ag, TiO_2 Rutile, and TiO_2 embedded in Ti6Al4V lattice composite materials is shown in Fig. 4.1. The color of pure anatase TiO_2 ceramic changes from greyish to whitish with darker spots for TiO_2 -2.5% Ag ceramic. The TiO_2 -Ti6Al4V composite structure has good interphase cohesion and uniformity between ceramic bonds and metallic cellular struts. Some porosity is seen at the interphase, at the areas of the higher surface roughness of the printed metal lattices. It is preferable to face the surface with pure ceramic for an antibacterial application. Based on this logic, the best condition for an antibacterial application would be a lattice that includes ceramic for lower layers and pure ceramic without lattice for outer surface.



Figure 4.1 A) ZrO_2 , B) TiO_2 Anatase, C) 50% ZrO_2 and 50% TiO_2 , D) TiO_2 and 2.5% Ag, E) TiO_2 Rutile, F) TiO_2 embedded in Ti6Al4V lattice (diameter of samples is 20 mm and final heights are 3-6 mm after SPSing).

4.1.2 Antibacterial assay

Antibacterial activity of lattice-included composites before and after SPSing and the cermet composites and ceramic materials towards *Escherichia coli* K12 MG1655 was evaluated after 30 min and 4 h exposure (Fig. 4.2) while using ZrO_2 surface as negative control. Among the tested materials in dark conditions, the highest antibacterial effect corresponding to reduction in *Escherichia coli* viability was observed for TiO_2 -2.5% Ag ceramics already within 30 min compared to negative control and no viable bacteria were detected at the detection limit of about 450 CFU per surface. Silver-doped titania for increasing photocatalytic activity has been studied in [86-88] and can be applied for water pollutants with the help of 3D printing [89]. Adding metallic lattice to ceramic silver-doped titania material decreased the antibacterial effect compared with plain ceramics and increased the damage tolerance. The solution is to cover the TiO_2 -Ag-Ti6Al4V surface with a thin layer of pure ceramic material to hide/cover the lattices from surface.

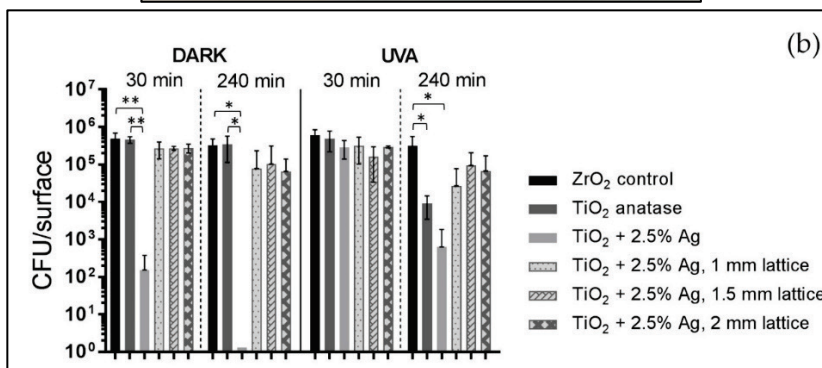
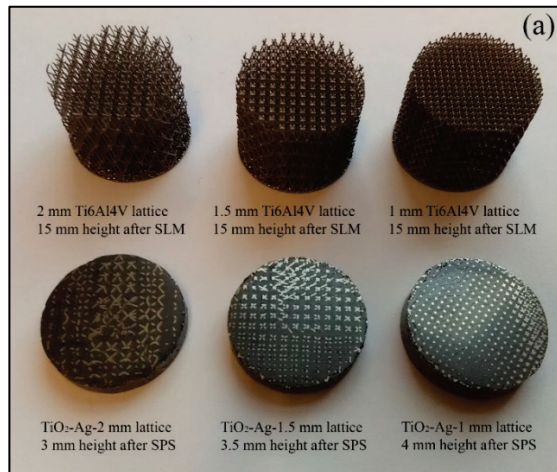


Figure 4.2 a) Lattice-included composites before and after SPSing, b) Viability of *E. coli* MG1655 on ceramic and composite hybrid surfaces after 30 min and 4 h exposure in the dark and UVA-illuminated. Columns represent recovered viable bacteria as colony forming units (CFU). Mean and standard deviation of at least 3 independent values is shown on logarithmic scale and only statistically significant differences ($p < 0.05$) are marked on the graph (* < 0.05 and ** < 0.01) [Publication 2].

4.1.3 Prospective applications

3D metal printing is a promising approach to combine powder metallurgy for biomedical applications (lattice structure with bone shapes filled by biomaterials or Bioceramic scaffolds for controlled delivery of the antibiotic). The SLM method has the ideal capability to manufacture patient-specific artificial implants due to complicated body anatomy. Combining SLM with ceramic consolidation methods as SPS or HIP enables one to apply cermet and functionally graded material (FGM) productions in hip joint, rib cage, bone truss, tooth implant, etc. Furthermore, metal to ceramic gradient can be produced in either longitudinal (Fig. 4.3A) or circumferential directions (Fig. 4.3B) [91, 92] according to skeleton configuration.

Photosynthesis of water into constituent parts, H₂ and O₂, is achieved using solar or UV light for producing hydrogen fuel cells [92]. Water splitting is needed for titania semiconductor photoelectrode combined counter metal electrode such as platinum to increase H₂ generation [93]. Possible design of mechanism is shown in Fig. 4.3C, which can be produced by using the SLM-SPS method for solar powered vehicles. Regardless of

antibacterial and industrial fields, glasses frame, watch screen and car dashboard are considered as some luxury applications for metal-TiO₂ composite [94, 95]. Luxurious overview of 3D printing is illustrated in Fig. 4.3D with emphasis on watches with antibacterial effect on the top and/or bottom surface.

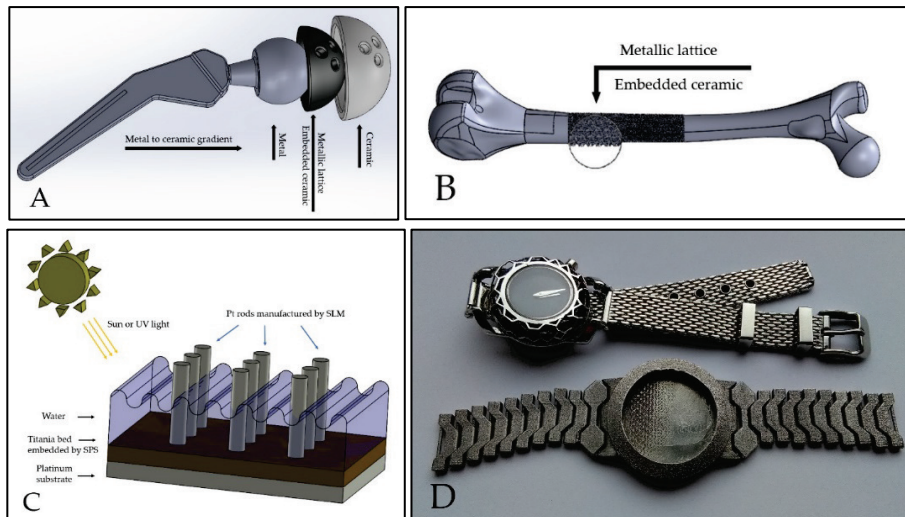


Figure 4.3 A) Sketch of hip joint and gradient longitudinal FGL connection to pelvis; B) Sketch of lightweight refractory femur bone structure; C) Photosynthesis of H₂O by combined TiO₂ and Pt photocatalyst using the SLM-SPS method; D) luxurious application to produce watches with antibacterial effect in surface or bottom.

4.2 Biomedical application

Combination of the SLM-SPS approach is introduced for producing metal-ceramic hybrid composites for chronic osteomyelitis, Vancomycin local delivery, and infected bones replacement in tissue engineering. The pure wollastonite (CaSiO₃) with a particle size of 1-5 μm (NYAD supplier, grade 1250) is filled and consolidated into spaces of atomized argon Ti6Al4V cellular lattice structure via SPS (Fig. 4.4). The process was performed with the pressure of 30 MPa at a holding temperature of 1100 °C with a heating rate of 100 °C/min and a holding time of 5 min [96-98]. Wollastonite composition includes 48.28 % CaO and 51.72 % SiO₂, while natural mineral may contain a small amount of iron, aluminum, magnesium, potassium, and sodium. SLM manufactured Ti6Al4V lattice with 1 mm unit cell filled by CaSiO₃ powder, sintered in SPS, polished by sandpaper, and good boundary between ceramic and lattice resulted after SPS, as shown in Fig. 4.5.

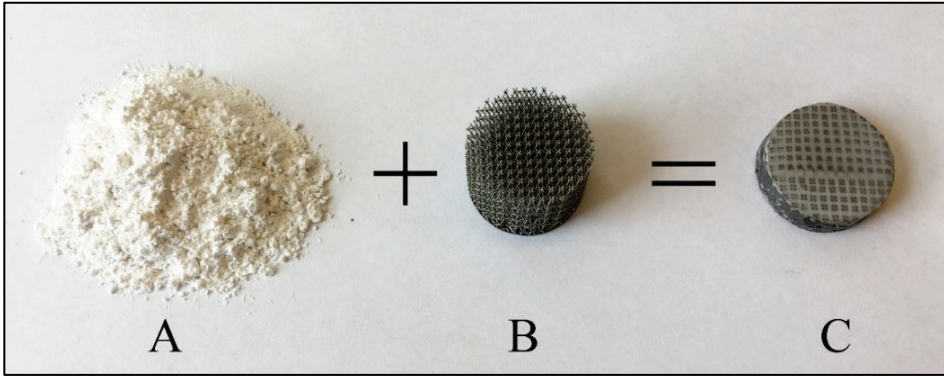


Figure 4.4 A) Wollastonite (CaSiO_3) powder; B) SLM produced Ti6Al4V lattice structure with 1 mm cell size; C) Sintered sample (dimensions of lattice structure: 20 mm diameter and 15 mm height before SPS and 6 mm height after SPS and polishing) [Publication 3].

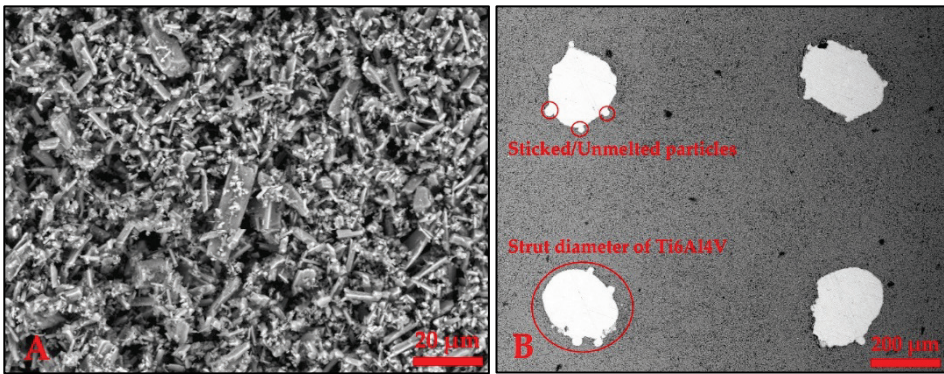


Figure 4.5 A) CaSiO_3 powder, B) A unit cell of Ti6Al4V with four cross sectional lattice rods/struts and a size of 1 mm (black dots are graphite sheet pieces after SPSing).

4.3 Tunneling study

4.3.1 Overview of TBM components manufactured by 3D printing

Hard materials with high wear resistance are most wanted in mining, metal machining, cutting, drilling, and tunnel boring machine (TBM) applications to increase productivity and to reduce the risk/time/price required for exchange operations. To assess the impact-abrasion performance, the configuration of the cutterhead, drag bits, inserts and buttons of TBM is schematically shown (CAD design) in Fig. 4.6. Up to now, the inserts were prepared by traditional powder metallurgy methods and nowadays, 3D printing technology is available to prepare samples for HIP or SPS post-processing procedures.

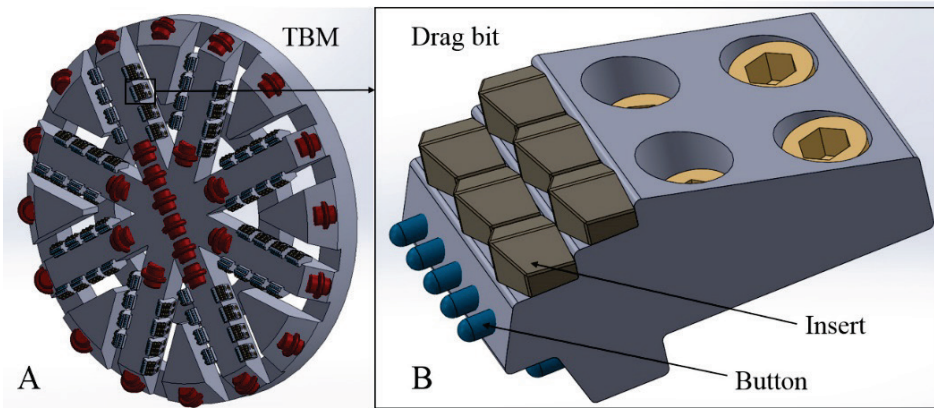


Figure 4.6 A) Schematic of tunnel boring machine cutterhead; B) Position of buttons and inserts in the drag bit (TBM diameter is 3000 mm, drag bit dimension is 195×115×90 mm) [Publication 4].

4.3.2 Mapping of impact-abrasive wear performance

It was confirmed by laboratory testing that the reinforcement by diamond particles added to metal alloy powders provides the best improvement when compared to a plain sample (Fig. 4.7A) and sintered inside metallic lattice (Fig. 4.7B). Both samples showed up to 2-6 times improvement in impact-abrasive wear conditions. Table. 4.1 gives the list of equipment required to fabricate the samples. To test the proposed fabrication technology, six materials were manufactured.

The mingled impact-abrasive tribo-device (IATD, Fig. 4.7C) was applied to test the samples. Sequential impact energy of 5.6 J and frequency of 27.5 Hz were provided by an impact generator (industrial hammer drill from Makita). The samples were experiencing reciprocate drill impact movement along with the rotating wheel to supply abrasive (made from WC-Co) with a force of 49 N and velocity of 1 m/s. Ottawa sand (used in ASTM G65 standard, particle size 0.2-0.3 mm) served as abrasive that was feuded through the nozzle into the contact region between the wheel and the sample [69, 99]. The test duration was 5 minutes, simulating 300 m of sliding distance.

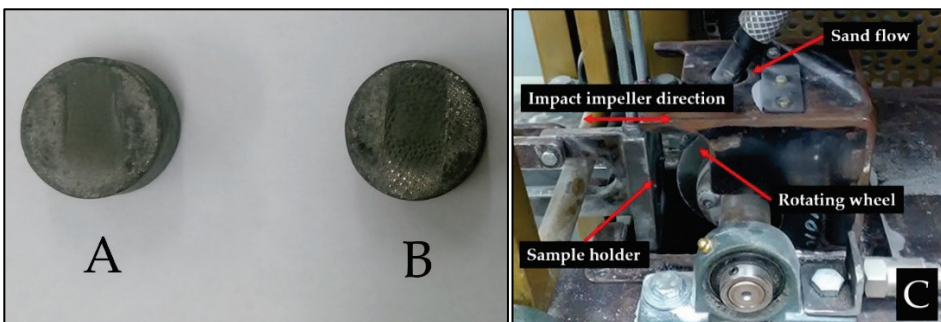


Figure 4.7 Digital photograph of samples: A) Without lattice; B) With Ti6Al4V lattice; C) Positioning the sample, impact drill and abrasive wheel in laboratory.

Table 4.1 List of machines used.

Process	Machine, Specification
Selective Laser Melting (SLM)	Realizer SLM50, construction volume $\varnothing 70 \times 40$ mm, layer thickness 20-50 μm
Spark Plasma Sintering (SPS)	FCT System, up to 2200 °C and 100 MPa, 1000 °C/min heating rate
Impact-abrasive tribo-device (IATD)	Tribosystem, up to 19 J impact energy and up to 55 Hz impact frequency
Vacuum Nitriding Furnace (VNF)	R. D. WEBB, up to 1700 °C, nitrogen flow and 10 °C/min heating rate
Scanning Electron Microscopy (SEM)	Hitachi TM-1000, magnification 20-10,000 X
3D Optical Surface Profiler (OSP)	Bruker ContourGT-K0+, lost volume calculation to cubic nanometer range
Energy-dispersive Spectroscopy (EDS)	Zeiss EVO MA15 SEM with INCA Energy 350 X-ray micro-analyser

4.4 Tribology study

As shown in Fig. 4.8, different mechanisms can be applied for the impact-abrasive test: a combination of steel rotating wheel (abrasion) and reciprocating/drilling (impact) in IATD machine (Fig. 4.8A) or a combination of reciprocating plunger (abrasion) and sliding (impact) in oblique sample fixed under 30°-45° angle in Fig. 4.8B [100].

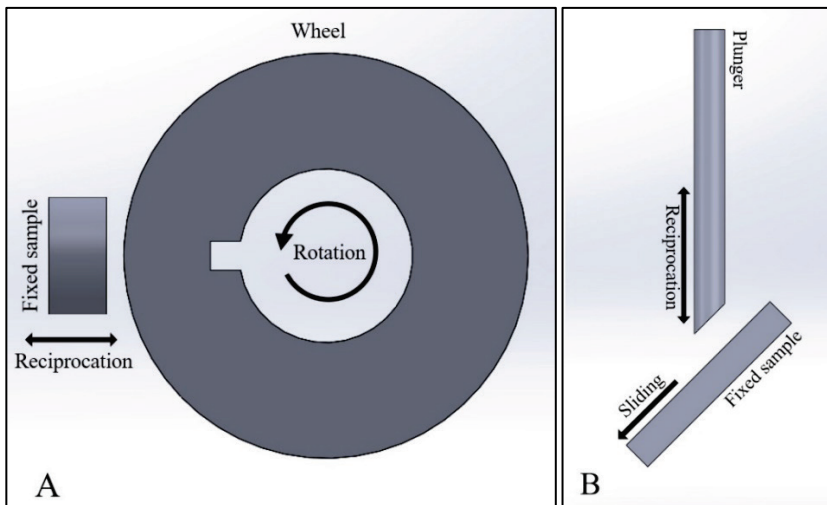


Figure 4.8 Simultaneous reciprocating and rotating motion to provide impact and abrasion test condition used at: A) TalTech University; B) AC2T Company.

Six composites including Ti6Al4V, 316L, Cr and Mo in detail are described in Table 4.2. Samples No.5 and 6 contain 316L lattice structure with 5 wt.% diamond and the rest of them are lattice-free. Mixing high strength and high corrosion resistance Ti6Al4V and high-density high ductility steel alloy 316L produces a resistant composite for relatively high strain and abrasive medium at high temperatures.

The volumetric wear rate results of the impact/abrasive test on the IATD machine (Figs. 4.7C and 4.8A) are presented in Fig. 4.9 for the samples listed in Table 4.2.

It is demonstrated that samples No.3 (lattice-free) and 6 (lattice-included) have the best wear resistance due to the presence of Cr, Ni, Mo, Al, and V elements in the 316L and Ti6Al4V alloy powders, which even promotes the excellent mechanical properties. The analysis of the results shows that: 1) Cr and Mo in sample No.2 made it more wear resistant than No.1; 2) Because of balance between Cr-Mo-Ni and diamond percentage, sample No.3 is more wear resistant than No.4.

Table 4.2 Description of samples content (in units of gram) - Lattice structures with 1 mm cell size are printed from 95 wt. % 316L and 5 wt. % of "Diamond-56 wt. % Ni". Average particle sizes are diamond 40-50 μm , Ti6Al4V 5-40 μm , 316L 30-55 μm .

No.	Diamond (56 wt. % Ni)	Diamond (30 wt. % Ni)	Ti6Al4V	316L	Cr	Mo	Lattice
1	8		4	4			
2	8		3.5	3.5	0.5	0.5	
3		6	5	5			
4		6	4.5	4.5	0.5	0.5	
5	8		3	3	0.5	0.5	4
6		6	4	4	0.5	0.5	4

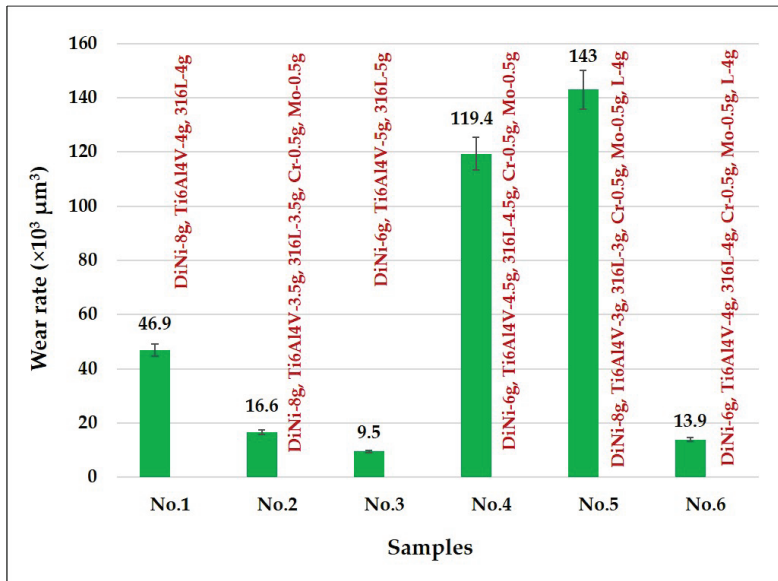


Figure 4.9 Wear rate of samples during impact-abrasive test measured by 3D OSP (Di=diamond, Ni=nickel, Cr=chromium, Mo=molybdenum, and L=lattice) [Publication 1].

Conclusions

The present study is an attempt to introduce combined SLM-SPS approaches mainly to optimize the production of wear and impact resistant materials by the combination of selective laser melting and spark plasma sintering. The current work seeks to address the following topics in industry focused fields:

- New design by functionally gradient lattice in multi-layers enables higher weldability/ductility at the bottom layer (pure metal) and higher hardness at the top (pure ceramic or hard material). Position of the metal-diamond composite structure in the desired location (continuous change from 100% metal to almost 100% hard reinforcement in uniaxial or circumferential direction) in the FGL structure was achieved.
- For the first time, it was shown that adding 10 wt.% PCD particles in the 316 L or Ti6Al4V powders results in slightly brittle scaffolds (in comparison to, e.g., 5 wt.% PCD) due to the weaker intersection of struts (specially in thinner struts) because of insufficient amount of metal.
- Adding a higher content of transition/bonding metals (Mo, Cr and Ni) guarantees higher impact-abrasive resistance of the composite, along with the metal-coated diamond particles. A balance content between diamond powders and these bonding metals is pivotal in both lattice-free and lattice-included structure types.
- The SLM manufactured Ti6Al4V lattice was filled with TiO₂-Ag powders and then consolidated by SPS. Compression strength and damage tolerance of the composites were shown to increase significantly as compared to plain TiO₂-Ag ceramics (without lattice). For Plain ceramic, fracture occurs in 250 MPa, whereas, 2 mm unit cell lattice can postpone the strength to 600 MPa.
- Adding uniform metallic lattice to ceramic silver-doped titania material decreased the antibacterial effect compared with unreinforced ceramics. To overcome such a drawback, coating or filling of the surface of the sample with plain ceramic is preferable.
- Also, the mechanical and biomedical properties of five types of scaffolds have been investigated as lightweight metallic structures, namely, rectangular, primitive, lattice, gyroid and honeycomb. Rectangular scaffold is supposed to transport oxygen and convey the fluid, whereas, honeycomb is suggested for the growth of cells. Ti6Al4V SLM manufactured product can be sintered along with CaSiO₃ in SPS for load bearing and bone replacements.

Future works

Based on the results gained in our recent study, the following goals can be summarized for upcoming works:

- I. The effect of unit cells and strut diameters on the ductility and impact absorption will be studied.
- II. In the current study, mainly diamond was applied as hard reinforcement for different applications, while it is possible to use c-BN or WC-Co, etc.
- III. Instead of metal-ceramic cermet composite, it is suggested to use metal-metal hybrid composite for highest ductility and aerospace applications.
- IV. Different additive manufacturing powders/lattices can be considered to be filled by hard materials as binder metal alloy, including Ni-based (Inconel625 or Inconel718), Co-based (CoCrMo or CoCrW), Cu-based (CuNi2SiCr or Cu15NiSn) or Fe-based (high toughness type 1.2709 or high tensile strength type 1.4542).
- V. Simulation study of other mechanical characterization of 3D printed structures, i.e., densification, brittleness, fracture, fatigue and crack propagation.

References

- [1] D. Herzog, V. Seyda, E. Wycisk, C. Emmelmann, Additive manufacturing of metals, *Acta Materialia* 117 (2016) 371-392.
- [2] T.D. Ngo, A. Kashani, G. Imbalzano, K.T.Q. Nguyen, D. Hui, Additive manufacturing (3D printing): A review of materials, methods, applications and challenges, *Composites Part B* 143 (2018) 172-196.
- [3] J.P. Kruth, L. Froyen, J.V. Vaerenbergh, P. Mercelis, M. Rombouts, B. Lauwers, Selective laser melting of iron-based powder, *Journal of Materials Processing Technology* 149 (2004) 616-622.
- [4] M. Mazur, M. Leary, M. McMillan, S. Sun, D. Shidid, M. Brandt, Mechanical properties of Ti6Al4V and AlSi12Mg lattice structures manufactured by Selective Laser Melting (SLM), *Laser Additive Manufacturing* (2017) 119-161.
- [5] A. Hussein, L. Hao, C. Yan, R. Everson, P. Young, Advanced lattice support structures for metal additive manufacturing, *Journal of Materials Processing Technology* 213, (2013) 1019-1026.
- [6] Y. Wang, L. Zhang, S. Daynes, H. Zhang, S. Feih, M.Y. Wang, Design of graded lattice structure with optimized mesostructures for additive manufacturing, *Materials & Design* 142, (2018) 114-123.
- [7] E. Louvis, P. Fox, C.J. Sutcliffe, Selective laser melting of aluminium components, *Journal of Materials Processing Technology* 211 (2011), 275-284.
- [8] Z. Shen, M. Johnsson, Z. Zhao, M. Nygren, Spark Plasma Sintering of Alumina, *J. Am. Ceram. Soc.* 85 (2002) 1921-1927.
- [9] C. Qiu, S. Yue, N.J.E. Adkins, M. Ward, H. Hassanin, P.D. Lee, P.J. Withers, M.M. Attallah, Influence of processing conditions on strut structure and compressive properties of cellular lattice structures fabricated by selective laser melting, *Materials Science & Engineering A* 628 (2015) 188-197.
- [10] C. Yan, L. Hao, A. Hussein, D. Raymont, Evaluations of cellular lattice structures manufactured using selective laser melting, *International Journal of Machine Tools and Manufacture* 62 (2012) 32-38.
- [11] Y. Holovenko, L. Kollo, M. Jöeleht, R. Ivanov, T. Soloviova, R. Veinthal, Production of metal-ceramic lattice structures by selective laser melting and carburizing or nitriding, *Proceedings of the Estonian Academy of Sciences* 68 (2019) 131-139.
- [12] T. DebRoy, H.L. Wei, J.S. Zuback, T. Mukherjee, J.W. Elmer, J.O. Milewski, A.M. Beese, A. Wilson-Heid, A. De, W. Zhang, Additive manufacturing of metallic components-process, structure and properties, *Progress in Materials Science* 92 (2018) 112-224.
- [13] <https://setis.ec.europa.eu/> (accessed 01.05.2020).
- [14] <https://www.therobbinscompany.com/products/tunnel-boring-machines/> (accessed 01.05.2020).
- [15] <https://www.hoganas.com/surface-coating> (accessed 01.05.2020).

- [16] Y. Holovenko, M. Antonov, L. Kollo, I. Hussainova, Friction studies of metal surfaces with various 3D printed patterns tested in dry sliding conditions, *Proceedings of the Institution of Mechanical Engineers, Part J: Journal of Engineering Tribology* 232 (2018), 43-53.
- [17] E. Louvis, P. Fox, C. J. Sutcliffe, Selective laser melting of aluminium components, *Journal of Materials Processing Technology* 211 (2011) 275-284.
- [18] <https://www.slm-solutions.com/en/products/> (accessed 01.05.2020).
- [19] A. Strondl, O. Lyckfeldt, H. Brodin, U. Ackelid, Characterization and Control of Powder Properties for Additive Manufacturing, *Springer JOM* 67 (2015).
- [20] K.G. Prashanth, R. Damodaram, T. Maity, P. Wang, J. Eckert, Friction welding of selective laser melted Ti6Al4V parts, *Materials Science & Engineering A* 704 (2017) 66-71.
- [21] Anna Knaislová, Pavel Novák, Sławomir Cygan, Lucyna Jaworska, Marcello Cabibbo, High-Pressure Spark Plasma Sintering (HP SPS): A Promising and Reliable Method for Preparing Ti-Al-Si Alloys, *Materials* 2017, 10(5), 465.
- [22] K. Dash, B.C. Ray, D. Chaira, Synthesis and characterization of copper-alumina metal matrix composite by conventional and spark plasma sintering, *Journal of Alloys and Compounds* 516 (2012) 78-84.
- [23] V. Mamedov, Spark plasma sintering as advanced PM sintering method, *Powder Metallurgy* 45 (2002) 322-328.
- [24] <http://www.fct-systeme.de/en> (accessed 01.05.2020).
- [25] M.A. Khan, R.L. Williams, D.F. Williams, In-vitro corrosion and wear of titanium alloys in the biological environment, *Biomater.* 17 (1996) 2117-2126.
- [26] K. Zhuravleva; M. Boenisch, K.G. Prashanth, U. Hempel, A. Health, T. Gemming, M. Caling, S. Scudino, L. Schultz, J. Eckert, Production of porous β -type Ti-40Nb alloy for biomedical applications: Comparison of selective laser melting and hot pressing, *Mater.* 6 (2013) 5700-5712.
- [27] H. Schwab, K.G. Prashanth, L. Loeber, U. Kuehn, J. Eckert, Selective laser melting of Ti-45Nb alloy, *Metals* 5 (2015) 686-694.
- [28] H. Attar, K.G. Prashanth, L.C. Zhang, M. Calin, I.V. Okulov, S. Scudino, C. Yang, J. Eckert, Effect of powder particle shape on the properties of in situ Ti-TiB composite powders produced by selective laser melting, *J. Mater. Sci. Technol.* 31 (2015) 1001-1005.
- [29] A. B. Spierings, M. Voegtlin, T. Bauer, K. Wegener, Powder flowability characterisation methodology for powder-bed based metal additive manufacturing, *Progress in Additive Manufacturing* (2016) 9-20.
- [30] H. Galarraga, R. J. Warren, D. A. Lados, R. R. Dehoff, M. M. Kirka, P. Nandwana, Effects of heat treatments on microstructure and properties of Ti-6Al-4V ELI alloy fabricated by electron beam melting (EBM), *Materials Science & Engineering A* 685 (2017) 417-428.
- [31] C. Yan, L. Hao, A. Hussein, D. Raymont, Evaluations of cellular lattice structures manufactured using selective laser melting, *International Journal of Machine Tools & Manufacture* 62 (2012) 32-38.

- [32] J. Ping Li, J. R. de Wijn, C. A. Van Blitterswijk, K. de Groot, Porous Ti6Al4V scaffold directly fabricating by rapid prototyping: Preparation and in vitro experiment, *Biomaterials* 27 (2006) 1223-1235.
- [33] Z. H. Liu, D. Q. Zhang, S. L. Sing, C. K. Chua, L. E. Loh, Interfacial characterization of SLM parts in multi-material processing: Metallurgical diffusion between 316L stainless steel and C18400 copper alloy, *Materials characterization* 94 (2014) 116-125.
- [34] F. Velasco, W. M. Lima, N. Anton, J. Abenojar, J. M. Torralba, Effect of intermetallic particles on wear behaviour of stainless steel matrix composites, *Tribology International* 36 (2003) 547-551.
- [35] A. Buford, T. Goswami, Review of wear mechanisms in hip implants: Paper I-General, *Materials and Design* 25 (2004) 385-393.
- [36] W.S.W. Harun, M.S.I.N. Kamariah, N. Muhamad, S.A.C. Ghani, F. Ahmadd, Z. Mohamed, A review of powder additive manufacturing processes for metallic biomaterials, *Powder Technology* 327 (2018) 128-151.
- [37] B.A. Mangour, D. Grzesiak, and J.M. Yang, Rapid fabrication of bulk-form TiB₂/316L stainless steel nanocomposites with novel reinforcement architecture and improved performance by selective laser melting, *J. Alloys Compd.* 680 (2016) 480-493.
- [38] US9302945B2 United States Patent, 3-D diamond printing using a pre-ceramic polymer with a nanoparticle filler, <https://patents.google.com/patent/US9302945B2/en>.
- [39] R. M. Hooper, J. L. Henshall, A. Klopfer, The wear of polycrystalline diamond tools used in the cutting of metal matrix composites, *International Journal of Refractory Metals & Hard Materials* 17 (1999) 103-109.
- [40] J. Paulo Davim, Diamond tool performance in machining metal-matrix composites, *Journal of Materials Processing Technology* 128 (2002) 100-105.
- [41] E. A. Ekimov, N. V. Suetin, A. F. Popovich, V. G. Ralchenko, Thermal conductivity of diamond composites sintered under high pressures, *Diamond & Related Materials* 17 (2008) 838-843.
- [42] V. V. N. Reddy, B. Ramamoorthy, P. K. Nair, A study on the wear resistance of electroless Ni-P/Diamond composite coatings, *Wear* 239 (2000) 111-116.
- [43] O. Al-Ketan, R. Rowshan, R.K.A. Al-Rub, Topology-mechanical property relationship of 3D printed strut, skeletal, and sheet based periodic metallic cellular materials, *Additive Manufacturing* 19 (2018) 167-183.
- [44] D.J. Yoo, Recent trends and challenges in computer-aided design of additive manufacturing-based biomimetic scaffolds and bioartificial organs, *Int. J. Precis. Eng. Manuf.* 15 (2014) 2205-2217.
- [45] D.J. Yoo, New paradigms in cellular material design and fabrication, *Int. J. Precis. Eng. Manuf.* 16 (2015) 2577-2589.
- [46] P. Heini, L. Müller, C. Körner, R.F. Singer, F.A. Müller, Cellular Ti6Al4V structures with interconnected macro porosity for bone implants fabricated by selective electron beam melting, *Acta Biomater.* 4 (2008) 1536-1544.
- [47] T. Freyman, I. Yannas, L. Gibson, Cellular materials as porous scaffolds for tissue engineering, *Prog. Mater. Sci.* 46 (2001) 273-282.

- [48] C. Yan, L. Hao, A. Hussein, P. Young, Ti-6Al-4V triply periodic minimal surface structures for bone implants fabricated via selective laser melting, *Mechanical Behavior of Biomedical Materials* 51 (2015) 61-73.
- [49] X. Wan, A. Hu, M. Li, C. Chang, D. Mao, Performances of CaSiO₃ ceramic sintered by spark plasma sintering, *Materials Characterization* 59 (2008) 256-260.
- [50] R. Rahmani, M. Rosenberg, A. Ivask, L. Kollo, Comparison of mechanical and antibacterial properties of TiO₂/Ag ceramics and Ti6Al4V-TiO₂/Ag composite materials using combining SLM-SPS techniques, *Metals* 9 (2019) 874.
- [51] R. Rahmani, M. Antonov, L. Kollo, Y. Holovenko, P. K. Gokuldoss, Mechanical Behavior of Ti6Al4V Scaffolds Filled with CaSiO₃ for Implant Applications, *Applied Sciences* 9 (2019) 3844.
- [52] N. Kamboj, M. A. Rodríguez, R. Rahmani, P. K. Gokuldoss, I. Hussainova, Bioceramic scaffolds by additive manufacturing for controlled delivery of the antibiotic vancomycin, *Proceedings of the Estonian Academy of Sciences* (2019), 68, 185-190.
- [53] R. Rahmani, M. Antonov, N. Kamboj, Modelling of impact-abrasive wear of ceramic, metallic, and composite materials, *Proceedings of the Estonian Academy of Sciences* 68 (2019) 191-197.
- [54] R. Rahmani, M. Brojan, M. Antonov, K. G. Prashanth, Perspectives of metal-diamond composites additive manufacturing using SLM-SPS and other techniques for increased wear-impact resistance, *International Journal of Refractory Metals and Hard Materials* 88 (2020) 105192.
- [55] Y. Holovenko, L. Kollo, M. Saarna, R. Rahmani, T. Soloviova, M. Antonov, K. G. Prashanth, S. Cygan, R. Veinthal, Effect of lattice surface treatment on performance of hardmetal-titanium interpenetrating phase composites, *International Journal of Refractory Metals & Hard Materials* 86 (2020) 105087.
- [56] R. Rahmani, M. Antonov, L. Kollo, Wear Resistance of (Diamond-Ni)-Ti6Al4V Gradient Materials Prepared by Combined Selective Laser Melting and Spark Plasma Sintering Techniques, *Advances in Tribology* (2019) 5415897.
- [57] R. Rahmani, M. Antonov, L. Kollo, Selective Laser Melting of Diamond-Containing or Postnitrided Materials Intended for Impact-Abrasive Conditions: Experimental and Analytical Study, *Advances in Materials Science and Engineering* (2019) 4210762.
- [58] <https://www.materials.sandvik/en/> (accessed 01.05.2020).
- [59] <http://www.tls-technik.de/> (accessed 01.05.2020).
- [60] <http://www.vanmoppes.ch/en/> (accessed 01.05.2020).
- [61] <http://www.hoganas.com/surface-coating> (accessed 01.05.2020).
- [62] <http://www.fct-systeme.de/en> (accessed 01.05.2020).
- [63] <https://www.slm-solutions.com/en/products/machines/slmr125/> (accessed 01.05.2020).
- [64] S. Van Bael, Y. C. Chai, S. Truscello, M. Moesen, G. Kerckhofs, H. Van Oosterwyck, J.-P. Kruth, J. Schrooten, The effect of pore geometry on the in vitro biological behavior of human periosteum-derived cells seeded on selective laser-melted Ti6Al4V bone scaffolds, *Acta Biomaterialia* 8 (2012) 2824-2834.

- [65] S. Barui, S. Chatterjee, S. Mandal, A. Kumar, B. Basu, Microstructure and compression properties of 3D powder printed Ti-6Al-4V scaffolds with designed porosity: Experimental and computational analysis, *Materials Science and Engineering C* 70 (2017) 812-823.
- [66] G. Pyka, A. Burakowski, G. Kerckhofs, M. Moesen, S. Van Bael, J. Schrooten, M. Wevers, Surface Modification of Ti6Al4V Open Porous Structures Produced by Additive Manufacturing, *Advanced Engineering Materials* 14 (2012) 363-370.
- [67] <http://www.nfm-technologies.com/> (accessed 01.05.2020).
- [68] T. Camus and S. Moubarak, Maintenance Robotics in TBM Tunnelling, ISARC, in *Proceedings of the International Symposium on Automation and Robotics in Construction* (2015).
- [69] M. Antonov, R. Veinthal, D-L. Yung, D. Katusin, I. Hussainova, Mapping of impact-abrasive wear performance of WC-Co cemented carbides, *Wear* 332-333 (2015) 971-978.
- [70] K.G. Prashanth, J. Eckert, Formation of metastable cellular microstructures in selective laser melted alloys, *J. Alloys Compd.* (2017) 27-34.
- [71] O. Al-Ketan, M.A. Assad, R.K. Abu Al-Rub, Mechanical properties of periodic interpenetrating phase composites with novel architected microstructures, *Compos. Struct.* 176 (2017) 9-19.
- [72] J. Kadkhodapour, H. Montazerian, A.C. Darabi, A. Anaraki, S. Ahmadi, A. Zadpoor, S. Schmauder, Failure mechanisms of additively manufactured porous biomaterials: effects of porosity and type of unit cell, *J. Mech. Behav. Biomed. Mater.* 50 (2015) 180-191.
- [73] E. Badisch, S. Ilo, R. Polak. Multivariable modeling of impact-abrasion wear rates in metal matrix-carbide composite materials. *Tribol. Lett.* 36 (2009) 55-62.
- [74] L. Zhang, S. Feih, S. Daynes, S. Chang, M.Y. Wang, J. Wei, W.F. Lu, Energy absorption characteristics of metallic triply periodic minimal surface sheet structures under compressive loading. *Addit. Manuf.* 23 (2018) 505-515.
- [75] C. Zheng, F. Wang, X. Cheng, K. Fu, J. Liu, Y. Wang, T. Liu, Z. Zhu, Effect of microstructures on ballistic impact property of Ti-6Al-4V targets, *Materials Science & Engineering A* 608 (2014) 53-62.
- [76] K. Senthil, M. A. Iqbal, Effect of projectile diameter on ballistic resistance and failure mechanism of single and layered aluminum plates, *Theoretical and Applied Fracture Mechanics* 67-68 (2013) 53-64.
- [77] J.K. Holmen, J. Johnsen, S. Jupp, O.S. Hopperstad, T. Børvik, Effects of heat treatment on the ballistic properties of AA6070 aluminium alloy, *International Journal of Impact Engineering* 57 (2013) 119-133.
- [78] W. Liu, Z. Chen, X. Cheng, Y. Wang, A. R. Amankwa, J. Xu, Design and ballistic penetration of the ceramic composite armor, *Composites Part B* 84 (2016) 33-40.
- [79] K.C. Nune, A. Kumar, R.D.K. Misra, S.J. Li, Y.L. Hao, R. Yang, Functional response of osteoblasts in functionally gradient titanium alloy mesh arrays processed by 3D additive manufacturing, *Colloids and Surfaces B: Biointerfaces* 150 (2017) 78-88.

- [80] M.A. Surmeneva, R.A. Surmenev, E.A. Chudinova, A. Koptioug, M.S. Tkachev, S.N. Gorodzha, L.E. Rännar, Fabrication of multiple-layered gradient cellular metal scaffold via electron beam melting for segmental bone reconstruction, *Materials and Design* 133 (2017) 195-204.
- [81] D. Khrapov, M. Surmeneva, A. Koptioug, S. Evsevleev, F. Léonard, G. Bruno, R. Surmenev, X-ray computed tomography of multiple-layered scaffolds with controlled gradient cell lattice structures fabricated via additive manufacturing, *Journal of Physics* 1145 (2019) 1-7.
- [82] D.C. Hofmann, S. Roberts, R. Otis, J. Kolodziejska, R.P. Dillon, J-k Suh, A.A. Shapiro, Z-K Liu, J-P. Borgonia, Developing Gradient Metal Alloys through Radial Deposition Additive Manufacturing, *Scientific reports* (2014) 1-8.
- [83] H. M. Sung-Suh, J. R. Choi, H. J. Hah, S. M. Koo, Y. C. Bae, Comparison of Ag deposition effects on the photocatalytic activity of nanoparticulate TiO₂ under visible and UV light irradiation, *Journal of Photochemistry and Photobiology A: Chemistry* 163 (2004) 37-44.
- [84] H-C. Kim, H-K. Park, I-J. Shon, I-Y. Ko, Fabrication of ultra-fine TiO₂ Ceramics by a high-frequency induction heated sintering method, *Journal of Ceramic Processing Research* 7 (2006) 327.
- [85] B. Vandenbroucke, J-P. Kruth, Selective laser melting of biocompatible metals for rapid manufacturing of medical parts, *Rapid Prototyping* 13 (2007) 196-203.
- [86] C. He, Y. Yu, X. Hu, A. Larbot, Influence of silver doping on the photocatalytic activity of titania film, *Applied Surface Science* 200 (2002) 239-247.
- [87] L. Zhao, H. Wang, K. Huo, L. Cui, W. Zhang, H. Ni, Y. Zhang, Z. Wu, P. K. Chu, Antibacterial nano-structured titania coating incorporated with silver nanoparticles, *Biomaterials* 32 (2011) 5706-5716.
- [88] M. Visnapuu, M. Rosenberg, E. Truska, E. Nommiste, A. Sutka, A. Kahru, M. Rahn, H. Vija, K. Orupold, V. Kisand, A. Ivask, UVA-induced antimicrobial activity of ZnO/Ag nanocomposite covered surfaces, *Colloids and Surfaces B: Biointerfaces* 169 (2018) 222-232.
- [89] R. Bernasconi, E. Carrara, M. Hoop, F. Mushtaq, X. Chen, B. J. Nelson, Salvador Pané, Caterina Credi, Marinella Levi, Luca Magagnin, Magnetically navigable 3D printed multifunctional micro devices for environmental applications, *Additive Manufacturing* 28 (2019) 127-135.
- [90] G.E. Ryan, A.S. Pandit, D.P. Apatsidis, Porous titanium scaffolds fabricated using a rapid prototyping and powder metallurgy technique, *Biomaterials* 29 (2008) 3625-3635.
- [91] William E. Frazier, Metal Additive Manufacturing: A Review, *Journal of Materials Engineering and Performance* 23 (2014) 1917-1928.
- [92] *Filters and filtration handbook*, Ken Sutherland, Fifth edition, 2008.
- [93] A. Kudo, Y. Miseki, Heterogeneous photocatalyst materials for water splitting, *Chem. Soc. Rev.* 38 (2009) 253-278.
- [94] N.S. Leyland, J.P. Carroll, J. Browne, S.J. Hinder, B. Quilty, S.C. Pillai, Highly Efficient F, Cu doped TiO₂ anti-bacterial visible light active photocatalytic coatings to combat hospital-acquired infections, *Sci. Rep.* 6 (2016) 24770.

- [95] T.S. Balint, J.P. Melchiorri, Making the Venus Concept Watch 1.0, *Acta Astronautica* 101 (2014) 138-150.
- [96] H. Li, J. Chang, Fabrication and characterization of bioactive wollastonite/PHBV composite scaffolds, *Biomaterials* 25 (2004) 5473-5480.
- [97] L.E. Murr, E.V. Esquivel, S.A. Quinones, S.M. Gaytan, M.I. Lopez, E.Y. Martinez, F. Medina, D.H. Hernandez, E. Martinez, J.L. Martinez, Microstructures and mechanical properties of electron beam-rapid manufactured Ti-6Al-4V biomedical prototypes compared to wrought Ti-6Al-4V, *Mater. Charact.* 60 (2009) 96-105.
- [98] X. Wan, A. Hu, M. Li, C. Chang, D. Mao, Performances of CaSiO₃ ceramic sintered by spark plasma sintering, *Mater. Charact.* 59 (2008) 256-260.
- [99] ASTM G65-04 Standard Test Method for Measuring Abrasion Using the Dry Sand/Rubber Wheel Apparatus, *Annual Book of ASTM Standards* (2004).
- [100] E. Badisch, C. Katsich, H. Winkelmann, F. Franek, M. Roy, Wear behaviour of hardfaced Fe-Cr-C alloy and austenitic steel under 2-body and 3-body conditions at elevated temperature, *Tribology International* 43 (2014) 1234-1244.

Acknowledgment

This thesis and related papers would not have been possible without support, encouragement and guidance from my supervisor *Maksim Antonov* and my co-supervisor *Lauri Kollo*.

I would like to express my gratitude to *Miha Brojan* from Laboratory of Nonlinear Mechanics, University of Ljubljana, Slovenia, and *Ewald Badisch* from AC2T Research GmbH, Wiener Neustadt, Austria, for providing me an opportunity to improve my research skills in their institutes during my PhD mobility supported by Dora Plus program.

I am indebted to my parents, family and friends for their support and helping. In addition, I am grateful to *Nikhil Kamboj*, *Marek Tarraste*, *Yaroslav Holovenko*, *Rahul Kumar*, *Roman Ivanov*, *Le Liu*, *Tatevik Minasyan*, and *Navid Alinejadian* for common working, sharing the experiences and friendship. I am also thankful to *Prashanth Konda Gokuldoss*, *Hans Vallner*, *Kristo Karjust*, *Fjodor Sergejev*, *Irina Hussainova* and *Priit Kulu* for valuable advice and assistance during the study. I would like to thank *Rainer Traksmaa* for the help with XRD patterning, *Heinar Vagiström* for the help with preparation and coating of samples and *Mart Viljus* for the help with EDS mapping.

This work was supported by *TalTech* University scholarship, the Estonian Ministry of Higher Education and Research under Projects (IUT19-29, ETAG18012 and PRG643), project number 2014-2020.4.01.16-0183 (Smart Industry Centre), European Regional Funds through the project MOBERC15 and TalTech base finance project (B56 and SS427).

Abstract

Combination of SLM-SPS approaches for tribological, antibacterial and biomaterial applications

The present study is focused on a new combined approach to fabricate parts with increased wear and impact resistance for use in industrial applications, such as tunnelling, mining, as well as in antibacterial (in-vitro) and biomedical (in-vivo) areas.

In this case, a combination of selective laser melting (SLM) and spark plasma sintering (SPS) to 3D print functionally graded lattices (FGL) that are later filled/consolidated with metals, ceramics, hard material composites was used.

FGL structures due to their novelties, desired distribution of metal and ceramic in longitudinal and/or circumferential directions, fast prototyping, and almost full densification has been introduced and developed as an outcome of the modern powder metallurgy field.

3D printing of gradient structure along with post-processing procedures such as nitriding, chromium coating, blasting by alumina, filling by biocompatible ceramics, covering by antibacterial surface, and hard-materials adding to lattice structures are introduced in this thesis and related papers.

Laboratory-developed Impact-abrasive tribo-device (IATD), scanning electron microscopy (SEM), X-ray diffraction (XRD), energy-dispersive spectroscopy (EDS), vacuum furnace nitriding (VFN) and optical surface profiler (OSP) were used to prepare, test and characterize samples.

In addition, nonlinear finite element simulation was developed with the help of SolidWorks, Ansys, and Comsol Multiphysics software and explicit dynamic (AUTODYN solver) under impact, abrasion, and compression mode.

Our coupled experimental and analytical results show that the FGL structure allows a more accurate and favorable distribution of diamond particles across the structure and our finite element simulations showed increased ductility and impact energy absorption due to a more uniform distribution of stresses throughout the volume of sample.

Keywords: Additive manufacturing; Selective laser melting; Spark plasma sintering; Ti6Al4V and 316L lattice structures; Metal-diamond 3D printing; Polycrystalline diamond; Tunnel boring machine; Wear resistance; Finite element simulation; antibacterial and photoactivity applications.

Lühikokkuvõte

Kombineeritud SLM-SPS meetod triboloogiliste, antibakteriaalsete ja biosobivate materjalide valmistamiseks

Käesolev uuring keskendub suurenenud kulumis- ja löögikindlusega osade uuele kombineeritud valmistusviisile, mida võib kasutada tööstuslikes rakendustes, näiteks tunneliehituses, kaevandamisel, samuti ka antibakteriaalses (in vitro) keskkonnas ja biomeditsiini (in vivo) alal.

Selektiivse laserisulatamise (SLM) ja sädepaagutuse (SPS) kombinatsiooni kasutati funktsionaalselt moodustatud struktuuride (FGL) 3D-printimiseks (kolmemõõtmeline printimine), mis hiljem täidetakse metalli, keraamika või kõvasulami pulbriga ja paagutakse komposiitmaterjali valmistamiseks.

Kaasaegse pulbermetallurgia valdkonna tulemused on võimaldanud välja töötada ja kasutusele võtta FGL struktuurid tänu nende uudsusele, metalli ja keraamika vastavale jaotusele detaili piki- ja / või ristisuunas, kiirele prototüüpimisele ja peaaegu täielikule tihendamisele (pooride puudumisele).

Selles dissertatsioonis ja vastavates seotud artiklites tutvustatakse gradientstruktuuri 3D-printimist koos järeltöötlusprotseduuridega nagu nitreerimine, kroomikihiga katmine, alumiiniumoksiidiga suruõhuga pritsimine (puhastamine), biosobiva keraamikaga täitmine, antibakteriaalse pinnaga katmine ja kõvade faaside lisamine võrestruktuuridesse.

Katsekehade (katsematerjalide) töötlemiseks, katsetamiseks ja iseloomustamiseks kasutati laboratorset löök-abrasiivset triboseadet (IATD), skaneerivat elektronmikroskoopi (SEM), röntgendifraktsiooni (XRD), röntgenmikroanalüüsi (EDS), nitreerimist vaakumahjus (VFN) ja optilist pinnaprofiili mõõteriista (OSP).

Löök-, abrasiiv- ja survetingimused modelleeriti mittelineaarsete lõplike elementide meetodite abil (tarkvaraga SolidWorks, Ansys ja Comsol Multiphysics) ja ekplitsiidse dünaamilise tarkvaraga (AUTODYN).

Omavahel seotud eksperimentaalsete ja analüütiliste uuringute tulemused näitavad, et FGL-struktuur võimaldab teemandi (või muu kõvafaasi) osakesi jaotada täpsemini ja optimaalsemalt üle kogu materjali struktuuri; lõplike elementide simulatsioonid näitasid suurenenud plastsust ja löögienergia summutamist pingete ühtlasema jaotuse tõttu kogu materjali mahus.

Funktsionaalselt moodustatud struktuuride kasutamine võimaldab valmistada mitmekihilise (gradientse) materjali, mida on võimalik keevitada küljest, kus on maksimaalne metalli sisaldus, kuid maksimaalne kõvadus ja kulumiskindlus tekitakse teistes detaili kohtades (kus on maksimaalne keraamilise või muu kõvafaasi sisaldus). Saavutati metall-teemant FGL komposiitstruktuur, mille sees ühest küljest teiseni (piki- või ristisuunas) teemandi (pinnatud, adhesiooni parandamiseks) sisaldus 0 kuni 100 % pidevalt muutus (samal ajal metalli sisaldus muutus 100 kuni 0 % ni).

Esmakordselt näidati, et 10-massiprotsendiliste teemantosakeste lisamisel 316L või Ti6Al4V pulbritele saadakse habras võrgustik, kuid 5 massiprotsendiga struktuur on tunduvalt parem, eriti prinditud elementide ristumiskohtades.

Suurema maatriksmetallide (Mo, Cr ja Ni) ja/või metallkattega teemantosakeste lisamine tagab komposiidi suurema löögikindluse. Teemandipulbrite ja nende maatriksmetallide omavaheline optimaalne sisaldus on otsustav faktor mõlemas nii võrgustikuga kui ka ilma võrgustikuta struktuuritüüpides.

Ti6Al4V võrgustik valmistati SLM meetodiga, täideti TiO₂-Ag pulbritega ja seejärel paagutati SPS-ga. Komposiitmaterjalide survetugevus ja kahjutaluvus suurenesid märgatavalt võrreldes tavalise TiO₂-Ag keraamikaga (ilma tugevdava võrgustikuta). Survekatse jooksul komposiitmaterjal püsis tervikuna ja fragmentide eraldumine tekkis ainult 25 % deformatsiooni puhul.

Ühtlase tugevdava metallvõrgustiku lisamine keraamilisele hõbedaga-legeeritud titaan dioksiid materjalile vähendas antibakteriaalset toimet. Sellise puuduse ületamiseks on eelistatav moodustada komposiitmaterjal, mille sees võrgustik ei ulatu pinnani (välispind koosneb monoliitkeraamikast).

Samuti on uuritud viit tüüpi (ristkülikukujulisi, primitiivseid, võre-, güroid- ja kärgstruktuure) luu implantaadi 3D printitud struktuuri (poorsed, kõrge eritugevusega) mehaanilisi ja biomeditsiinilisi omadusi. Ristkülikukujuline 3D printitud struktuur sobib paremini hapniku ja vedeliku transportimiseks (levitamiseks), kuid rakkude kasvatamiseks soovitatakse kärgstruktuuri. 3D printimisega valmistatud Ti6Al4V struktuuri (võrgustiku) saab paagutada koos CaSiO₃-ga SPS meetodiga luu implantaatideks või osaliseks luude asendamiseks.

Märksõnad: Kolmemõõtmeline printimine; Selektiivne lasersulatus; Sädepaagutus; Ti6Al4V ja 316L võrestruktuurid; Metall-teemant komposiitmaterjali 3D-printimine; Polükristalne teemant; Metrootunnelite läbinduskombain; Kulumiskindlus; Lõplike elementide simulatsioon; antibakteriaalsed ja fotoaktiivsed rakendused.

Appendix

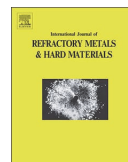
Publication I

R. Rahmani; M. Brojan; M. Antonov; K. G. Prashanth; Perspectives of metal-diamond composites additive manufacturing using SLM-SPS and other techniques for increased wear-impact resistance, International Journal of Refractory Metals and Hard Materials 88 (2020) 1-13.



Contents lists available at ScienceDirect

International Journal of Refractory Metals & Hard Materials

journal homepage: www.elsevier.com/locate/IJRMHM

Perspectives of metal-diamond composites additive manufacturing using SLM-SPS and other techniques for increased wear-impact resistance

Ramin Rahmani^{a,b,*}, Miha Brojan^b, Maksim Antonov^a, Konda Gokuldoss Prashanth^{a,c,d}^a Department of Mechanical and Industrial Engineering, Tallinn University of Technology, Ehitajate tee 5, 19086 Tallinn, Estonia^b Laboratory for Nonlinear Mechanics, Faculty of Mechanical Engineering, University of Ljubljana, Askerceva 6, SI-1000 Ljubljana, Slovenia^c Erich Schmid Institute of Materials Science, Austrian Academy of Science, Jahnstraße 12, A-8700 Leoben, Austria^d CBCMT, School of Mechanical Engineering, Vellore Institute of Technology, 632014, Tamil Nadu, India

ARTICLE INFO

Keywords:

Selective laser melting
 Spark plasma sintering
 Hard material 3D printing
 Metal-diamond powders
 Wear-impact resistance
 Finite element simulation

ABSTRACT

In this paper, a new route is introduced to fabricate parts with increased wear and impact resistance for use in tunneling and mining applications. A combination of selective laser melting (SLM) and spark plasma sintering (SPS) to 3D print functionally graded lattices (FGL) that are later filled with metal-diamond composites was used. It was demonstrated that a cellular lattice plays an important role in the consolidation of diamond particles. Impact-abrasive laboratory experiments with tribological device, developed in-house, were carried out to characterize the fabricated samples. The results show that the balance of nickel, molybdenum, and chromium significantly affects the performance of the fabricated specimens. The addition of a higher content of Mo–Cr, Ni and coated diamond particles guarantees higher impact-abrasive resistance of the composite. Our experimental results show that the FGL structure allows a more accurate distribution of diamond particles (variable metal/refractory material content) across the structure and our finite element simulations showed increased ductility and impact absorption ability due to a more uniform distribution of stresses throughout the volume.

1. Introduction

Additive manufacturing has an immense potential to assist in the development of new classes of materials with precisely engineered microstructures that can work in extremely harsh conditions. For example, a combination of selective laser melting (SLM) of metals and spark plasma sintering (SPS) of metallic, ceramic or composite materials enables the production of composites using functionally graded lattice (FGL) structures with continuous metal lattices for optimized strength and sintered/embedded hard reinforcements for optimized hardness [1,2]. A cost-efficient drag bit for deep geothermal drilling or tunnel boring machines [3] in which harsh impact-abrasive conditions apply is an excellent example of application to test the limits of additive manufacturing (AM) methods, such as 3D printing of metallic and composite materials with diamond inclusions [4,5].

SLM is a rapid prototyping technology based on the powder bed fusion process with the high heating and cooling rate (10^4 – 10^6 K/s [6]) that enables the creation of complicated parts and assemblies directly from computer-aided design (CAD) models. The feeding mechanism is used to deposit agglomerated powders in front of a rubber wiper that sweeps the powder on the building area to form a thin uniform layer.

The minimal possible thickness of the spread layer depends on flow-ability, sphericity and wiper height adjustment. The laser then pulses and heats the powder on the building area to form a solid object. With this system, the objects are built layer by layer on e.g. Ti6Al4V platform with the help of a servomotor driven elevator that moves downwards by a distance equal to the layer thickness and after every wiping and sintering sequence. The process is carried out in an argon protective environment with a pressure of 6 mbar and an oxygen level < 0.5% [7]. Powders are deposited, melted and consolidated layer by layer with the prescribed thickness (e.g. 0.25–0.5 μ m for SLM50) to manufacture dense layers and CAD designed dimensions. The basis of the SLM classification is usually platform sizes e.g. SLM50, SLM280 or SLM500 (that corresponds to 50, 280 and 500 mm and is prescribing the maximum size of the object that is possible to print) [8]. Unmelted/non-consolidated powders outside the platform, wiped out during the job or after finishing the job can be recycled which is an advantage of AM technology regarding powder consumption [9]. Another benefit of SLM is the ability to use a wide scope of metal, ranging from Ti-, Fe-, Al-, Ni-, Co- to Cu-based powders [10]. Parts fabricated by this technology show better fatigue resistance, fracture toughness and tribological properties compared to their cast counterparts [11].

* Corresponding author at: Department of Mechanical and Industrial Engineering, Tallinn University of Technology, Ehitajate tee 5, 19086 Tallinn, Estonia
 E-mail addresses: ramin.rahmaniahrajanjani@taltech.ee, ramin.rahmaniahrajanjani@gmail.com (R. Rahmani).

<https://doi.org/10.1016/j.ijrmhm.2020.105192>

Received 18 December 2019; Accepted 9 January 2020

Available online 10 January 2020

0263-4368/© 2020 Elsevier Ltd. All rights reserved.

The SPS process is a relatively new solid consolidation sintering technique with simultaneous application of a low voltage, high pulse current, and uniaxial pressure-assisted punch electrodes. The key advantages of this new sintering method over the hot isostatic pressing (HIP) method include very high densities obtained in a short time and a wide-ranging sintering temperature (300–2200 °C), fast heating rate (1000 °C/min) and cooling rate (300 °C/min) compared to the conventional powder metallurgy, e.g. hot isostatic pressing. The DC pulsed electrical direct current in a vacuum chamber generates the spark discharge and rapid Joule heating through graphite mold and powder compact (tungsten carbide molds can be used for hard materials powders) [12,13]. The graphite molds and punches control pressure, as well as thermocouple control (TC) or pyrometer control (PC), applies temperature precise control [14]. SPS is developed for the consolidation of a wide range of different materials, such as metals, ceramics, and composites in different dimensions (usually disk-shaped) and with high density.

The flowability (sphericity), particle size (nano or micro), density, composition, melting points, avalanche angles, inter-particle forces, powder surface fractal, etc., give valuable information about the applicability of powders [15]. For example, due to its high strength-to-weight ratio argon atomized Ti6Al4V powder is widely used in bio-material, aerospace and additive manufacturing applications [16]. Grade 5 titanium alloy containing 5.5–6.75 wt% aluminum and 3.5–4.5 wt% vanadium with 4.43 g/cm³, particle size ≤45 μm and melting point ≥1604 °C has excellent strength, low density and high corrosion resistance. The 316 L powder (with density 7.95 g/cm³) is an austenitic low-carbon non-magnetic stainless steel containing 16–18 wt % chromium, 10–14 wt% nickel and 2–3 wt% molybdenum. Apart from its biomedical and chemical applications, it is outstanding for its excellent fluidity (of powder) in an SLM approach, corrosion resistance and strength at high temperature [17]. Excellent mechanical properties and corrosion resistance of 316 L and Ti6Al4V alloys motivated the researchers to mix them and promote their characteristics [18–21].

Printing diamond particles remains a big challenge. So far, it is only reported as a patent [22]. However, printing diamond particles mixed with metals is already possible, but still in progress [2,23,24]. One such route is via metal-coated polycrystalline diamond (PCD) which is also used in our study [25,26]. The coating usually consists of cobalt, nickel,

aluminum and copper, and a wide variety of carbides, nitrides, ceramics and metal alloys. It is commonly used for its good thermal conductivity in electronic components and in applications where wear resistance is important [27,28]. It was shown, for example, that 316 L-diamond lattice printed structures or sintered diamond along with Ti6Al4V lattice via SPS route has provided uniform distribution of diamond particles and consequently lower wear rates and improved crack resistance [23].

In this paper, we show a novel approach for printing diamond included lattice/matrix structures for the potential use in tunneling and mining applications. We apply a combination of SLM and SPS techniques and propose an axial FGL structure with a dense metal region at the bottom for better weldability/ductility, gradient interlayer filled Ti6Al4V-diamond composite and plain Ni-coated diamond at the top for higher hardness to improve wear-impact resistance. To analyze the influence of the geometry we vary the cell size, strut diameter and volume fraction of the specimen. We show that a cellular lattice structure plays an important role in the consolidation of diamond particles. By introducing a lattice structure, the diamond particles are kept in situ as oppose to the solid printing the 316 L-diamond composite which induces depositions of diamond particles at the bottom of each layer. Nitriding (and/or carburizing), chromium coating, blasting/cleaning by alumina nanopowders, diamond mixing is applied in the recent study as metallic lattice structures post-processing after SLM route. The impact-abrasion tribo-device (IATD), 3D optical surface profiler (OSP), scanning electron microscopy (SEM) and energy-dispersive spectroscopy (EDS) were applied to estimate how well the produced materials can withstand the wear and impact conditions. Demonstration of impact resistance of the specimen in distinct conditions (plain and lattice-included samples) is presented also via finite element simulations.

2. Methods and materials

Functionally graded cellular metallic lattices manufactured by SLM and filled with diamond particles or WC-Co hardmaterials which are sintered with the SPS are proposed to fabricate parts with improved abrasion and impact resistance. A sketch of such FGL structure with a dense metal region at the bottom for better weldability/ductility,

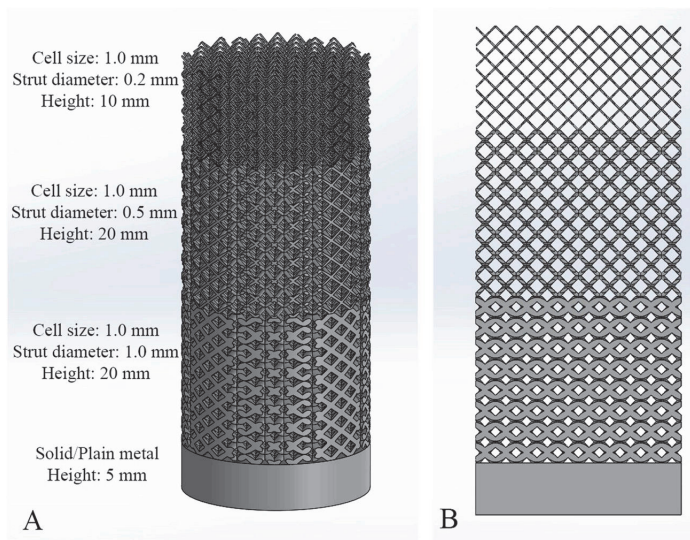


Fig. 1. FGL structure with a dense metal region at the bottom for better weldability/ductility, interlayers gradient metallic and wear resistant at the top. A) Sample with 20 mm diameter proper for SPS mold, B) cross sectional view.

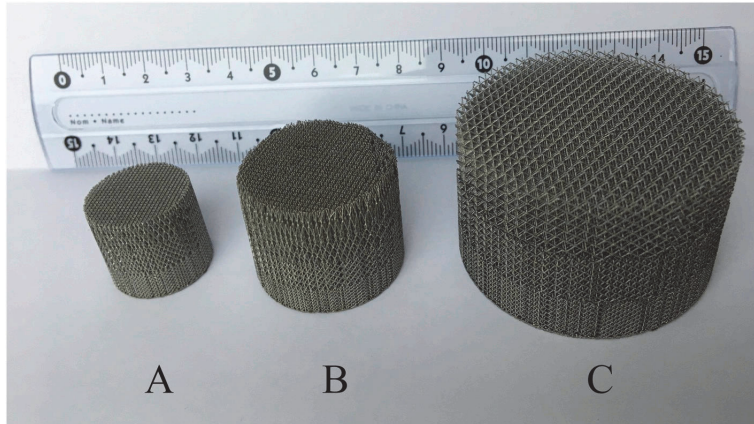


Fig. 2. Demonstration of the possibility of fabrication of Ti6Al4V lattices of required size functionally graded from bottom to top in three volume fraction stages (42, 30, and 16%). The diameters and heights of samples are: A) $\text{Ø}20 \times 18$ mm, B) $\text{Ø}30 \times 24$ mm, C) $\text{Ø}50 \times 30$ mm.

gradient interlayers (metal-ceramic composite) and wear resistant (high hardness) in top is depicted in Fig. 1.

These scaffolds can be filled with various types of hard materials, ceramics, metals or oxides for biocompatibility, antibacterial and tribological applications [29–32]. In Fig. 2, we show three fabricated functionally graded lattices (FGL) made from Ti6Al4V by the SLM technique. The structure of the specimens is denser (higher volume fraction) at the bottom and decreases in three stages towards the top, with 42%, 30% and 16% volume fraction of metal respectively. The outer dimensions of the specimens are given in the figure caption.

Fig. 3 shows four structures made from the same material and the same printing technique with a continuous cell size across the whole specimen. The first two specimens have the same strut diameter and different cell size, whereas the last two have the same cell size but different strut diameter. All the specimens shown in this figure were nitrided in a vacuum nitriding furnace (VNF, under nitrogen gas flowing with $10^\circ\text{C}/\text{min}$ heating rate and 90 min holding time at 900°C) to fabricate TiN phase surrounded lattice beams [23,33]. It is known that, nitrided Ti6Al4V scaffolds have higher brittleness and collapse under lower load; therefore, it preferred mainly for applications with

followed filling by additional powder and sintering [23,33]. As nitriding takes place in a furnace with constant Ni-flow, the depth of treated material during the process is independent from the volume fraction of Ti6Al4V.

On the other hand, the process of chrome plating via chemical vapor deposition (CVD) is influenced by volume fraction of lattice material. In Fig. 4 three specimens with various lattice cell sizes made from 316 L powder are shown. Even though the CVD reactor conditions were constant for all samples, it is evident that chromium deposition/penetration through the lattice struts is not complete for the specimen with smaller cell sizes (i.e. for higher material volume fractions). Note that with the chrome plating process the metal is protected against corrosion and fatigue and remains sufficiently ductile.

Both metal alloys Ti6Al4V and 316 L used to print the specimens in Figs. 2-4 are ductile scaffolds. With the same technology, it is possible to print also hard materials. For example, one can print Rockit 701 powder, produced by Hoganas [4], with the element composition Fe 76.3%, W 9.5%, Cr 4%, Nb 1.6%, C 1%, Ti 0.6% and 7% other elements (SEM image of the particles is shown in Fig. 5A). It is convenient for printing impact, abrasive and crack resistant products. Apart from

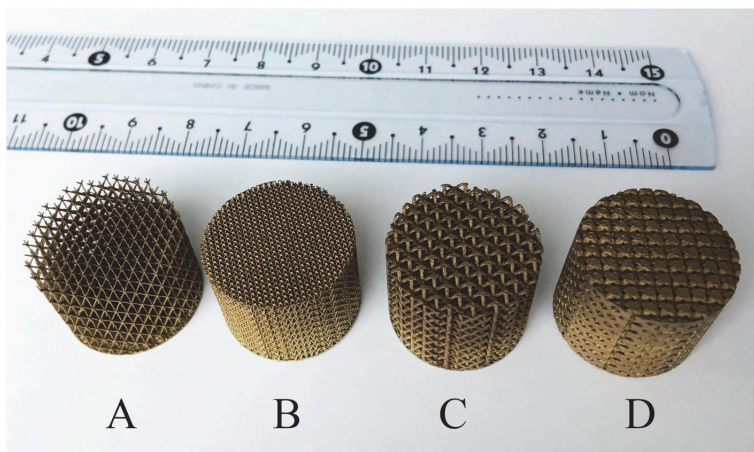


Fig. 3. Nitrided Ti6Al4V lattice structures with varied cell size, strut diameter and approx. Volume fraction: A) 1.5 mm, 0.2 mm, 12%, B) 0.75 mm, 0.2 mm, 26%, C) 1 mm, 0.5 mm, 36%, D) 1 mm, 1 mm, 60%, respectively. All specimens have 20 mm diameter and 15 mm height.

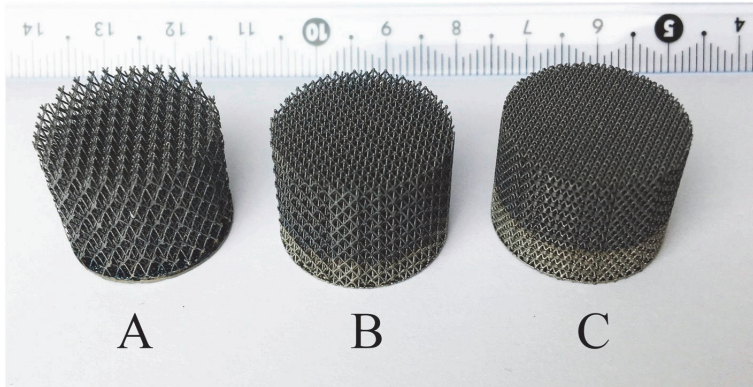


Fig. 4. Chrome plated 316 L lattice structures with varied cell sizes and volume fraction: A) 1.5 mm and 12%, B) 1.0 mm and 19%, and C) 0.75 mm and 26%. The specimens are 20 mm in diameter and 15 mm in height.

sintering tungsten inside 316 L scaffolds, direct 3D printing of Fe-9.5 wt% W is already feasible for consolidating hardmaterial particles in favorable places (see for instance Fig. 5B).

Moreover, it is also possible to consolidate diamond particles in situ [2,23,24]. 3D printed struts with mixture of Ti6Al4V and diamond with 5 wt% of diamond and 10 wt% of diamond are shown in Fig. 6A and B. In the case of 10 wt% diamond mixture, the connection/cohesion of the struts is relatively weak (due to weaker bonding between diamond and metals) which leads to a more brittle scaffold structure. The problem can be solved by increasing the strut diameter. As shown in Fig. 7, the diamond particles are accumulated at the bottom of the strut (due to polygon shape of diamond-nickel particles and spherical shape of Ti6Al4V or 316 L, difference in weight/density/size, and sweeping by printer rubber). Another explanation is that diamond particles in the upper part of layer are destroyed (exploded) by intensive heating and only particles that are at the bottom of the layer are mostly surviving during heating by laser. Therefore, better bonding and homogeneous distribution of diamond particles are expected in a bulk print. This agrees with Fig. 8 where we show a surface of the 3D printed bulk/plain piece.

The 3D printed Ti6Al4V scaffold's surface could be treated by the alumina nanoparticle blasting. The results of the process are shown in Figs. 9 and 10 for different strut diameters (pore sizes). Then, post-cleaning or post-polishing has a pivotal role to avoid single inclusions weakly adhered to main cell structure that is especially important for bio applications with precisely defined pore or strut dimensions [34–36].

Diamond particle sizes, metal coating and fraction of Ti6Al4V have vital roles for full consolidation and to avoid the graphitization as much as SPS parameters (sintering time, temperature, pressure) allow. As

illustrated in XRD pattern in Fig. 11, graphite phase formation is inevitable and can alter to different final constituents; but choosing larger diamond particles with thicker nickel-coating yields better results [2,23]. According to previous findings stated above, the most suitable conditions/materials/processing were selected for current research.

Titanium Ti6Al4V argon atomized powder 5–40 μm (Fig. 12A) and stainless steel AISI 316 L 30–55 μm powder (Fig. 12B), manufactured by TLS Technik GmbH from Germany and Sandvik Osprey Ltd. from UK, respectively, and were used for the cellular lattice structures fabrication. For fabrication of matrices, the following powders were used: chromium metal powder in 6 μm particle size (Fig. 12C) and molybdenum in 1–3 μm particle size (Fig. 12D) both made by Pacific Particulate Material Ltd. Canada. Two types of polycrystalline 40–50 μm diamond particles with 30 and 56 wt% nickel coating (shown in Fig. 12E and F for 30% with 5.13 g/cm^3 density and 56% with 6.53 g/cm^3 density, respectively) were provided by Van Moppes & Sons Ltd. from Switzerland.

In Table 1 a list of equipment to fabricate the samples is given. To test the proposed fabrication technology six materials were manufactured. The details on the composition (in grams and wt%) is given in Table 2. Note that only samples No.5 and No.6 contain a 316 L lattice with 5 wt% diamond (15 mm height and 20 mm diameter, 1 mm lattice cell size), and the rest of them are lattice-free. Mixing Ti6Al4V (low-density titanium alloy), which has high strength and high corrosion resistance, with 316 L (high-density steel alloy), which has high ductility, produces a resistant composite that can be subjected to relatively high strain and an abrasive medium at high temperatures. In the current paper, 316 L-diamond FGL with circumferential to longitudinal 1:1 ratio of unit cell size in bottom, 1:2 in middle, and 1:3 for top is applied for samples No.5 and No.6. The tribological tests were carried out with

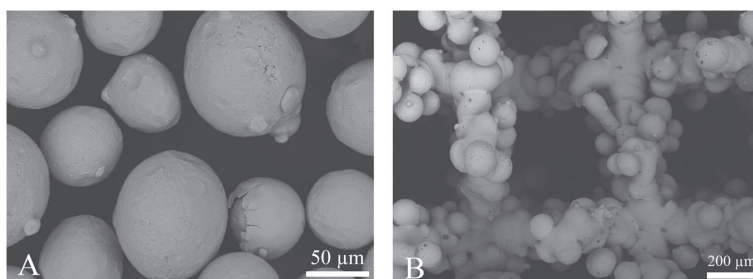


Fig. 5. Rockit 701 (Fe balance with 9.5 wt% W). A) Particles and B) 3D printed structure with unit cell size of 1 mm and smallest thickness of strut.

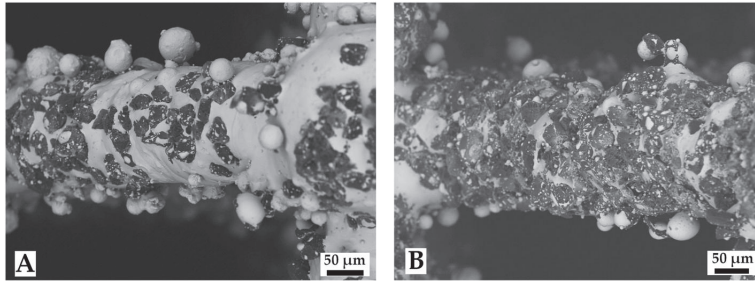


Fig. 6. 3D printed Ti6Al4V lattice structure with A) 5% and B) 10% diamond of volume content. The unit cell size is 1 mm and strut diameter 0.2 mm in both cases (top view).

1:1 cell size side.

Two steps of the SPS procedure included pre-heating/drying at 260 °C, 10 MPa, 6 min and sintering at 860 °C, 100 MPa, 6 min (see Fig. 13). Pre-heating (drying) step helps to dry the powders to avoid later surface oxidation of nickel coating and results in better bonding between the diamond particle and metals. The selected parameters of sintering were the maximum possible. The increase of the temperature and pressure in the sintering step above 860 °C and 100 MPa was leading to squeezing of melted metals (Ni, Cr, and Mo) out of the mold of the SPS machine.

The set parameters of the 3D metal printer were: laser current 3000 mA, exposure time 600 µs, and point distance of 1 µm. Note that the same printing parameters can be used to print both, 316 L and Ti6Al4V powders. Fig. 14A and B shows the difference between 316 L lattice and 316 L with 5% nickel-coated diamond particles. Diamond printing without considerable change to graphite phase is facilitated by pre-heating step, the close melting point of nickel and steel, and uniform distribution of diamond particles; whereas, excellent consolidation of the composite for the impact-abrasive application depends on SLM parameters (laser current, exposure time, point distance) and SPS parameters (pressure, temperature, time). Consolidated diamond particles in surrounded metal powders after SPS is shown in Fig. 15A and B with different magnifications for sample No.1. As well, embedded lattice structures of the sample No.5 is shown in Fig. 16.

The wear resistance evaluation of specimens to simulate excavation in mines and tunnels was performed on the innovative impact-abrasive tribological device (IATD), it is shown in Fig. 17A) developed at Tallinn University of Technology [37]. The impact loading was performed with the energy of impact 5.6 J and frequency of impact 28 Hz by Makita hammer drill. The WC-15% Co wheel with 100 mm diameter, 8 mm wide and 1 m/s sliding speed is pressed against specimen with 49 N force. Specimens after sintering were having the following dimensions: diameter - 20 mm and height - 10 mm (Fig. 17B). Abrasive sand grain

size 0.2–0.3 mm were flowing through a nozzle into the wear region (between the wheel and specimen surface) with 200 g/min rate. An optical surface profiler (OSP) was applied to characterize the results after 5 min (300 m sliding distance) of impacting and abrading with IATD.

3. Results and discussion

The results of the impact/abrasive test on the IATD are presented in Fig. 18 for the six samples from Table 2. The volumetric wear rates were measured three times and averaged. Significantly different results are obtained for each type of composite. It is demonstrated that samples No.3 (lattice-free) and No.6 (lattice-included) have superior wear resistance (both samples are visualized via OSP analyzer in Fig. 19). This can be attributed to the presence of Cr, Ni, Mo, Al, and V elements in the mix of 316 L and Ti6Al4V powders which even promotes the excellent mechanical properties. Additional Cr and Mo in samples No.2 made it more wear resistant than No.1 (Fig. 18). Another vital factor was a balance between the diamond percentage and that of bonding metals. It means that No.3 is more abrasion resistant than No.4 because of equilibrium between Cr-Mo-Ni and Diamond. For example, Cobalt alloy CoCr28Mo6 has higher hardness (HV10–385) and ductility than Ti6Al4V (HV10–370), 316 L (HV10–210) or nickel alloy IN939 (HV10–305) [8]. The idea of adding extra Cr–Mo to Ni has been raised to make the composite harder, more ductile and providing enough metal matrix for better performance of diamond particles.

316 L-5 wt% nickel-diamond SLM lattice can be adopted as an impact absorber structure that is sintered, filled in SPS along with other powders. No. 1–4 have 16 g weight and can be compared in pairs (pair one: No.1 and 2; pair two: No.3 and 4) due to almost equal amount of diamond. While, No.5 and 6 have 19 g weight and equal lattice structure. Nevertheless, it was not an unexpected outcome that sample No.6 wear resistance is better than No.5, because of a higher volume of

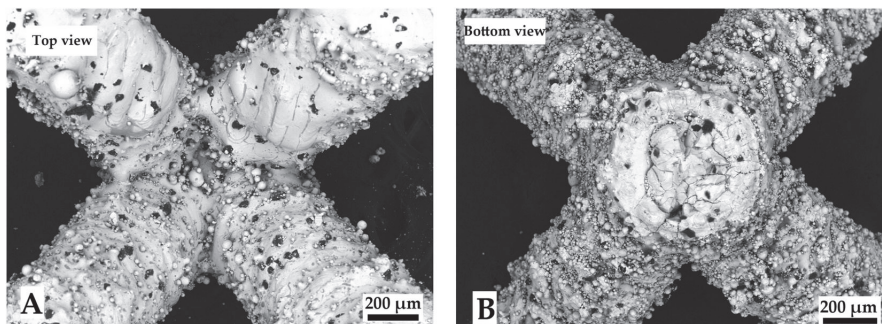


Fig. 7. 3D printed Ti6Al4V lattice structure with 5% diamond. A) Top and B) Bottom view. The unit cell size is 2 mm and the strut diameter is 0.5 mm.

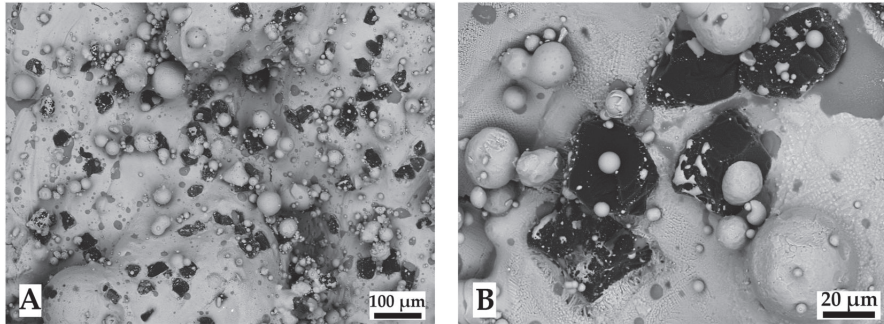


Fig. 8. 3D printed Ti6Al4V bulk volume with 5 wt% diamond. A) X500 and B) X1000 magnification. The specimen was 20 mm in diameter and 5 mm in height.

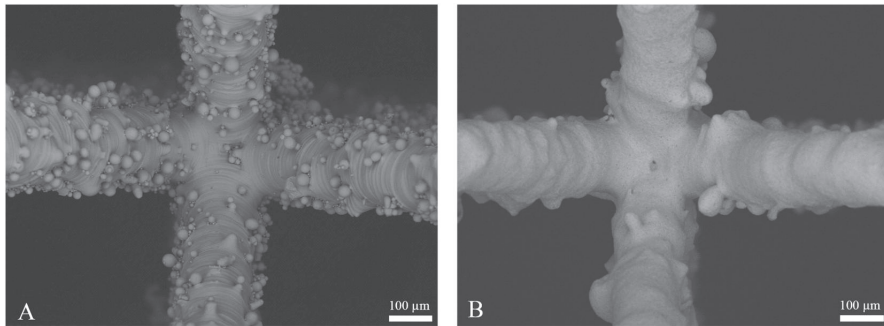


Fig. 9. Ti6Al4V lattice structures with 1.5 mm cell size and 0.2 mm strut diameter A) after printing and B) after alumina nanoparticle blasting.

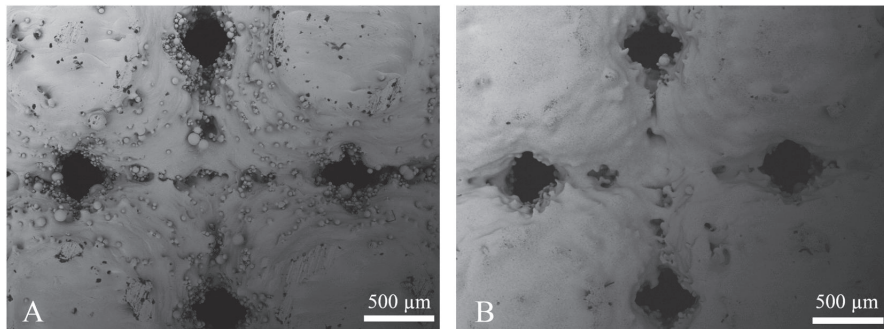


Fig. 10. Ti6Al4V lattice structures with 2.0 mm cell size and 1 mm strut diameter A) after printing and B) after alumina nanoparticle polishing.

diamond, a better balance between the value of Cr-Mo-Ni and proper bonding between melted lattice and sintered powders which is suitable for improving wear resistance, impact energy absorption and damage tolerance. Micrographs of samples after IATD is shown in Fig. 19. However, depth of wear scar in No.3 can be more in some points because of brittle fracturing but has lower volume of material lost during test. In equal test conditions, the wear scar of sample No.6 is more “flat” while wear of sample No.3 material is “cylindrical” (similar to the shape of the wheel of tribodevice). This is because of ductility of the lattice structure that was trapping diamond particles and removing them uniformly.

Fig. 20A demonstrates the distribution of diamond, titanium, iron, and nickel as EDS color mapping of sample No.3. The EDS elemental mapping results of 316 L, Ti6Al4V and diamond nickel-coating composition (without lattice) illustrated the presence of 12 elements,

namely, C 46.44%, Ti 23.31%, Fe 12.15%, Ni 9.65%, Cr 3.82%, Al 1.44%, V 1.11%, P 0.75%, Sn 0.52%, Mn 0.36%, Si 0.30%, and S 0.15% (Diamond with nickel coating usually contains small amount of phosphorus and chromium [38]). Also, the EDS elemental mapping results for Ti6Al4V and diamond nickel-coating composition embedded in 316 L lattice showed presence of 14 elements, namely, C 47.27%, Ti 23.57%, Fe 9.36%, Ni 8.40%, Al 3.36%, Cr 2.91%, Si 1.20%, V 1.04%, P 0.79%, W 0.60%, Na 0.43%, S 0.35%, Ca 0.34%, and Mn 0.30% (Fig. 20B).

In the current case, better weldability (or ability to be tightly fixed by bolts without brittle fracturing) at the bottom (more metal) and better abrasive behavior (more hard material) at the top is targeted for mining applications. Another advantage of using metallic cellular lattice was better electrical conductivity for materials during SPS process to gain more consolidated/densified composition with lower

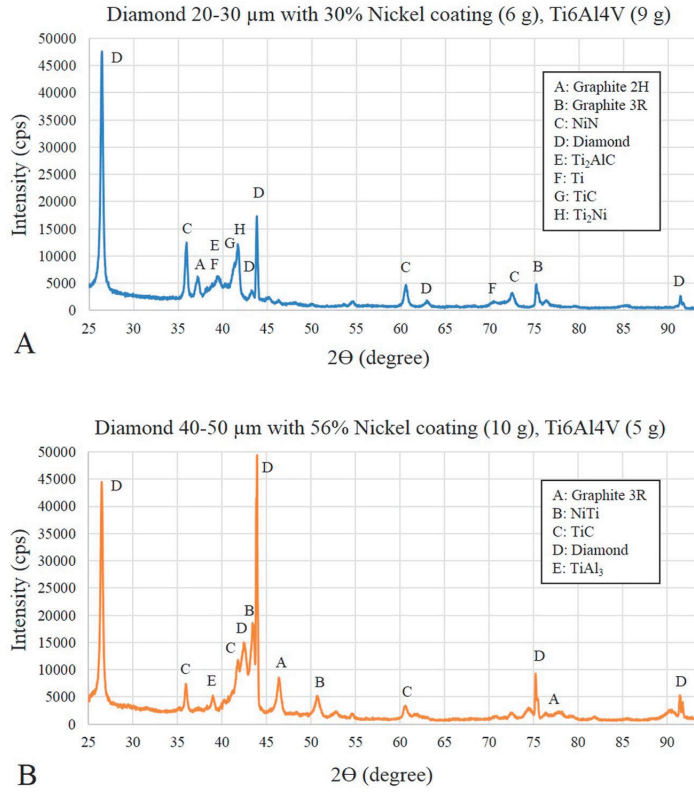


Fig. 11. XRD diffraction comparison of diamond-nickel-Ti6Al4V with different constituent volume. A) Diamond size 20–30 μm with 30% Nickel coating (6 g), Ti6Al4V (9 g), B) Diamond size 40–50 μm with 56% Nickel coating (10 g), Ti6Al4V (5 g).

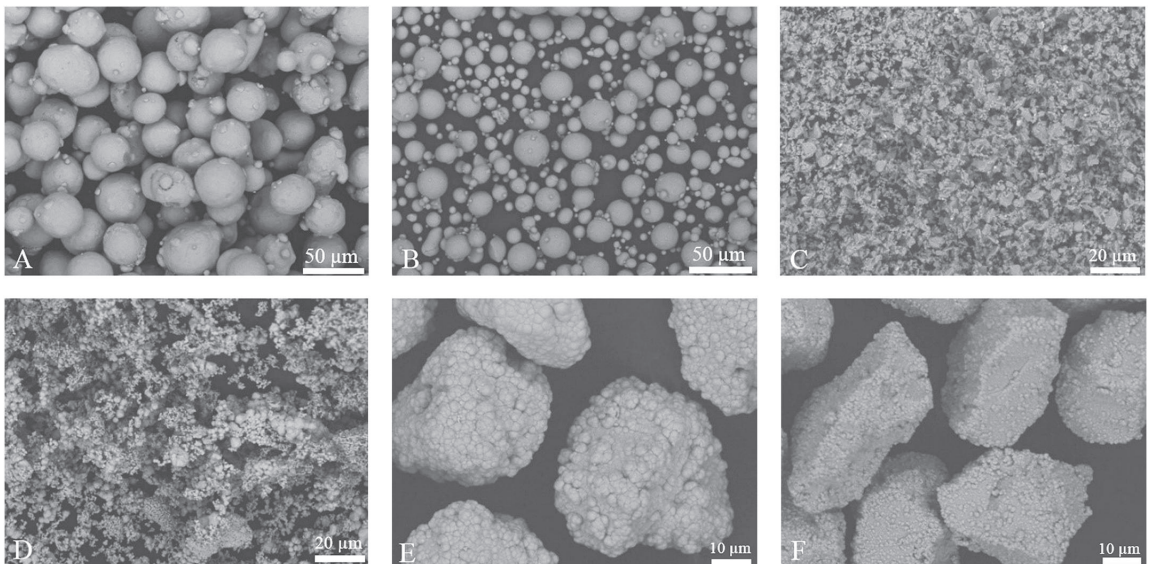


Fig. 12. SEM images of A) 316 L, B) Ti6Al4V, C) Chromium, D) Molybdenum, E) Diamond-56 wt% Ni, and F) Diamond-30 wt% Ni.

Table 1
Used machines list.

Process	Machine, specification
Selective Laser Melting (SLM)	Realizer SLM50, construction volume $\varnothing 70 \times 40$ mm, layer thickness 20–50 μm
Spark Plasma Sintering (SPS)	FCT System, up to 2200 °C and 100 MPa, 1000 °C/min heating rate
Impact-abrasive tribo-device (IATD)	Tribosystem, up to 19 J impact energy and up to 55 Hz impact frequency
Vacuum Nitriding Furnace (VNF)	R. D. WEBB, up to 1700 °C, nitrogen flow and 10 °C/min heating rate
Scanning Electron Microscopy (SEM)	Hitachi TM-1000, magnification 20–10,000 X
3D Optical Surface Profiler (OSP)	Bruker ContourGT-K0+, lost volume calculation from millimeter to nanometer range
Energy-dispersive Spectroscopy (EDS)	Zeiss EVO MA15 SEM with INCA Energy 350 X-ray micro-analyzer

Table 2

Description of samples content (in units of gram) - Lattice structures with 1 mm cell size are printed from 95 wt. % 316 L and 5 wt% of “Diamond-56 wt. % Ni”. Average particle sizes are: diamond 40–50 μm , Ti6Al4V 5–40 μm , 316 L 30–55 μm .

No.	Diamond (56 wt. % Ni)	Diamond (30 wt. % Ni)	Ti6Al4V	316 L	Chromium	Molybdenum	Lattice
1	8		4	4			
2	8		3.5	3.5	0.5	0.5	
3		6	5	5			
4		6	4.5	4.5	0.5	0.5	
5	8		3	3	0.5	0.5	4
6		6	4	4	0.5	0.5	4

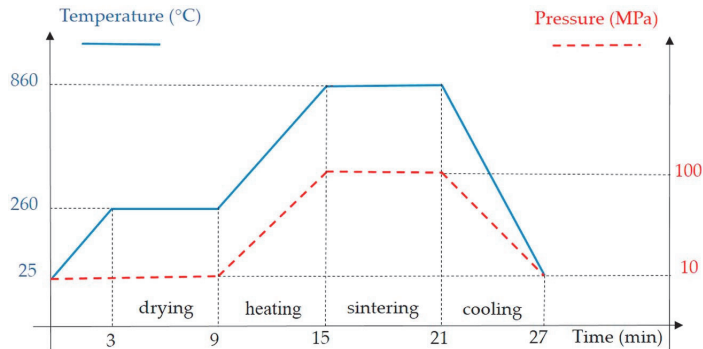


Fig. 13. SPS pressure-temperature sequence.

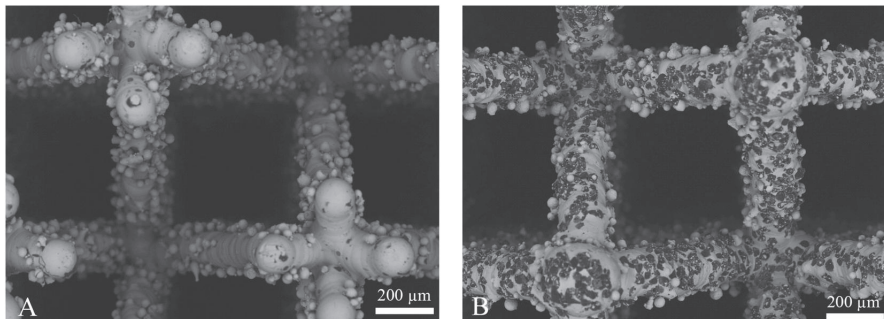


Fig. 14. SEM micrographs of A) 316 L and B) 316 L-5% diamond lattices (after 3D printing).

temperature and electric current. This method is advantageous to avoid material wasting in unnecessary surfaces/volumes and making higher performance cutters and blades by reduction the cost and time required for exchange operations. Depending on the volume fraction of the samples, three types of lattices were suggested in this paper: low, average and high as shown in Fig. 4. The low 12% volume fraction lattice structure (unit cell size 1.5 mm, Fig. 4A) did not lead to an expected increased wear resistance and noticeable damage tolerance. On

the other hand, the high 26% volume fraction lattice (unit cell size 0.75 mm, Fig. 4C) reduced the diamond content in the mixture, resulting in a decrease in hardness and wear resistance. The 19% volume fraction lattice (unit cell size 1 mm, Fig. 4B), combining 316 L and 5 wt % diamond mixed powder had the best properties.

The addition of chromium, molybdenum and nickel to the iron-based or titanium-based alloys improve corrosion, wear, chemical and heat resistance that is useful in medical and food industries [39,40].

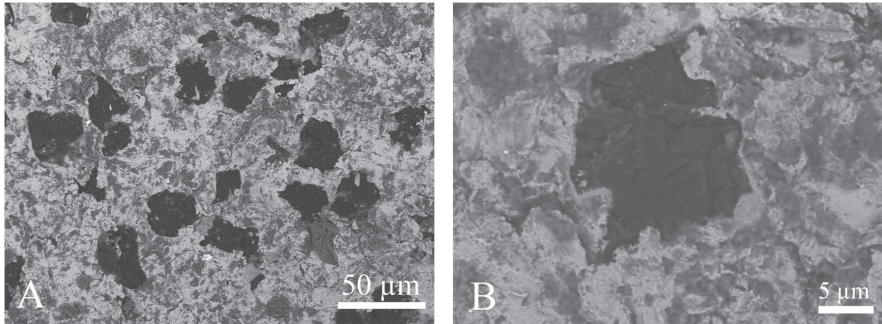


Fig. 15. SEM micrographs of sintered sample No.1 A) 500 ×, B) 2000 × (after SPSing).

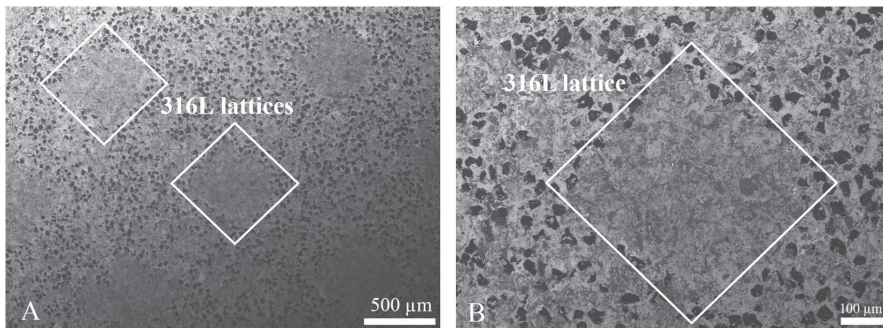


Fig. 16. SEM micrographs of sample No.5, lattice included (after SPSing).

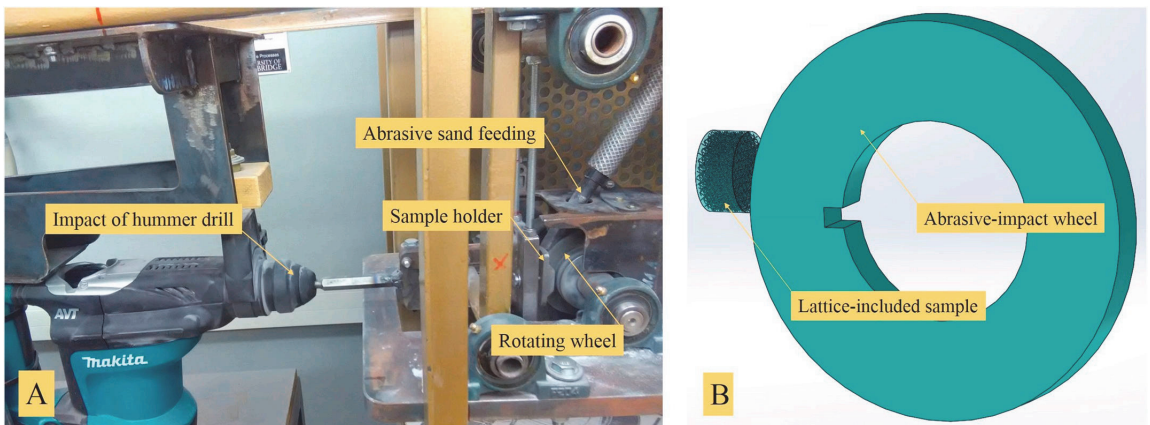


Fig. 17. A) Impact-abrasive tribology device (IATD) developed at Tallinn University of Technology, B) Lattice-included sample designed by SolidWorks.

However, nickel coating naturally has 8–12 wt% of phosphorus (producer company data [38]). As expected, sample No.2 is exhibited better wear resistance than No.1 (56% Ni coating for both samples No.1 and No.2), because increase of Cr–Mo, increases wear resistance. For the same reason, sample No.3 is evaluated higher impact-abrasive resistance than No.4 (30% Ni coating for both samples No.3 and No.4). Therefore, finding a balance point between diamond particles and bonding metals is necessary, because Cr–Mo–Ni increasing more than a critical value make it less resistant against impact and abrasion.

4. Simulation and application

To model the impact-abrasive conditions and to provide the tool for analysis and optimization of the relevant materials for these and other similar applications, the coupling of SolidWorks (CAD design) and Comsol (nonlinear dynamic analysis) was performed [24]. In the current simulation, the same dimensions were set up for both cylindrical samples ($\varnothing 20 \times 10$ mm) under single impact test without abrasive particles (Fig. 17). Mesh configuration is shown in Fig. 21. A finer mesh was chosen in the lattice structure as compared to the abrasive wheel. The numerical test was modeled in only one-stroke and in uniaxial

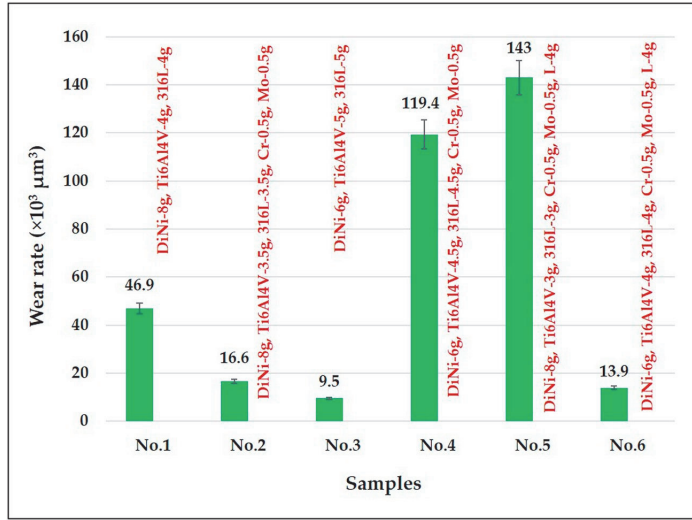


Fig. 18. Wear rate of samples during impact-abrasive test measured by 3D OSP (Di = diamond, Ni = nickel, Cr = chromium, Mo = molybdenum, and L = lattice).

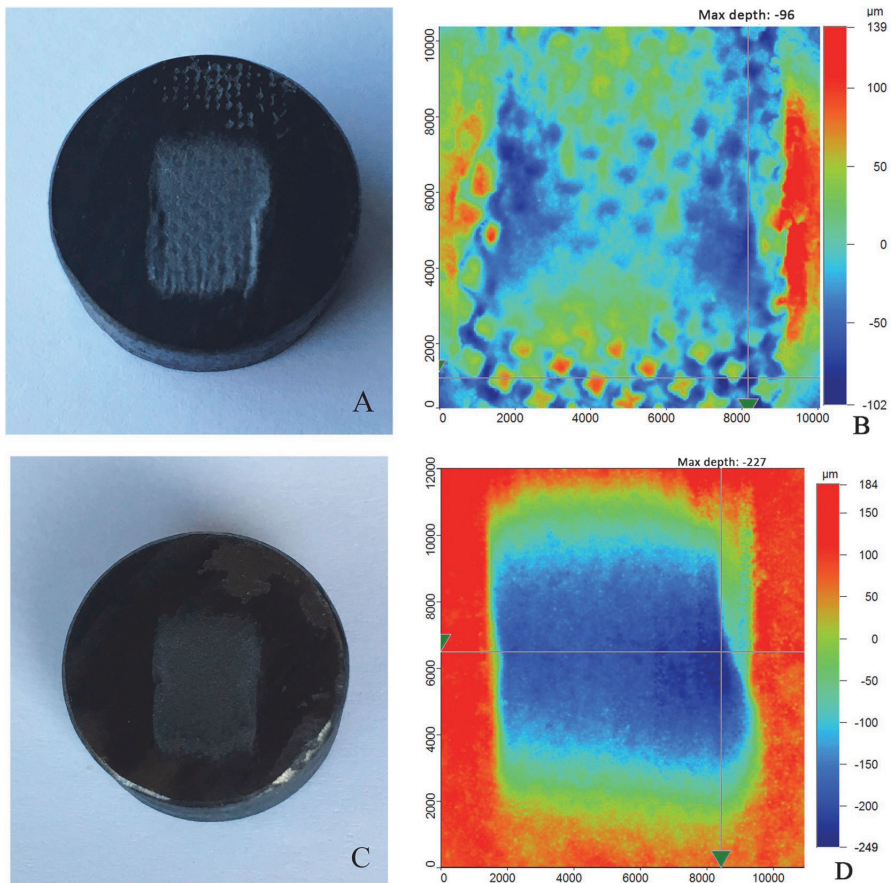


Fig. 19. Image of samples A) No.6 and C) No.3, OSP contour micrograph of samples B) No.6 and D) No.3 after impact-abrasive test (dimensions of lattice structures are 20 mm diameter and 9 mm height).

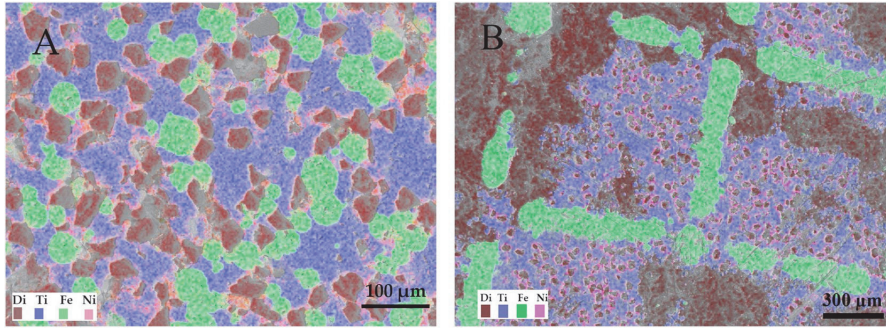


Fig. 20. EDS color mapping of A) 316 L, Ti6Al4V and diamond nickel-coating composition (without lattice) B) Ti6Al4V and diamond nickel-coating composition embedded in 316 L (with lattice).

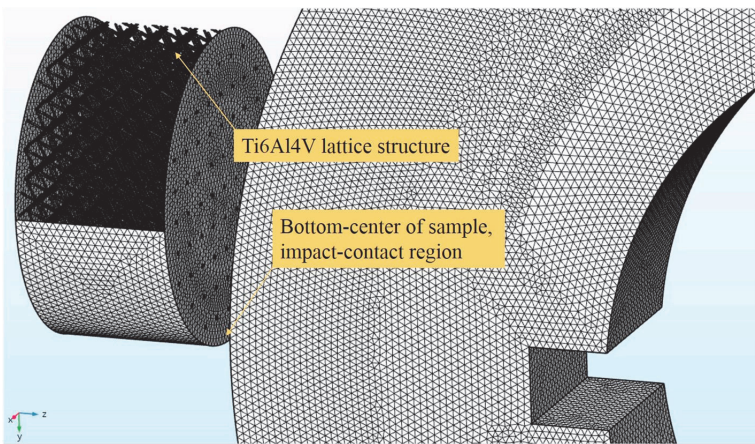


Fig. 21. Mesh configuration by Comsol based on tribo-device for impact test.

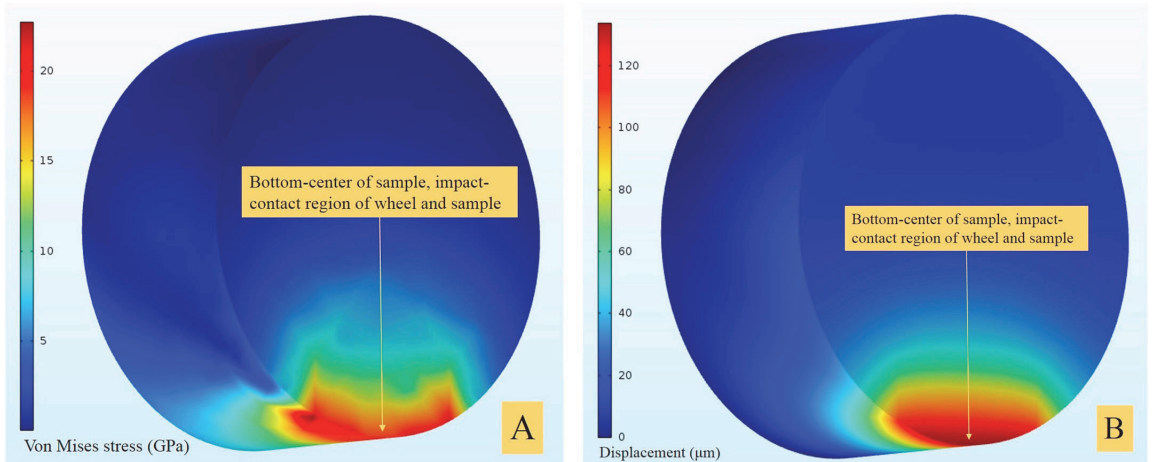


Fig. 22. Stress distribution and deformation of simple sample (pure diamond) after impact test (test 1).

direction with 5.6 J impact energy (non-rotating wheel, Ø 100 diameter). In the first simulation, a bulk specimen made from pure diamond was tested. The results for the Von Mises stress and displacement

is illustrated in Fig. 22. As expected, maximum values of stress and deformation are measured at the contact of the wheel and the sample. The simulation yielded maximum ≈ 23 GPa of stress and ≈ 135 μm

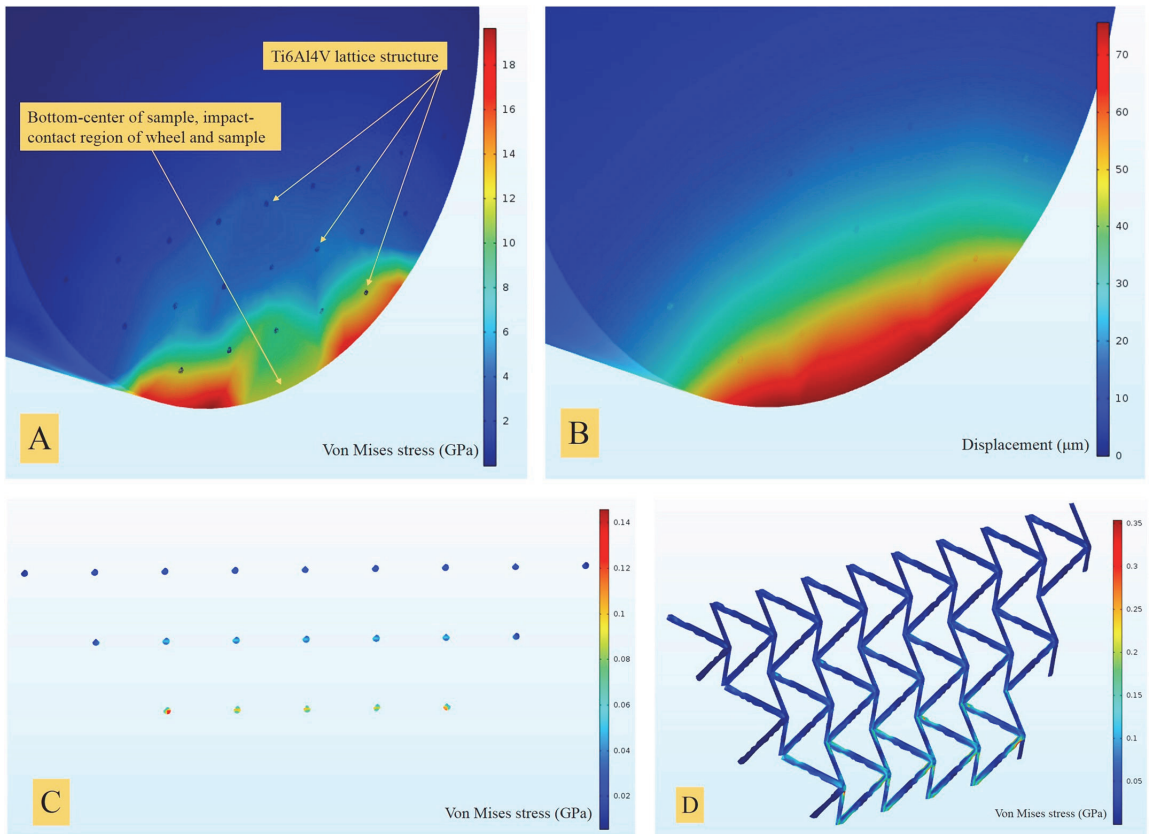


Fig. 23. Stress distribution and deformation of 316 L-lattice included (lattice beams have 0.2 mm diameter) diamond sample after impact test with impact influence on three bottom rows of lattice structure (test 2).

maximum displacement. The second test was modeled 2 mm unit cell size 316 L lattice structure throughout the sample (Fig. 23). The results (stress max. ≈ 19 GPa and displacement max. ≈ 75 μm) demonstrate impact absorption by 316 L lattices and significantly decrease in deformation of the sample. The presence of embedded lattice structure (uniform or gradient) prevents the increase of stress (Figs. 22A and 23A) and works as an impact absorber due to the lateral deformability of continuous metallic structure.

5. Conclusion

A new route has been introduced to fabricate parts with increased wear and impact resistance for the use in tunneling and mining applications. We used SPS method to consolidate metal-diamond composite having lattice structures manufactured by the SLM. The lattices can include diamond particles or other hard materials. Mixed 316 L-Ti6Al4V binder alloys and Cr-Mo-Ni transition metals made a strong additive composition for consolidation diamond particles in situ. 3D printing of functionally gradient lattice structures by SLM, nitriding, chromium coating, blasting by alumina jet, diamond mixing to 316 L particles in the SLM process of making lattices, and diamond mixing to Ti6Al4V in the SPS process of filling the lattice, were used in this paper. It was shown that adding 10 wt% coated diamond particles in the 316 L or Ti6Al4V powders results in slightly brittle scaffolds (in comparison to e.g. 5 wt% diamond) because of the weaker intersection and junction of struts due to less amount of binding metal. In addition, our tests show

that during solid/plain printing of Ti6Al4V-diamond mixture, the diamond particles are agglomerated at the bottom layers during 3D printing because of difference in shape, size and density. Our design by functionally gradient lattice in three stages enables better weldability/ductility at the bottom (where more metal is concentrated) and better hardness at the top (where more hard material can be located). Generally, positional definition of metal-diamond composition in desired location (continuous change from 100% metal to almost 100% hard reinforcement in uniaxial direction) in the FGL structure can be achieved with the proposed technology. Laboratory experiments of wear/impact on an impact-abrasive tribology device, developed in-house, were performed. The results show that the balance of nickel, molybdenum, and chromium in the content affects the performance of the fabricated specimens. Adding a higher content of Mo-Cr into Ni guarantees higher impact-abrasive resistance of the composite, along with the diamond particles coated by 30% Ni. A balance content between diamond powders and bonding metals (Cr, Mo and Ni) is important in both lattice-free and lattice-included structure types. We also performed finite element simulations which show that metallic-printed lattice structures enable more uniform distribution of stresses throughout the volume of the sample which implies that such structures have promising properties for applications e.g. in drilling/mining for their impact absorption abilities.

Different produced additive manufacturing powders (with spherical shapes) can be considered to mix with diamond or other hard materials (such as c-BN or WC-Co) as binder metal alloy powders include Ni-

based (Inconel625 or Inconel718), Co-based (CoCrMo or CoCrW), or Fe-based (high toughness 1.2709 or high tensile strength 1.4542). As current research has targeted the future of 3D printing on tunneling application with developed impact/abrasion test machine, it is desirable to investigate on geothermal earth drilling with emphasis on fatigue/rotating test machine and proper lattice structures. A circumferential FGL can be suggested with a metallic cylindrical core in the center and radially increased hard material from innermost to outermost diameter.

Declaration of Competing Interest

The authors (Ramin Rahmani, Miha Brojan, Maksim Antonov, and Konda Gokuldoss Prashanth) declare that there are no conflicts of interest regarding the publication of "Perspectives of metal-diamond composites additive manufacturing using SLM-SPS and other techniques for increased wear-impact resistance" in Journal of "International Journal of Refractory Metals & Hard Materials".

Acknowledgments

This research was supported by the Estonian Ministry of Higher Education and Research under Projects (IUT19-29 and ETAG18012), project number 2014-2020.4.01.16-0183 (Smart Industry Centre), Slovenian Research Agency (Program P2-0263), European Regional Funds through the project MOBERC15 and TTÜ base finance project (B56 and SS427). The authors would like to thank *Rainer Traksmaa* for the help with XRD patterning, *Heinar Vagiström* for the help with surface cleaning of samples via alumina nanoparticles and *Mart Viljus* for the help with EDS mapping.

References

- [1] Y. Holovenko, L. Kollo, M. Saarna, R. Rahmani, T. Soloviova, M. Antonov, K.G. Prashanth, S. Cygan, R. Veinthal, Effect of lattice surface treatment on performance of hardmetal-titanium interpenetrating phase composites, *Int. J. Refract. Met. Hard Mater.* 86 (2020) 105087.
- [2] R. Rahmani, M. Antonov, L. Kollo, Wear resistance of (diamond-Ni)-Ti6Al4V gradient materials prepared by combined selective laser melting and spark plasma sintering techniques, *Adv. Tribol.* (2019) 5415897.
- [3] <https://setis.ec.europa.eu/>.
- [4] www.hoganas.com/surface-coating.
- [5] Y. Holovenko, M. Antonov, L. Kollo, I. Hussainova, Friction studies of metal surfaces with various 3D printed patterns tested in dry sliding conditions, *Proce. Instit. Mech. Eng. Part J: J. Eng. Tribol.* 232 (2018) 43–53.
- [6] K.G. Prashanth, J. Eckert, Formation of metastable cellular microstructures in selective laser melted alloys, *J. Alloys Compd.* 707 (2017) 27–34.
- [7] E. Louvis, P. Fox, C.J. Sutcliffe, Selective laser melting of aluminium components, *J. Mater. Process. Technol.* 211 (2011) 275–284.
- [8] <https://www.slm-solutions.com/en/products/>.
- [9] A. Strondl, O. Lyckfeldt, H. Brodin, U. Ackelid, Characterization and control of powder properties for additive manufacturing, *springer, JOM* 67 (2015).
- [10] K.G. Prashanth, R. Damodaram, T. Maity, P. Wang, J. Eckert, Friction welding of selective laser melted Ti6Al4V parts, *Mater. Sci. Eng. A* 704 (2017) 66–71.
- [11] K.G. Prashanth, S. Kolla, J. Eckert, Additive manufacturing processes: selective laser melting, electron beam melting and binder jetting-selection guidelines, *Materials* 10 (2017) 672.
- [12] K. Dash, B.C. Ray, D. Chaira, Synthesis and characterization of copper-alumina metal matrix composite by conventional and spark plasma sintering, *J. Alloys Compd.* 516 (2012) 78–84.
- [13] V. Mamedov, Spark plasma sintering as advanced PM sintering method, *Powder Metall.* 45 (2002) 322–328.
- [14] <http://www.fct-systeme.de/en>.
- [15] A.B. Spierings, M. Voegtlin, T. Bauer, K. Wegener, Powder flowability characterization methodology for powder-bed based metal additive manufacturing, *Progr. Addit. Manufact.* (2016) 9–20.
- [16] H. Galarraga, R.J. Warren, D.A. Lados, R.R. Dehoff, M.M. Kirka, P. Nandwana, Effects of heat treatments on microstructure and properties of Ti-6Al-4V ELI alloy fabricated by electron beam melting (EBM), *Mater. Sci. Engin. A* 685 (2017) 417–428.
- [17] C. Yan, L. Hao, A. Hussein, D. Raymont, Evaluations of cellular lattice structures manufactured using selective laser melting, *Int J Mach Tool Manu* 62 (2012) 32–38.
- [18] J. Ping Li, J.R. de Wijn, C.A. Van Blitterswijk, K. de Groot, Porous Ti6Al4V scaffold directly fabricating by rapid prototyping: preparation and in vitro experiment, *Biomaterials* 27 (2006) 1223–1235.
- [19] Z.H. Liu, D.Q. Zhang, S.L. Sing, C.K. Chua, L.E. Loh, Interfacial characterization of SLM parts in multi-material processing: metallurgical diffusion between 316L stainless steel and C18400 copper alloy, *Mater. Charact.* 94 (2014) 116–125.
- [20] F. Velasco, W.M. Lima, N. Anton, J. Abenojar, J.M. Torralba, Effect of intermetallic particles on wear behaviour of stainless steel matrix composites, *Tribol. Int.* 36 (2003) 547–551.
- [21] A. Buford, T. Goswami, Review of wear mechanisms in hip implants: paper I-general, *Mater. Des.* 25 (2004) 385–393.
- [22] US9302945B2 United States Patent, 3-D Diamond Printing Using a Pre-Ceramic Polymer With A Nanoparticle Filler, <https://patents.google.com/patent/US9302945B2/en>.
- [23] R. Rahmani, M. Antonov, L. Kollo, Selective laser melting of diamond-containing or postnitrided materials intended for impact-abrasive conditions: experimental and analytical study, *Adv. Mater. Sci. Eng.* (2019) 4210762.
- [24] R. Rahmani, M. Antonov, N. Kamboj, Modelling of impact-abrasive wear of ceramic, metallic, and composite materials, *Proc. Est. Acad. Sci.* 68 (2019) 191–197.
- [25] R.M. Hooper, J.L. Henshall, A. Klopfer, The wear of polycrystalline diamond tools used in the cutting of metal matrix composites, *Int. J. Refract. Met. Hard Mater.* 17 (1999) 103–109.
- [26] J.P. Davim, Diamond tool performance in machining metal-matrix composites, *J. Mater. Process. Technol.* 128 (2002) 100–105.
- [27] E.A. Ekimov, N.V. Suetin, A.F. Popovich, V.G. Ralchenko, Thermal conductivity of diamond composites sintered under high pressures, *Diam. Relat. Mater.* 17 (2008) 838–843.
- [28] V.V.N. Reddy, B. Ramamoorthy, P.K. Nair, A study on the wear resistance of electroless Ni-P/diamond composite coatings, *Wear* 239 (2000) 111–116.
- [29] X. Wan, A. Hu, M. Li, C. Chang, D. Mao, Performances of CaSiO₃ ceramic sintered by spark plasma sintering, *Mater. Charact.* 59 (2008) 256–260.
- [30] N. Kamboj, M.A. Rodríguez, R. Rahmani, K.G. Prashanth, I. Hussainova, Bioceramic scaffolds by additive manufacturing for controlled delivery of the antibiotic vancomycin, *Proc. Est. Acad. Sci.* 68 (2019) 185–190.
- [31] R. Rahmani, M. Rosenberg, A. Ivask, L. Kollo, Comparison of mechanical and antibacterial properties of TiO₂/Ag ceramics and Ti6Al4V-TiO₂/Ag composite materials using combining SLM-SPS techniques, *Metals* 9 (2019) 874.
- [32] R. Rahmani, M. Antonov, Y.H. Kollo, K.G. Prashanth, Mechanical behavior of Ti6Al4V scaffolds filled with CaSiO₃ for implant applications, *Appl. Sci.* 9 (2019) 3844.
- [33] Y. Holovenko, L. Kollo, M. Jöeleht, R. Ivanova, T. Soloviova, R. Veinthal, Production of metal-ceramic lattice structures by selective laser melting and carburizing or nitriding, *Proc. Est. Acad. Sci.* 68 (2019) 131–139.
- [34] S. Van Bael, Y.C. Chai, S. Truscillo, M. Moesen, G. Kerckhofs, H. Van Oosterwyck, J.-P. Kruth, J. Schrooten, The effect of pore geometry on the in vitro biological behavior of human perosteum-derived cells seeded on selective laser-melted Ti6Al4V bone scaffolds, *Acta Biomater.* 8 (2012) 2824–2834.
- [35] S. Barui, S. Chatterjee, S. Mandal, A. Kumar, B. Basu, Microstructure and compression properties of 3D powder printed Ti-6Al-4V scaffolds with designed porosity: experimental and computational analysis, *Mater. Sci. Eng. C* 70 (2017) 812–823.
- [36] J.M. Sobral, S.G. Caridade, R.A. Sousa, J.F. Mano, R.L. Reis, Three-dimensional plotted scaffolds with controlled pore size gradients effect of scaffold geometry on mechanical performance and cell seeding efficiency, *Acta Biomater.* 7 (2011) 1009–1018.
- [37] M. Antonov, R. Veinthal, D.-L. Yung, D. Katusin, I. Hussainova, Mapping of impact-abrasive wear performance of WC-co cemented carbides, *Wear* 332–333 (2015) 971–978.
- [38] <http://www.vanmoppes.ch/en/>.
- [39] B.F. Shahgaldi, F.W. Heatley, A. Dewar, B. Corrin, In vivo corrosion of cobalt-chromium and titanium wear particles, *J. Bone Joint Surg.* 77 (1995).
- [40] E. Zumelzu, I. Goyos, C. Cabezas, O. Opitz, A. Parada, Wear and corrosion behaviour of high-chromium (14-30% Cr) cast iron alloys, *J. Mater. Process. Technol.* 128 (2002) 250–255.

Publication II

R. Rahmani; M. Rosenberg; A. Ivask; L. Kollo; Comparison of mechanical and antibacterial properties of TiO₂/Ag ceramics and Ti6Al4V-TiO₂/Ag composite materials using combining SLM-SPS techniques, *Metals* 9 (2019) 1-13.

Article

Comparison of Mechanical and Antibacterial Properties of TiO₂/Ag Ceramics and Ti6Al4V-TiO₂/Ag Composite Materials Using Combined SLM-SPS Techniques

Ramin Rahmani ^{1,*}, Merilin Rosenberg ^{2,3}, Angela Ivask ³ and Lauri Kollo ¹

¹ Department of Mechanical and Industrial Engineering, Tallinn University of Technology, Ehitajate Tee 5, 19086 Tallinn, Estonia

² Department of Chemistry and Biotechnology, Tallinn University of Technology, Ehitajate Tee 5, 19086 Tallinn, Estonia

³ Laboratory of Environmental Toxicology, National Institute of Chemical Physics and Biophysics, Akadeemia Tee 23, 12618 Tallinn, Estonia

* Correspondence: ramin.rahmaniahranjani@ttu.ee; Tel.: +372-5198-8504

Received: 16 July 2019; Accepted: 7 August 2019; Published: 8 August 2019



Abstract: In present work, the combination of spark plasma sintering (SPS) and selective laser melting (SLM) techniques was introduced to produce composite materials where silver-doped titania (TiO₂) ceramics were reinforced with ordered lattice structures of titanium alloy Ti6Al4V. The objective was to create bulk materials with an ordered hierarchical design that were expected to exhibit improved mechanical properties along with an antibacterial effect. The prepared composite materials were evaluated for structural integrity and mechanical properties as well as for antibacterial activity towards *Escherichia coli*. The developed titanium–silver/titania hybrids showed increased damage tolerance and ultimate strength when compared to ceramics without metal reinforcement. However, compared with titania/silver ceramics alone that exhibited significant antibacterial effect, titanium-reinforced ceramics showed significantly reduced antibacterial effect. Thus, to obtain antibacterial materials with increased strength, the composition of metal should either be modified, or covered with antibacterial ceramics. Our results indicated that the used method is a feasible route for adding ceramic reinforcement to 3D printed metal alloys.

Keywords: Ti6Al4V lattice structure; Ag-doped TiO₂ anatase; spark plasma sintering; selective laser melting; additive manufacturing; antibacterial and photoactivity applications

1. Introduction

Titania (TiO₂) is one of the very often used ceramic materials in medical, antibacterial, paint, varnish, and pigment applications. Two well-known mineral forms of TiO₂ are anatase and rutile that have motivated interests in electrical conductivity and photocatalytic activity fields. Anatase TiO₂ has been shown to exhibit photocatalytic and thus, self-cleaning, activity under ultraviolet illumination. Photodegradation capability of TiO₂, especially under visible light conditions can be even further enhanced by depositing transition metal dopants like silver (Ag) [1,2]. For enhanced antibacterial effect of those materials, Ti-implants have been coated by TiO₂-nanotubes and Ag-nanoparticles in dental and orthopedic applications [3]. The primary interest in TiO₂ ceramics has been related to its use in thin films or as an additive [4]. The implementation of TiO₂ as a bulk ceramic is mainly restricted due to its high brittleness, having fracture toughness in the order of 2–3 MPa·m^{1/2} [5].

It is possible to reinforce ceramic materials with metals, to improve the mechanical properties of the ceramics. Titanium and its alloys are widely used as biomaterials due to their sufficient biocompatibility, light weight, and high mechanical strength [6]. Titanium has excellent physical properties, its corrosion resistance is utterly known for orthopedic, osteology, and dental applications [7] and it possesses the ability to be 3D printed into complex objects. Research studies have displayed that the powder of Ti6Al4V, a material that is finding increasing use in medical applications has a high potential as a starting material for selective laser melting (SLM), a method that can be used to create various 3D structures [8]. Titania that requires relatively low temperatures for full consolidation, may be successfully combined with 3D printed metals. Combining oxide ceramics with metals by common methods is however complicated due to the inherent incompatibility of the interphases. For example, fusing of wear resistant oxide ceramics on a titanium substrate for implants faces distinct challenges in terms of obtaining strong bonding between the ceramic and the metal [9].

Different methods can be applied for consolidating ceramics and composites based on these. When ultrafine- or nano-structures are desired, spark plasma sintering (SPS) is commonly used. Both nanostructured titania and titania based nanocomposites have been produced by SPS [10–12]. Due to very high heating and cooling rate that can preserve the nanostructure at nearly full density, silver-doped titania could be employed for medical applications where antimicrobial properties, chemical inertness, and wear resistance are needed and also for water purification. Combining with titanium could drastically increase the damage tolerance of the ceramic and also provide added application specific functions. For example, a device of combined TiO₂/Ag and Cu/CoNiP was shown to effectively perform as magnetically rolling microrobots for water purification [13].

In this study a combination of selective laser melting and spark plasma sintering was introduced for the production of new versatile metal–ceramic hybrid structures to increase damage tolerance of the material. In the process, SLM was used to first 3D print the periodic titanium lattice structure followed by the embedding of titania–silver composite powder to the lattice and hot consolidation by SPS. Prepared materials were analyzed for mechanical properties under a compression test and antibacterial activity against *Escherichia coli* cells.

2. Materials and Methods

2.1. Materials

Titanium dioxide powders with BET surface area of 150 m²/g (Figure 1a) and flaky silver powder with the purity of 99.95% (Figure 1b) were purchased from ABCR GmbH and used to produce ceramic materials and as the matrix phase in composites. Titanium dioxide was first ultrasonically deagglomerated under isopropanol. Doping with 2.5wt% of silver was performed by using a bottle mixer at 15 RPM for 24 h. Yttria (Y₂O₃) stabilized polycrystalline zirconia (ZrO₂) was manufactured in TOSOH corporation (TZ-3Y-E, Tokyo, Japan) and was used to produce control ceramic surfaces for antibacterial tests (Figure 1c). Gas atomized Ti6Al4V alloy powders having a particle size in the range from 15 to 45 μm (Figure 1d) were obtained from TLS Technik Spezialpulver GmbH and were used to print metal lattices.

2.2. Specimens Preparation

Ceramic materials of TiO₂–2.5% Ag, pure TiO₂ and ZrO₂ (the latter two as controls for the antibacterial test) were produced using a spark plasma sintering (SPS) machine HP D10 from FCT GmbH. Sintering temperature of 750 °C, pressure of 75 MPa and holding time of 30 min were used to compact the composites. To produce metal–ceramic composite materials, first cylindrically shaped Ti6Al4V lattices (Figure 2, top row) were produced using selective laser melting (SLM50 metal additive manufacturing system from Realizer GmbH). The specimens had a diameter of 20 mm and height of 15 mm. The specimens exhibited diamond type porous lattices with unit cell size from 1 to 2 mm. To prepare metal–ceramic composites, porous titanium lattice was placed in a graphite mold and

ceramic powder of TiO_2 supplemented with 2.5% Ag was embedded in the lattices (Figure 2, bottom row). SPS at $900\text{ }^\circ\text{C}$, 75 MPa and during 30 min was used to compact the composites (Figure 3). The height of compacted composite lattices was 3–4 mm and depended on the cell size of initial lattices. Lattices with 1 mm cell size were shrunk down to 4 mm, lattices with 1.5 mm cell size shrunk to 3.5 mm and lattices with 2 mm cell unit size shrunk to 3 mm. For the compressive test, identical SPS conditions were applied for 10 mm diameter and 25 mm height lattice structures.

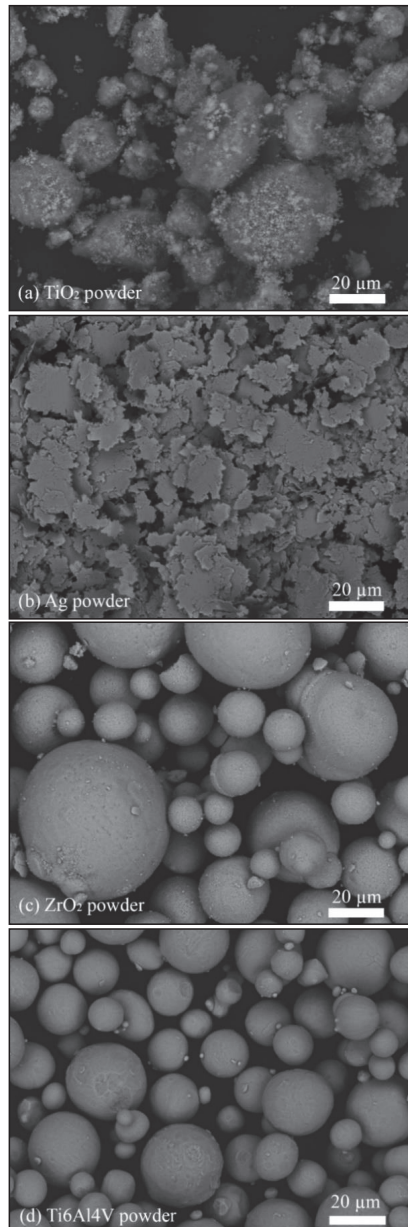


Figure 1. SEM micrographs of (a) TiO_2 anatase, (b) Ag, (c) ZrO_2 , and (d) Ti6Al4V powders.

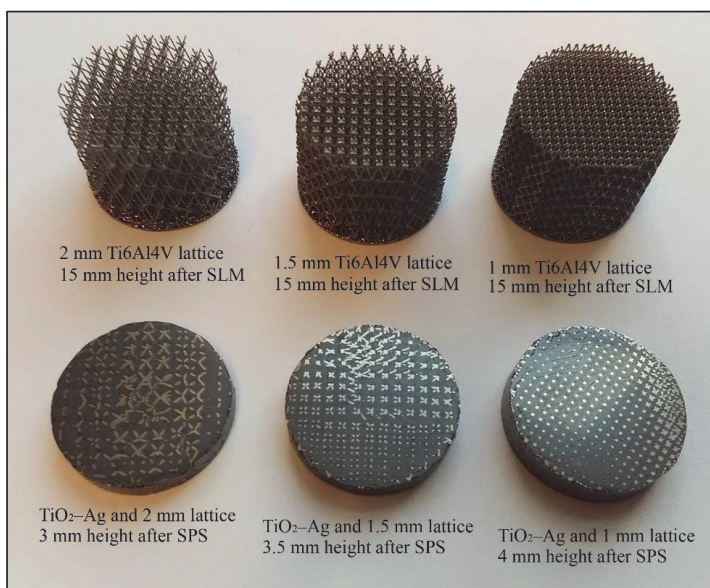


Figure 2. **Top row:** Selective laser melting (SLM) manufactured Ti6Al4V lattice structures with unit cell size and volume fraction of 2 mm and 6%, 1.5 mm and 9%, 1 mm and 16%, respectively (dimensions of lattice structures are 20 mm diameter and 15 mm height); **Bottom row:** Spark plasma sintering (SPS) sintered TiO₂-2.5% Ag embedded in the Ti6Al4V lattice structures.

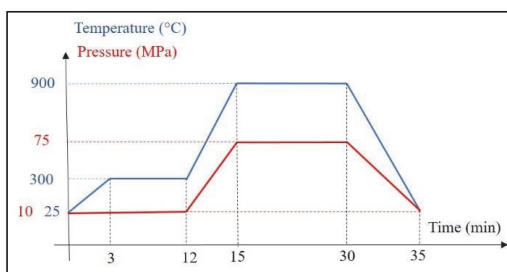


Figure 3. SPS conditions for TiO₂ powder embedded Ti6Al4V lattice structure.

2.3. Mechanical and Microstructural Characterization

Microstructure of the produced materials was examined with a scanning electron microscope (Zeiss EVO MA15, Oberkochen, Germany) equipped with energy dispersive spectroscopy (EDS). Compressive testing of the samples was performed on Instron 8516 servo-hydraulic test machine. The cylindrical samples with diameter of 10 mm and height of 8–9 mm (the height of 3D printed lattice structures was 25 mm which was shrunken to 8–9 mm after SPS) were loaded with a crosshead speed of 0.5 mm/min, according to standard ASTM E9/09.

2.4. Antibacterial Assay

A comparative antibacterial assay was carried out for TiO₂-2.5% Ag, TiO₂, and ZrO₂ ceramics as well as for TiO₂-2.5% Ag and Ti6Al4V lattice hybrid structures of 1, 1.5, and 2 mm cell sizes (Figure 2). The assay was carried out using an in-house protocol based on ISO 27447:2009 and ISO 22196:2007 standard methods [14] towards a model gram-negative bacterium *Escherichia coli* MG1655. Prior to all experiments, the specimens were sanded and polished, in order to remove potential contaminants and smoothen the surface, then sterilized by autoclaving at 121 °C for 15 min. The material samples were

reused for consecutive experiments. After each test, samples were thoroughly washed with water and 70% ethanol, drained, submerged in 80 mL deionized water and sonicated using Branson Digital Sonifier model 450 (max power 400 W) equipped with horn model 101-135-066R at 25% amplitude for 10 min before autoclaving. *E. coli* culture for inoculum suspension was collected from fresh nutrient agar (5 g/L meat extract, 10 g/L peptone, 5 g/L sodium chloride, 15 g/L agar powder in deionized water) plates incubated overnight at 30 °C, suspended in 500-fold diluted nutrient broth (3 g/L meat extract, 10 g/L peptone, 5 g/L sodium chloride in deionized water) and further diluted with the same medium to optical density of 0.01 at 600 nm. Sterile surface samples were placed on the bottom of sterile 6-well polystyrene plates, inoculated with 50 µL *Escherichia coli* MG1655 suspension and covered with 2 cm × 2 cm × 0.005 cm polyethylene film. Exposure medium was 1:500 diluted nutrient broth. Samples were in parallel either covered by 1.1 mm UVA-transmissive borosilicate glass sheet and exposed to 2–2.5 W/m² UVA at 315–400 nm spectral range (measured using Delta Ohm UVA probe) effective at the sample level or kept in the dark covered by a 6-well plate lid.

After 30 min and 4 h exposure bacteria were retrieved from samples by repeatedly pipetting 3 mL of neutralizing medium (soybean-casein digest broth with lecithin and polyoxyethylene sorbitan monooleate: 17 g/L casein peptone, 3 g/L soybean peptone, 5 g/L sodium chloride, 2.5 g/L disodium hydrogen phosphate, 2.5 g/L glucose, 1.0 g/L lecithin, 7 g/L nonionic surfactant in deionized water) over the surface, serially diluted in 2 mL volume of physiological saline and from each dilution 3 × 20 µL drop-plated on nutrient agar. Plates were incubated overnight at 30 °C after which colony forming units were counted. The experiment was repeated at least three times for each surface type and time point. Statistical analysis of test results were carried out in GraphPad Prism 7.04 software using one-way ANOVA analysis with Tukey's multiple comparisons test at 0.05 significance level. Due to highly variable and inconsistent results of lattice-embedded samples, these were excluded from statistical analysis at the 4 h time point.

3. Results

3.1. Structural Study and Mechanical Properties of the Composite Materials and Ceramics

The appearance of TiO₂ and TiO₂-2.5% Ag ceramic surfaces, and TiO₂-2.5% Ag in Ti6Al4V composite materials is shown in Figure 4. The white color of TiO₂ ceramic changed to gray when 2.5% Ag was added. However, lighter areas likely with lower Ag content can be seen in TiO₂-2.5% Ag ceramic (Figure 4). Under SEM (Figure 5) adequate interphase cohesion with some porosity between ceramic and Ti6Al4V lattice rods was observed. A SEM image (Figure 5a) and digital photograph (Figure 2) show that the 1 mm lattice structure was less bent or distorted subjected to SPS conditions. Critical areas were the interphases between the lattice and ceramic. Although water tightness of the hybrids was achieved, still some porosity at the interphase remained (Figure 5b).

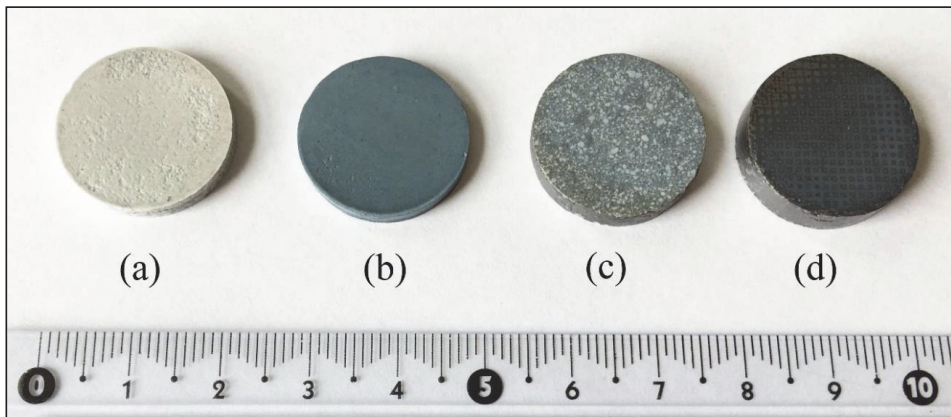


Figure 4. Digital photograph of (a) ZrO_2 , (b) pure TiO_2 anatase, (c) TiO_2 -2.5% Ag, (d) composite structure with TiO_2 -2.5% Ag and Ti6Al4V lattice after sintering (the lattice unit cell size is 1 mm and diameter of samples are 20 mm).

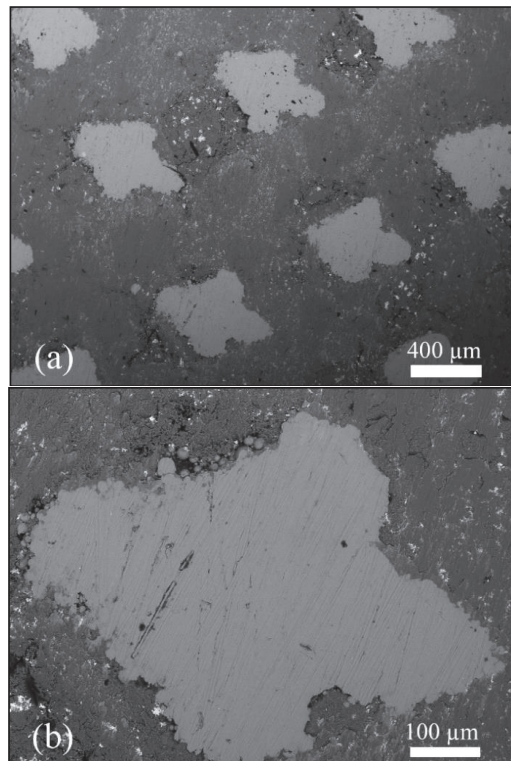


Figure 5. SEM micrograph of TiO_2 -2.5% Ag and Ti6Al4V lattice structure (1 mm unit cell size) taken at $\times 50$ magnification (a) and $\times 200$ magnification (b).

The EDS elemental mapping results (Figure 6) showed presence of seven elements, namely, Ti 56.45%, O 39.36%, Ag 2.53%, V 0.56%, Al 0.48%, Cl 0.42%, and P 0.20%. The EDS spectrum illustrated acceptable distribution of TiO_2 and Ag in composition. Also, rounded Ti6Al4V rods cross-section validated the resistance of 1 mm cell size printed lattice under compression (Figures 2 and 6). To reveal

the damage tolerance characteristics of ceramic–metal composite materials compared to pure ceramics, compression tests were performed (Figure 7). When plain titania ceramic showed brittle fracture, then lattice composite specimens did not catastrophically fail until 25% of deformation. For samples with larger volume fractions of metal phase (1 and 1.5 mm unit cell sizes) in addition to the absence of critical failure, ultimate strength of the composites was significantly higher.

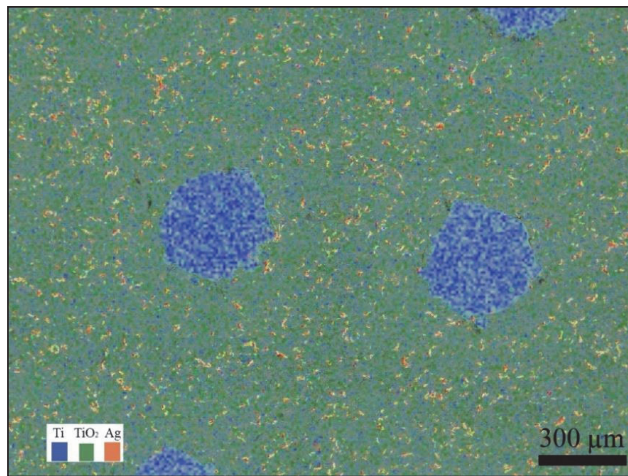


Figure 6. Energy dispersive spectroscopy (EDS) color mapping of TiO_2 -2.5% Ag embedded 1 mm cell size Ti6Al4V lattice structure.

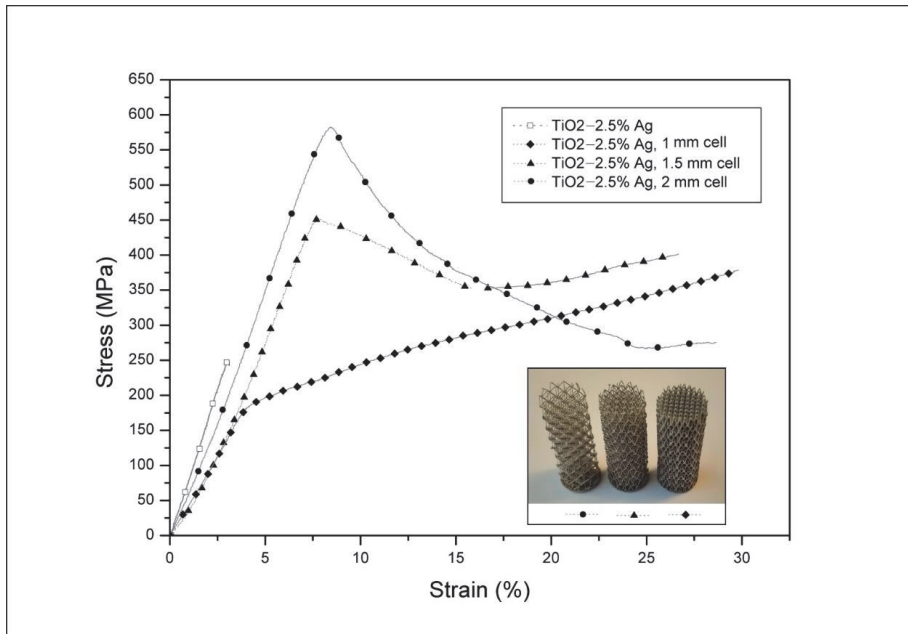


Figure 7. Compressive test results for TiO_2 -Ag without and with different unit cell sizes of lattice structure. Height of lattices were 25 mm and diameter was 10 mm before SPS.

3.2. Antibacterial Activity of the Surfaces

Antibacterial activity of the composite and ceramic materials towards *E. coli* MG1655 was evaluated after 30 min and 4 h exposure (Figure 8) while using ceramic zirconia surface as a negative control. Among the tested materials, the highest antibacterial effect in dark conditions was observed for TiO₂-2.5% Ag ceramics where >3 logs reduction in *E. coli* viability was observed already within 30 min compared to control ($p < 0.01$) and no viable bacteria detected at the detection limit of about 450 colony forming units (CFU) per surface. As ceramic TiO₂ without added silver had no antibacterial effect in dark conditions ($p > 0.05$), we suggest that the effect seen for Ag-supplemented TiO₂ ceramics was due to Ag ions released from the material. Results for lattice-embedded TiO₂-2.5% Ag surfaces were not statistically different from control after 30 min ($p > 0.05$) and had too high variability to compare results with full ceramic materials after the 4 h time point. The fact that significantly less antibacterial effect was seen for lattice-embedded samples suggests that the release of Ag from those materials was much lower than from ceramic samples.

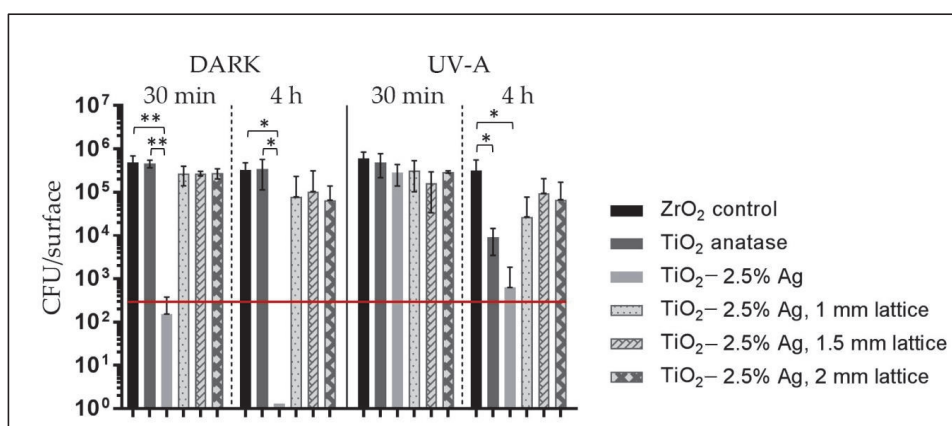


Figure 8. Viability of *Escherichia coli* MG1655 on ceramic and composite hybrid surfaces after 30 min and 4 h exposure in the dark and UV-A-illumination. Columns represent recovered viable bacteria as colony forming units (CFU). Mean and standard deviation of at least three independent values is shown on a logarithmic scale and only statistically significant differences ($p < 0.05$) marked on the graph (* $p < 0.05$ and ** $p < 0.01$). Only the upper error bar is shown for samples with >100% SD. Lattice samples are excluded from statistical analysis at 4 h time points due to very high variability. Limit of detection at 458 CFU/surface marked in red.

Due to the photocatalytic nature of TiO₂, the samples were assumed to exhibit UV-induced antibacterial effects. Indeed, 4 h exposure of bacteria to the ceramic TiO₂ surface under UV-A decreased bacterial viability by 1.6 logs ($p < 0.05$) compared to the control surface. The efficacy of Ag-supplemented ceramic TiO₂ surface under UV-A was higher than that of ceramic TiO₂ surface but significantly lower than the efficacy of TiO₂-2.5% Ag surface in dark conditions. This is likely because UV exposure has been shown to significantly decrease Ag solubility and subsequently, antibacterial activity as has been previously shown for photo-inducible Ag complemented ZnO surfaces [14].

Metal reinforced TiO₂-2.5% Ag ceramics showed significantly lower antibacterial effect than what was seen for ceramic surfaces. After 30 min under UV-A, TiO₂-2.5% Ag composite surfaces did not exhibit significant antibacterial effects compared with ZrO₂ control. After 4 h UV-A exposure, the composite surfaces yielded results that had too high variability to statistically compare them with control surfaces or full ceramic materials. However, according to the general picture, the composite surfaces exhibited slight antibacterial effect as compared to ZrO₂ control. These results showed that

while including titanium lattice to TiO_2 -2.5% Ag ceramic material increased the damage tolerance of the material, it significantly decreased the antibacterial effect of the ceramic material.

4. Discussion

Bonding of brittle ceramics to structural metals in assemblies has often remained a challenge, requiring designing for bolting or specific soldering alloys. The results described in this work represent a new approach for bonding, using additively manufactured lattice structure in the interphase of metal and ceramic. The composite structure where TiO_2 -2.5% Ag was bonded with titanium showed not only increased damage tolerance but also increased ultimate compressive strength when compared to unreinforced ceramics. To explain the increased strength and damage tolerance, ceramic and metal-ceramic samples were subjected to a compressive test (Figure 7). The results showed large fractured pieces in the case of ceramics (Figure 9a), whereas ceramics in the composite sample was fractured into sub-micrometric particles (Figure 9b). For highly brittle material such as TiO_2 -Ag, a larger content of energy is absorbed in crack initiation for hybrid composites.

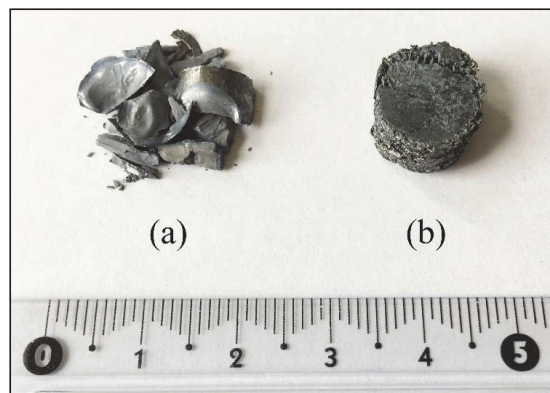


Figure 9. Appearance of (a) TiO_2 , (b) composite structure with TiO_2 - Ti6Al4V hybrid after compressive testing (sample diameter was 10 mm and unit cell size was 1 mm).

The proposed failure mechanism of composite hybrids is visualized in Figure 10. Three modes of deformation could be distinguished. During the first mode, at applied strain up to 2–3 percent, energy was absorbed in rearrangement and elastic deformation of the metallic lattice. The elastic modulus of the composite hybrid (≈ 50 – 80 GPa) was significantly lower than the elastic modulus of both separated constituents, Ti6Al4V (≈ 110 – 120 GPa) and TiO_2 (≈ 230 – 280 GPa). In the middle region of the elastic part of the compressive loading curve a cracking sound was observed. This was due to the removal of fractures of ceramic elements exposed to the surface (schematically shown in Figure 10, Mode 2). Until the yielding point, surface exposed ceramic elements were gradually removed, and this remained as the main deformation mechanism during plastic deformation of the hybrid, during Mode 3. Additionally, the interior ceramic elements were fractured as shown in Figure 10, Mode 3. The opposing force from metallic lattice (indicated by black arrows in Figure 10) induced back-pressure and fractured ceramic pieces got embedded into a ductile metal lattice. This interaction increased the damage tolerance of the composite hybrid under compressive loading.

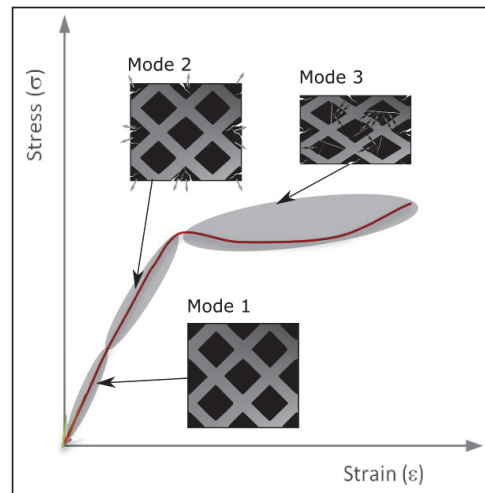


Figure 10. Schematic showing fracture mechanisms of metal–ceramic hybrids under compressive loading. Mode 1: rearrangement and elastic deformation of metal lattice; Mode 2: fracturing of ceramic surface elements; Mode 3: fracturing of the interior ceramic elements and embedding of these in ductile metal lattice.

Consequently, three modes of failure of the hybrid composite were differentiated during compressive loading. The increased damage tolerance and compressive strength were attributed to higher input energy needed to fracture the ceramics and interaction between fractured ceramic pieces and ductile metal lattice inside the material. As it was seen on the hybrid specimens after compressive testing (Figure 9b), the ceramic material was removed preferentially at the perimeter of the cylindrical sample. Further strengthening could be achieved if hybrid composite would be surrounded by an additional metallic layer so that ceramic would not be exposed on the outer surface.

Metal 3D printing enables the production of lattice structure objects with different shapes and internal mesostructures. The composite, therefore, can be designed according to existing mechanical loads. Functionally grading in different directions, and integrating solid printed metals with ceramic–metal hybrids could be realized. Furthermore, a metal lattice could be designed so that it acts as a heating element when an electric current is directed through the material. The heating would further enhance the antimicrobial effect of the ceramic.

The compressive test result of TiO_2 ceramic and Ti6Al4V-TiO_2 lattice composite was captured (Figure 10) and showed the benefits of lattice structure objects perfectly. Finite element analysis prepares an estimation of metal–ceramic composite materials strength produced by combining SLM-SPS technique subjected impact, abrasion or compression loading [15–17]. Numerical simulation illustrated that fracture will occur at around 500 MPa for pure ceramic, while buckling for metallic lattice will start from 1200 MPa (Figure 11). Damage tolerance of Ti6Al4V-TiO_2 composite depends on the densification of ceramic (SLM parameters) and metal–ceramic bonding phase (SPS parameters).

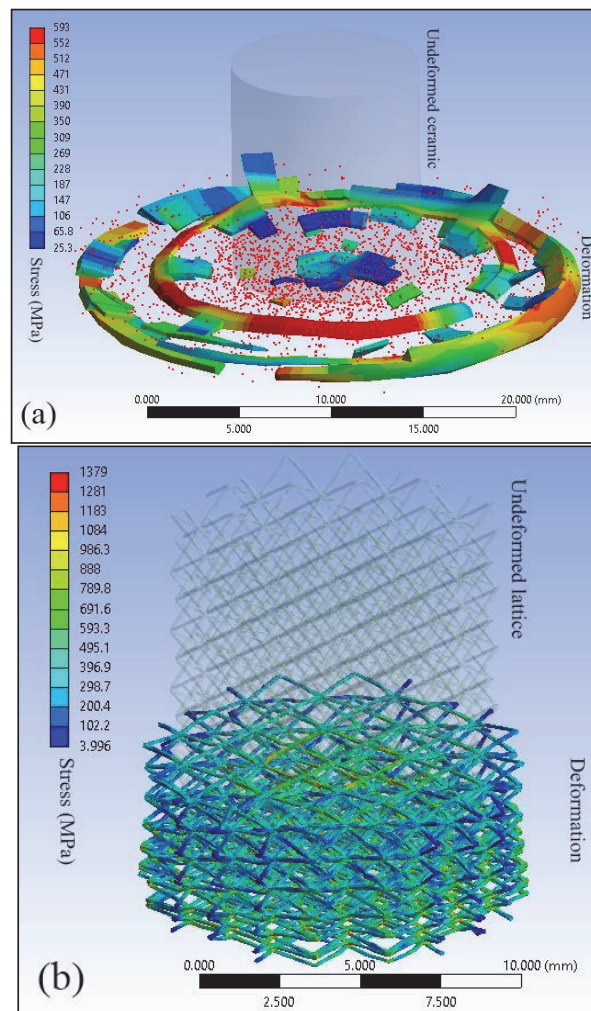


Figure 11. Compressive strength modelling of (a) TiO₂ ceramic, (b) Ti6Al4V lattice structure. Simulation conditions and dimensions are identical for the ceramic and lattice structures.

The present work used SPS as a consolidation method, which can produce only simple, cylindrical shapes. Using other hot consolidation methods as hot isostatic pressing or hot forging, 3D shaped hybrid composites could also be manufactured. The ability to produce composites with complex shape could provide new solutions for a number of applications in the field of metal–ceramic hybrids.

This study was unique as there are no prior studies reporting on antibacterial effects of hybrid composite metal–ceramic materials. However, studies on antibacterial effects of Ag-containing ceramic materials have been previously published [18]. In general, those studies have shown the relationship between the amount of silver in the ceramic surface and antibacterial activity [19] and the importance of segregation and agglomeration of silver on the surface for improving antibacterial efficacy [20–22]. Similar observation was also done in this study but only in dark conditions. Under UV-A, the effect of added Ag to ceramics had significantly smaller effect than in dark conditions. We suggest that this was due to Ag ions which drive the antibacterial effect of Ag–ceramic surfaces [23–25] being reduced back to elemental Ag onto the surfaces [14]. Compared with TiO₂–Ag ceramic material, the

antimicrobial effect of hybrid surfaces was drastically reduced (Figure 8). This change could not be only explained by reduced area of antimicrobial TiO₂-Ag surface in composite material as titanium metal lattice occupied 15% to 25% of the surface, depending on the sample. In almost all cases, both in dark and under ultraviolet exposure the antimicrobial effect of composite surfaces was orders of magnitude lower when compared to the fully ceramic surface. The reason for this was not clear, but it could be assumed that there was a combination of direct surface contact and soluble silver toxicity in effect, both dependent on silver exposure at the material surface. These results indicated that if the hybrid composite needed to be exposed on the surface, the metal composition would also need to be chemically modified for an antimicrobial effect. Otherwise, we suggest that in order to preserve the antibacterial activity of the composite material and reduce variability in antibacterial activity results, a thin layer of pure ceramic material should be added to the surface of the composite.

5. Conclusions

An approach to produce titanium/silver-doped titania composites was introduced, by combining of SLM and SPS techniques. The metallic lattice structures were 3D printed, embedded with TiO₂-Ag ceramic powder and consolidated by SPS. Compression strength and damage tolerance of the composites were shown to increase significantly when compared to TiO₂-Ag ceramics. No collapsing of the composites was seen at up to 25% of deformation in the compressive test. Adding metallic lattice to ceramic silver-doped titania material however decreased the antibacterial effect compared with ceramics only, significantly. Thus, we suggest that the composition of metal that is used to produce the lattice should be chemically modified or a thin layer of pure ceramic material should be added to the surface of the composite.

Author Contributions: For research articles with several authors, a short paragraph specifying their individual contributions must be provided. The following statements should be used “conceptualization, R.R. and M.R.; methodology, L.K. and A.I.; software, R.R.; validation, M.R., A.I. and L.K.; formal analysis, R.R.; investigation, R.R. and M.R.; resources, L.K. and A.I.; data curation, M.R.; writing—original draft preparation, R.R.; writing—review and editing, R.R., M.R., A.I. and L.K.; visualization, A.I.; supervision, L.K.; project administration, A.I.; funding acquisition, L.K.”.

Funding: This research was funded by the Estonian Ministry of Education and Research (IUT 19-29; PUT 748; IUT 23-5; base funding provided to R&D institutions B56 and SS427; M-ERA.NET DURACER project ETAG18012); The European Regional Fund, project number 2014-2020.4.01.16-0183 (Smart Industry Centre) and ERDF project TK134.

Acknowledgments: The authors would like to thank Mart Viljus for the help with EDS mapping.

Conflicts of Interest: The authors declare that there are no conflicts of interest.

References

1. He, C.; Yu, Y.; Hu, X.; Larbot, A. Influence of silver doping on the photocatalytic activity of titania film. *Appl. Surf. Sci.* **2002**, *200*, 239–247. [[CrossRef](#)]
2. Sung-Suh, H.M.; Choi, J.R.; Hah, H.J.; Koo, S.M.; Bae, Y.C. Comparison of Ag deposition effects on the photocatalytic activity of nanoparticulate TiO₂ under visible and UV light irradiation. *J. Photochem. Photobiol. Chem.* **2004**, *163*, 37–44. [[CrossRef](#)]
3. Zhao, L.; Wang, H.; Huo, K.; Cui, L.; Zhang, W.; Ni, H.; Zhang, Y.; Wu, Z.; Chu, P.K. Antibacterial nano-structured titania coating incorporated with silver nanoparticles. *Biomaterials* **2011**, *32*, 5706–5716. [[CrossRef](#)] [[PubMed](#)]
4. Oja Acik, I.; Junolainen, A.; Mikli, V.; Danilson, M.; Krunks, M. Growth of ultra-thin TiO₂ films by spray pyrolysis on different substrates. *Appl. Surf. Sci.* **2009**, *256*, 1391–1394. [[CrossRef](#)]
5. Kim, H.C.; Park, H.K.; Shon, I.J.; Ko, I.Y. Fabrication of ultra-fine TiO₂ Ceramics by a high-frequency induction heated sintering method. *J. Ceram. Process. Res.* **2006**, *7*, 327.
6. Matsuno, H.; Yokoyama, A.; Watari, F.; Uo, M.; Kawasaki, T. Biocompatibility and osteogenesis of refractory metal implants, titanium, hafnium, niobium, tantalum and rhenium. *Biomaterials* **2001**, *22*, 1253–1262. [[CrossRef](#)]

7. Asa'ad, F.; Pagni, G.; Pilipchuk, S.P.; Gianni, A.B.; Giannobile, W.V.; Rasperini, G. 3D-Printed Scaffolds and Biomaterials: Review of Alveolar Bone Augmentation and Periodontal Regeneration Applications. *Int. J. Dent.* **2016**, *2016*, 1239842. [[CrossRef](#)]
8. Vandenbroucke, B.; Kruth, J.P. Selective laser melting of biocompatible metals for rapid manufacturing of medical parts. *Rapid Prototyp. J.* **2007**, *13*, 196–203. [[CrossRef](#)]
9. Könönen, M.; Kivilahti, J. Concise review biomaterials & bioengineering: Fusing of dental ceramics to titanium. *J. Dent. Res.* **2001**, *80*, 848–854.
10. Zhang, C.; Chaudhary, U.; Lahiri, D.; Godavarty, A.; Agarwal, A. Photocatalytic activity of spark plasma sintered TiO₂-graphene nanoplatelet composite. *Scr. Mater.* **2013**, *68*, 719–722. [[CrossRef](#)]
11. Lee, Y.; Lee, J.H.; Hong, S.H.; Kim, D.Y. Preparation of nanostructured TiO₂ ceramics by spark plasma sintering. *Mater. Res. Bull.* **2003**, *38*, 925–930. [[CrossRef](#)]
12. Noh, J.H.; Jung, H.S.; Lee, J.K.; Kim, J.R.; Hong, K.S. Microwave dielectric properties of nanocrystalline TiO₂ prepared using spark plasma sintering. *J. Eur. Ceram. Soc.* **2007**, *2*, 2937–2940.
13. Bernasconi, R.; Carrara, E.; Hoop, M.; Mushtaq, F.; Chen, X.; Nelson, B.J.; Pané, S.; Credi, C.; Levi, M.; Magagnin, L. Magnetically navigable 3D printed multifunctional microdevices for environmental applications. *Addit. Manuf.* **2019**, *28*, 127–135. [[CrossRef](#)]
14. Visnapuu, M.; Rosenberg, M.; Truska, E.; Nommiste, E.; Sutka, A.; Kahru, A.; Rahn, M.; Vija, H.; Orupold, K.; Kisand, V.; et al. UVA-induced antimicrobial activity of ZnO/Ag nanocomposite covered surfaces. *Colloids Surf. B Biointerfaces* **2018**, *169*, 222–232. [[PubMed](#)]
15. Rahmani, R.; Antonov, M.; Kamboj, N. Modelling of impact-abrasive wear of ceramic, metallic, and composite materials. *Proc. Est. Acad. Sci.* **2019**, *68*, 191–197.
16. Rahmani, R.; Antonov, M.; Kollo, L. Wear Resistance of (Diamond-Ni)-Ti6Al4V Gradient Materials Prepared by Combined Selective Laser Melting and Spark Plasma Sintering Techniques. *Adv. Tribol.* **2019**, *2019*, 5415897. [[CrossRef](#)]
17. Rahmani, R.; Antonov, M.; Kollo, L. Selective Laser Melting of Diamond-Containing or Postnitrided Materials Intended for Impact-Abrasive Conditions: Experimental and Analytical Study. *Adv. Mater. Sci. Eng.* **2019**, *2019*, 4210762. [[CrossRef](#)]
18. Velasco, S.C.; Cavaleiro, A.; Carvalho, S. Functional properties of ceramic-Ag nanocomposite coatings produced by magnetron sputtering. *Prog. Mater. Sci.* **2016**, *84*, 158–191. [[CrossRef](#)]
19. Hsieh, J.H.; Tseng, C.C.; Chang, Y.K.; Chang, S.Y.; Wu, W. Antibacterial behavior of TaN-Ag nanocomposite thin films with and without annealing. *Surf. Coat. Technol.* **2008**, *202*, 5586–5589.
20. Wickens, D.J.; West, G.; Kelly, P.J.; Verran, J.; Lynch, S.; Whitehead, K.A. Antimicrobial activity of nanocomposite zirconium nitride/silver coatings to combat external bone fixation pin infections. *Int. J. Artif. Organs.* **2012**, *35*, 817–825.
21. Hsieh, J.H.; Chang, C.C.; Li, C.; Liu, S.J.; Chang, Y.K. Effects of Ag contents on antibacterial behaviors of TaON-Ag nanocomposite thin films. *Surf. Coat. Technol.* **2010**, *205*, 337–340.
22. Huang, H.L.; Chang, Y.Y.; Lai, M.C.; Lin, C.R.; Lai, C.H.; Shieh, T.M. Antibacterial TaN-Ag coatings on titanium dental implants. *Surf. Coat. Technol.* **2010**, *205*, 1636–1641. [[CrossRef](#)]
23. Jamuna-Thevi, K.; Bakar, S.A.; Ibrahim, S.; Shahab, N.; Toff, M.R.M. Quantification of silver ion release, in vitro cytotoxicity and antibacterial properties of nanostructured Ag doped TiO₂ coatings on stainless steel deposited by RF magnetron sputtering. *Vacuum* **2011**, *86*, 235–241. [[CrossRef](#)]
24. Song, D.H.; Uhm, S.H.; Kim, S.E.; Kwon, J.S.; Han, J.G.; Kim, K.N. Synthesis of titanium oxide thin films containing antibacterial silver nanoparticles by a reactive magnetron co-sputtering system for application in biomedical implants. *Mater. Res. Bull.* **2012**, *47*, 2994–2998.
25. Ferraris, M.; Miola, S.; Ferraris, S.; Gautier, G.; Maina, G. Chemical, mechanical, and antibacterial properties of silver nanocluster-silica composite coatings obtained by sputtering. *Adv. Eng. Mater.* **2010**, *12*, 276–282.




Publication III

R. Rahmani; M. Antonov; L. Kollo; Y. Holovenko; P. K. Gokuldoss; Mechanical Behavior of Ti6Al4V Scaffolds Filled with CaSiO₃ for Implant Applications, Applied Sciences 9 (2019) 1-11.

Article

Mechanical Behavior of Ti6Al4V Scaffolds Filled with CaSiO₃ for Implant Applications

Ramin Rahmani ^{1,*}, Maksim Antonov ¹, Lauri Kollo ¹, Yaroslav Holovenko ¹ and Konda Gokuldoss Prashanth ^{1,2,3,*} 

¹ Department of Mechanical and Industrial Engineering, Tallinn University of Technology, Ehitajate tee 5, 19086 Tallinn, Estonia; maksim.antonov@taltech.ee (M.A.); lauri.kollo@taltech.ee (L.K.); yaholo@taltech.ee (Y.H.)

² Erich Schmid Institute of Materials Science, Austrian Academy of Science, Jahn Straße 12, A-8700 Leoben, Austria

³ CBCMT, School of Mechanical Engineering, VIT University, Vellore, Tamil Nadu 632014, India

* Correspondence: ramin.rahmaniahranjani@taltech.ee (R.R.); kgprashanth@gmail.com (K.G.P.)

Received: 30 August 2019; Accepted: 10 September 2019; Published: 13 September 2019



Abstract: Triply periodic minimal surfaces (TPMS) are becoming increasingly attractive due to their biomedical applications and ease of production using additive manufacturing techniques. In the present paper, the architecture of porous scaffolds was utilized to seek for the optimized cellular structure subjected to compression loading. The deformation and stress distribution of five lightweight scaffolds, namely: Rectangular, primitive, lattice, gyroid and honeycomb Ti6Al4V structures were studied. Comparison of finite element simulations and experimental compressive test results was performed to illustrate the failure mechanism of these scaffolds. The experimental compressive results corroborate reasonably with the finite element analyses. Results of this study can be used for bone implants, biomaterial scaffolds and antibacterial applications, produced from the Ti6Al4V scaffold built by a selective laser melting (SLM) method. In addition, Ti6Al4V manufactured metallic lattice was filled by wollastonite (CaSiO₃) through spark plasma sintering (SPS) to illustrate the method for the production of a metallic-ceramic composite suitable for bone tissue engineering.

Keywords: Ti6Al4V scaffolds; triply periodic minimal surfaces; selective laser melting; additive manufacturing; biomaterial applications; finite element analysis; spark plasma sintering; wollastonite

1. Introduction

Titanium and its alloys have been widely used for biomedical and orthopedic applications, such as hip, knee, femur, vertebra, bone and skull, due to their excellent antibacterial/biocompatibility, strength-to-weight ratio and wear and corrosion resistance in comparison with stainless steel [1–5]. Implants have been made by computer numeric control (CNC) machining, or powder metallurgy, followed by different post-processing procedures. The metallic biomaterial scaffolds are applied for stent placement [6] or bone replacement [7]. Three dimensional (3D) printed porous scaffolds are suitable for seeding cells, delivering drugs, and are able to carry compression/tensile loading [2,3]. Biological activities along the scaffold surface (cell growth) and structural design of the scaffolds for additive manufacturing (AM) are both very important, and extensive research has been conducted [8]. With the use of optimal scaffold material and the suitable design for AM, scaffolds with added functionalities, elastic modulus, and strength matching the human bone can be realized [9].

Triply periodic minimal surfaces (TPMS) are some of the designs that are expected to be optimal candidates for bone tissue engineering applications. Primary simulation of the TPMS are crucial for designing these scaffolds to figure out the stress distribution, deformation and failure mechanism of porous structure [10,11].

Gradient structures, unit cell size, strut diameter, the volume fraction of the sample, plasticity and damage tolerance, as well as the minimizing of cost/time are considered during the computer-aided design (CAD) and simulation. In order to have optimized lightweight structures under loading and in vivo or in vitro conditions, printed scaffolds can be graded axially or radially [12]. Recently, research is focused upon polymeric printing using polyjet/inkjet deposition [13], which is faster with no post-processing, unlike metal printing. However, the low mechanical properties of polymer 3D printed materials make it non-applicable for in vivo conditions. Porous Ti6Al4V structures have yield strength and compressive strength in the range of 90–220 MPa [14]. The computer-aided design (CAD) of porous scaffolds and finite element analysis (FEA) have recently attracted much attention in the tissue engineering field. Fluid permeability [15] and biocompatibility [16] of scaffolds depends directly on the pore geometry and topology [17] of structures. The curved shape, smoothness, good flowability, 3D manufacturability and biocompatibility of Ti6Al4V powder particles makes Ti-based alloy promising for load bearing bone implants [18]. It is well known that the artificial bone scaffolds should have the following characteristics: (1) Biocompatibility with living tissues; (2) mechanical properties for trabecular bone and cortical bone (ranging from 0.7 to 15 MPa till >100 MPa [19]); and (3) porous fabricated structures for osteoporosis diseases. Periodic porous materials like TPMS are potential candidates for biomimetic scaffold architecture [19]. The main advantage of TPMS scaffolds is the open interconnected cell structure, deemed to facilitate cell migration, vitalization and vascularization, while retaining a high degree of structural stiffness [20]. Henceforth, mechanical properties, especially compressive strength, is considered as an important parameter for TPMS scaffolds. In this paper, we have performed compressive tests, where the experimental results are compared with the FEA for the selected promising TPMS structures.

Ti6Al4V is considered as excellent biomaterial because of higher fatigue strength, tensile strength and compressive strength [21–24]. However, it is bioinert, where an improper integration takes place with the host bone, resulting in a weak interfacial bond. As a result, at the bone-implant interface, there can be an accumulation of the necrotic fibrous tissue [25]. Nevertheless, in vivo life of the load bearing scaffolds can be increased by improving the interfacial bond of the bone and the metallic scaffolds. To improve the interfacial bonding, Ti6Al4V scaffolds are filled with wollastonite. Spark plasma sintering (SPS) was used for integrating wollastonite into the cellular Ti6Al4V structure [26]. Highly porous acicular wollastonite (CaSiO_3) with micro- or nano-sized pores results in high corrosion resistance and good biocompatibility [27,28].

Hence, the present study aims to fabricate Ti6Al4V scaffolds reinforced with bioactive elements (wollastonite) for the proper integration of the implant to the bone via tissue growth. By reviewing the articles, the deficiency of comparison between the mechanical properties of scaffolds, FEA, and an assortment of them regarding the applications is tangible. Five different Ti6Al4V scaffolds (samples) with identical outside dimensions and similar weight, namely: Rectangular, primitive, lattice, gyroid and honeycomb, were considered. They were chosen based on the desire to provide a continuous surface that is important for the growth/cultivation of viable cells and other aspects of tissue engineering [29]. The rectangular type has vertical available surface, whereas the primitive is made by sequential hollow spheres (proper for fluid permeability and drug delivery). Therefore, scaffolds A and B have vertical flat and spherical areas to flourish the cells. In the case of the lattice type structure, it is possible to specify the size of the cell and the diameter of the strut to figure out the proper cylindrical surface of the metallic rods. It is an intersecting cellular structure that is easy to use during the following of the SPS process, since it can be easily modeled, printed and filled by binder powders, and also allows a larger shrinkage required to produce hard metal-ceramic composites with a low porosity level by SPS [30]. The gyroid-type structure represents irregular continuous curves, and honeycomb considers embedded tubes, which are connected by horizontal washers.

A SolidWorks design and Ansys FEA combination were used to generate these structures and to further anticipate the mechanical behavior of the scaffolds subjected to compressive loading. The results from simulations are compared with the experimental compressive results.

2. Materials and Methods

Five distinct scaffolds were designed by SolidWorks, as shown in Figure 1 (rectangular, primitive, lattice, gyroid and honeycomb, respectively). The names are chosen according to the shape of the structures. These computer-aided design (CAD) models can be used both in finite element analysis (FEA) for the simulation of mechanical properties and the selective laser melting (SLM) process for the fabrication of the real parts. All the five scaffolds were of the following dimensions: A diameter of 20 mm and a height of 15 mm. The weight range of these samples varied between ≈ 3.8 and 5.5 g. Ti6Al4V powders with size of 10–45 μm (produced by a gas atomization process) from TLS Technik were used as the raw material for the production of triply periodic minimal surfaces (TPMS)-type scaffolds.

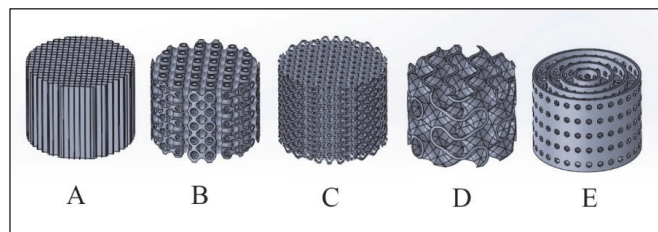


Figure 1. Scaffolds with: (A) Rectangular-, (B) Primitive-, (C) Lattice-, (D) Gyroid- and (E) Honeycomb-type structures (Dimensions: 20 mm in diameter and with 15 mm height), designed via computer-aided design (CAD) software.

A Realized SLM50 device with a maximum laser power of 120 W was used for the fabrication of the scaffolds. The following parameters were used for the fabrication of Ti6Al4V by SLM: Laser current 3000 mA, exposure time 600 μs , point distance 1 μm and unit cell size 1.5 mm. These are standard parameters that are observed for the fabrication of the Ti6Al4V samples. SLM-SPS processes were combined for producing metal-ceramic hybrid composites, which is suggested for chronic osteomyelitis, Vancomycin local delivery, and infected bones replacement in the field of tissue engineering [9]. The entire spark plasma sintering (SPS) setup is kept under the glovebox, in order to maintain the consolidation process in an inter atmosphere. This also helps in avoiding oxygen contamination during the SPS consolidation process. Microstructure of the samples were observed using scanning electron microscope (SEM), (Zeiss EVO MA 15, Germany)

Structural explicit dynamics using the AUTODYN solver and arbitrary Lagrange-Euler (ALE) method via ANSYS Workbench 17.2 is applied for these simulations. A high-quality finite element analysis (FEA) mesh is generated to gain a high-resolution response. The linearized governing motion equation in cylindrical coordinates (r, θ, z) can be expressed by [31]:

$$\frac{\partial \sigma_{rr}}{\partial r} + \frac{1}{r} \frac{\partial \sigma_{r\theta}}{\partial \theta} + \frac{\partial \sigma_{rz}}{\partial z} + \frac{1}{r} (\sigma_{rr} - \sigma_{\theta\theta}) + F_r = \rho \frac{\partial^2 u_r}{\partial t^2} \quad (1)$$

$$\frac{\partial \sigma_{r\theta}}{\partial r} + \frac{1}{r} \frac{\partial \sigma_{\theta\theta}}{\partial \theta} + \frac{\partial \sigma_{\theta z}}{\partial z} + \frac{2}{r} \sigma_{r\theta} + F_\theta = \rho \frac{\partial^2 u_\theta}{\partial t^2} \quad (2)$$

$$\frac{\partial \sigma_{rz}}{\partial r} + \frac{1}{r} \frac{\partial \sigma_{\theta z}}{\partial \theta} + \frac{\partial \sigma_{zz}}{\partial z} + \frac{2}{r} \sigma_{rz} + F_z = \rho \frac{\partial^2 u_z}{\partial t^2} \quad (3)$$

where, $\sigma_{ij} = \sigma_{ji}$ is the Cauchy stress tensor, u_i is displacement, ρ is density and F_i is body force ($F_r = F_\theta = 0$, $F_z = \text{axial compression}$). In the simulation, compressive punches are assumed rigid (unchanged dimension). Bottom punch is the fixed support and the top punch was kept moving until a maximum force of 100 kN (safe loading of machine), or a maximum deformation of 10 mm (with rate of 2 mm/min), is reached. Both the experimental tests and the numerical simulations have identical

boundary conditions. An Instron 8500 apparatus was used for measuring the compression tests of these scaffolds.

3. Biomaterial Production and Characterization

Figure 2 shows the five different TPMS scaffolds with a diameter of 20 mm and a 15 mm height. The five different TPMS scaffold types are: (a) Rectangular with a vertical flat area, (b) primitive, (c) lattice, (which is a very common type of structure produced using SLM [32]), (d) gyroid and (e) honeycomb (which is another common structure that is produced by SLM). Similarly Figures 3–7 exhibits the stress distribution and deformation in the five different TPMS scaffolds.

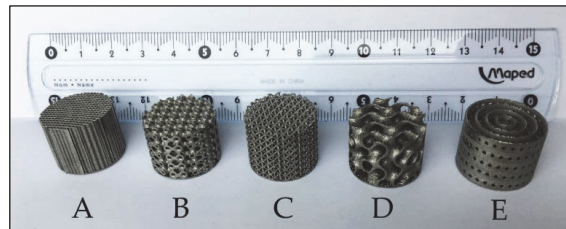


Figure 2. Scaffolds (their weight indicated in parentheses) with: (A) Rectangular (3.97 g), (B) Primitive (5.35 g), (C) Lattice (3.78 g), (D) Gyroid (4.04 g) and (E) Honeycomb (5.52 g) structures with 20 mm diameter and 15 mm height manufactured by selective laser melting.

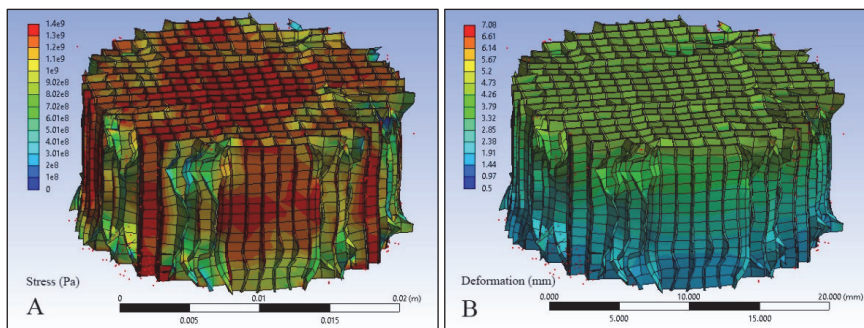


Figure 3. Rectangular scaffold simulation: (A) Stress and (B) displacement (final height after compression: $15 - 4.26 = 10.74$ mm; red dots are separated particles in contact with compressive punches).

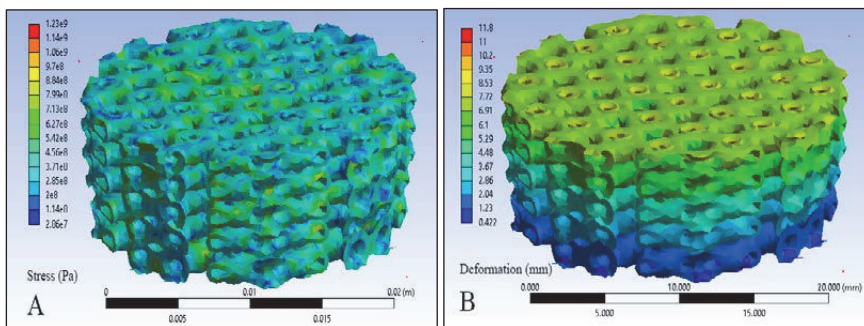


Figure 4. Primitive scaffold simulation: (A) Stress and (B) displacement (final height after compression $15 - 6.91 = 8.09$ mm; the red dots are separated particles in contact with compressive punches).

The 99.9% purity wollastonite (CaSiO_3) with a particle size of 1–5 μm (supplied by NYAD, grade 1250) is filled and sintered (fritting) inside an argon-atomized Ti6Al4V cellular lattice structure via an SPS machine (made by FCT Systeme), as shown in Figure 8. The process was performed with an optimal pressure of 30 MPa at a temperature of 1100 $^\circ\text{C}$, with a heating rate of 100 $^\circ\text{C}/\text{min}$ and a holding time of 5 min [33].

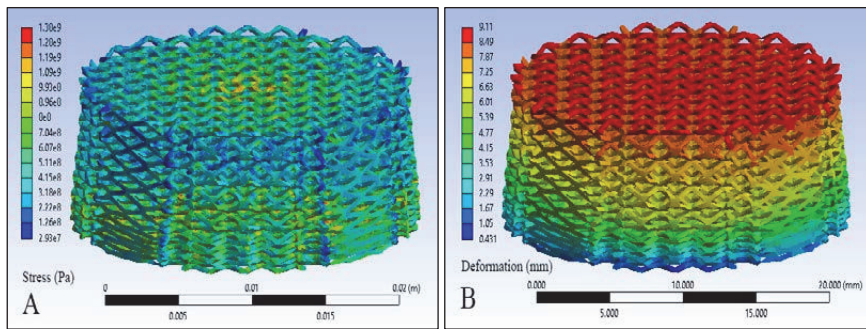


Figure 5. Lattice scaffold simulation: (A) Stress and (B) displacement (final height after compression 15 – 9.11 = 5.89 mm; red dots are separated particles in contact with compressive punches).

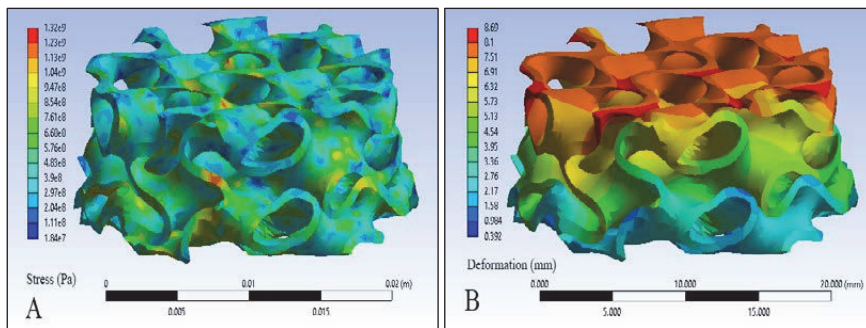


Figure 6. Gyroid scaffold simulation: (A) Stress and (B) displacement (final height after compression 15 – 8.1 = 6.9 mm; these red dots are separated particles in contact with compressive punches).

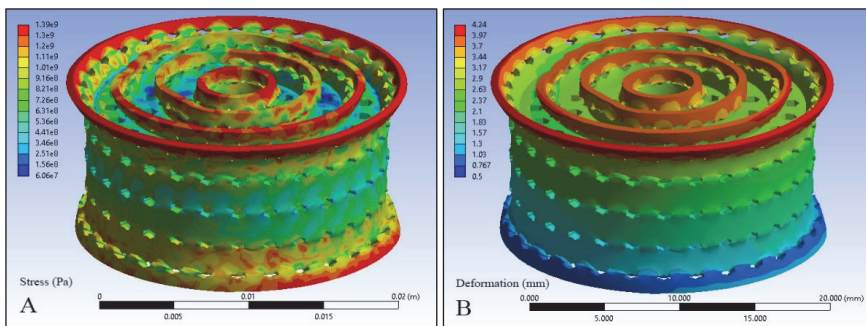


Figure 7. Honeycomb scaffold simulation: (A) Stress and (B) displacement (final height after compression 15 – 4.24 = 10.76 mm; red dots are separated particles in contact with compressive punches).

Wollastonite composition consists theoretically of 48.28% CaO and 51.72% SiO₂, while usually, the natural mineral may contain small amounts of iron, aluminum, magnesium, potassium and sodium (Figures 8A and 9A). An SLM-manufactured Ti6Al4V lattice with 1 mm cell size filled by CaSiO₃ powder and sintered in SPS (Figures 8B and 9B) are shown. The results show a good boundary between ceramic and lattice after SPS and polishing (Figures 8C and 9C).

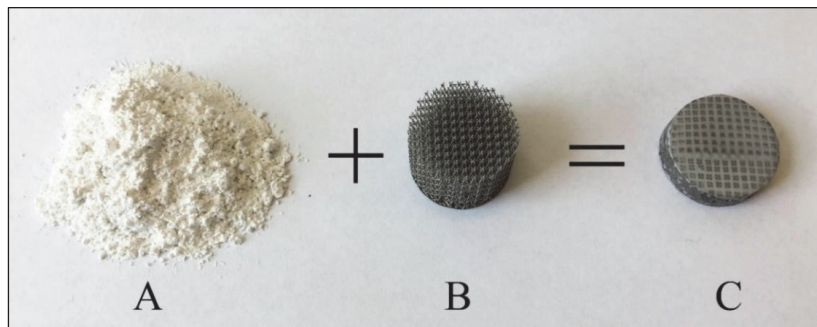


Figure 8. (A) Wollastonite (CaSiO₃) powder, (B) selective laser melting (SLM)-produced Ti6Al4V lattice structure with 1 mm cell size, and (C) Sintered sample (dimensions of lattice structure: 20 mm diameter and 15 mm height before spark plasma sintering (SPS) and 6 mm height after SPS and polishing).

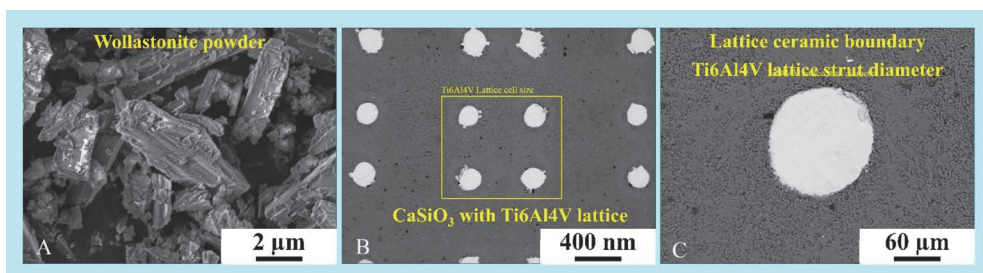


Figure 9. SEM micrographs of (A) wollastonite (CaSiO₃) powder, (B) Sintered CaSiO₃ embedded in a Ti6Al4V lattice after SPS, and (C) High magnification image of metal-ceramic boundary.

4. Results and Discussion

An *in vitro* simulation and experimental results are required before an *in vivo* assessment of any biomaterial. From the literature, the ultimate strength of Ti6Al4V manufactured by SLM or electron beam melting (EBM) can be found between ≈ 1.0 – 1.2 GPa [34,35], and this value is applied for simulations in the current research. The rectangular scaffold (Figure 3) exhibits a high compressive strength, and deformation mostly occurs in the top and/or bottom part of the sample. The final height of rectangular and honeycomb after the compression test are similar. Comparison between Figures 3 and 7 present the findings that due to interlayer horizontal sheets, embedded multi-tubes (inspired by multi-walled carbon nanotubes) and hexagonal pores, the honeycomb scaffold has less stress concentration values; it is wrinkled with an expansion in diameter.

As expected, primitive, lattice and gyroid scaffolds (Figures 4–6) exhibited uniform deformation. For these three conditions, adding layers upon layers with a defined unit cell size (for example a lattice with intersecting cellular rods) produce desired structure shapes easily, but will be deformed relatively easily during compressive loading. It shows that cell type, size and alignment together play a pivotal role on their failure mechanism [36]. The experimental stress-strain curves from the compression test are shown in Figure 10. As seen from Figure 10, primitive, lattice and gyroid scaffolds show a more inferior deformation stress than in the case of rectangular scaffolds. In addition, the rectangular

scaffold shows uniform plastic deformation allowances, where the stresses were distributed uniformly and the local overloading is completely avoided. It is shown that rectangular (due to vertical channels and fluid permeability) and honeycomb (due to horizontal plates and hexagon pores) are structures can bear high compressive loads. As demonstrated in section views of Figure 11, rectangular scaffolds have vertical thin plates that are resistant against distortion and deformation, whereas, honeycomb is more suitable for alive cell growth due to horizontal plates and continuous open porosity.

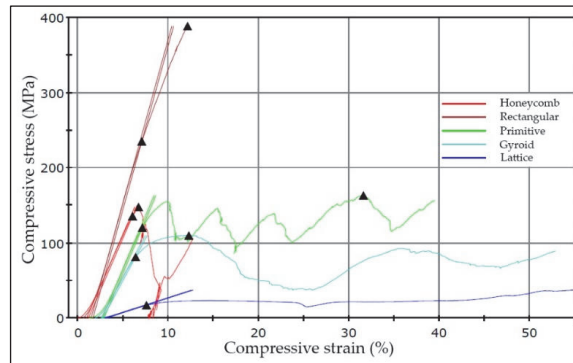


Figure 10. Stress-Strain compression results of scaffolds produced using the selective laser melting.

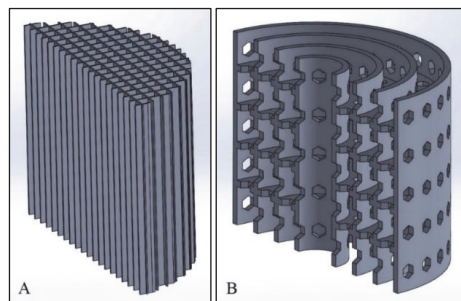


Figure 11. Section view of: (A) Rectangular, and (B) Honeycomb scaffolds.

The applicability of the porous TPMS scaffolds can be extended to applications related to (1) oxygen transport and/or (2) scaffold permeability [37]. The porous TPMS scaffolds can also contribute to enhanced cell seeding, and at the same time can maintain nutrient transport throughout the whole scaffold during in vitro culturing [16]. Regarding the final height of the deformed samples, the experimental compressive results (Figure 12A–E) are compared with the FEA analytical outcomes (Figures 3B, 4B, 5B, 6B and 7B), which are in good agreement. Regarding the Von Mises stress distribution (Figures 3A, 4A, 5A, 6A and 7A), primitive, lattice and gyroid scaffolds are relatively flexible/deformable structures, while more deformation energy can be absorbed by rectangular and honeycomb structures. Hence, for the rectangular structure, stress concentration and distortion can appear in the upper part of sample, but honeycomb failure started from the bottom of structures. Adding metallic lattice structure (Ti6Al4V) to ceramic reinforcement like wollastonite (CaSiO_3) produces a composite with higher wear resistance, damage tolerance and mechanical properties resulting in a higher durability of bones [38,39]. The strut diameter of the lattice is currently $\approx 200 \mu\text{m}$, while it could be increased up to 1 mm (Figure 9C). This ability helps to control volume fraction of both Ti6Al4V and CaSiO_3 in the composite required to achieve the density and porosity characteristic for bones. Besides, our SLM-SPS combination provides the possibility of making complicated shapes/structures for antibacterial or biomedical applications (Figure 8C). Height of scaffolds after the analytical and

experimental compression test are presented in Table 1. Statistical comparison shows a satisfying agreement between them. For Lattice scaffold (1 mm cell size and 0.5 mm strut diameter), the simulation outcomes show relatively lower weight than the experimental results. Such differences between the simulation and experimental results may be attributed to the porosity and unmelted/attached Ti6Al4V particles in the SLM parts [38,40].

Table 1. Compression test data (comparison of finite element analysis (FEA) simulation and experimental results).

Scaffold Type	Weight Before Test (g) (Figure 2)	Volume Fraction (% of Metal)	Height after Simulation (mm) (Figures 3–7)	Height after Experiment (mm) (Figure 8)	Maximum Compressive Load (kN) (Figure 9)
Rectangular	4.0 ± 0.1	19 ± 1	11 ± 1	11 ± 2	100 ± 5
Primitive	5.4 ± 0.2	28 ± 1	8 ± 2	8 ± 2	52 ± 2
Lattice	3.8 ± 0.1	17 ± 2	6 ± 2	8 ± 2	12 ± 1
Gyroid	4.0 ± 0.1	26 ± 2	7 ± 2	8 ± 1	35 ± 2
Honeycomb	5.6 ± 0.1	19 ± 1	11 ± 1	12 ± 3	70 ± 4

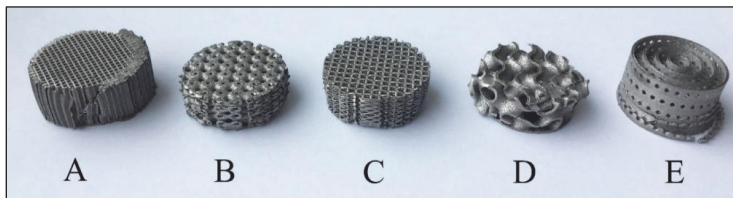


Figure 12. Triply periodic minimal surfaces (TPMS) scaffolds after compressive test with indication of their final height: (A) Rectangular –11 mm, (B) Primitive –8.4 mm, (C) Lattice –8.8 mm, (D) Gyroid –7.6 mm and (E) Honeycomb –12.1 mm.

Primitive TPMS have the highest volume fraction (28.2%, Table 1), and it might be interesting for biological activities due to a larger specific surface area. Stress distribution was uniform (Figure 4A), and shows a least difference between the simulation and experiment result (Figure 12B). Gyroid shows similar behavior as primitive, but including some broken/separated pieces in the top area because of a curvy cross section surface under compression. Strength of rectangular scaffold (Figure 12A) subjected to compressive loading is presented in Figure 9 and Table 1.

It survived under the maximum test load (100 kN). Comparison between A and Figure 12A shows that middle rectangular sections are less affected during compression, and any major deformation starts from the outer layers. Rectangular structure with rectangular/vertical channels is supposed for cells viability, oxygen transport and fluid permeability, otherwise it can be reinforced by horizontal plates (similar to honeycomb, Figure 11) for higher resistance against shear stress.

5. Conclusions

In this paper, five different Ti6Al4V triply periodic minimal surface structures with different surface areas were created by CAD design, namely rectangular, primitive, lattice, gyroid and honeycomb. The finite element simulation in comparison with 3D additive manufactured experimental results illustrated similar mechanical behaviors when the samples were subjected to compressive loading. They had uniform stress distributions and relatively identical displacements. It was found that ANSYS simulation has a potential to predict the mechanical behavior of additively manufactured scaffolds. Rectangular and honeycomb were novel cellular scaffolds designed for high compressive load-bearing and biological application with vertical and horizontal available surfaces, respectively. Rectangular scaffold is identified as suitable for oxygen transport and fluid permeability, whereas, honeycomb is

found to be the best for the growth of cells. SLM-manufactured Ti6Al4V lattice can be sintered via SPS along with CaSiO₃ for load bearing bone replacements.

Author Contributions: Conceptualization, R.R. and K.G.P.; methodology, M.A. and L.K.; investigation, R.R. and Y.H.; writing—original draft preparation, R.R.; writing—review and editing, M.A., L.K. and K.G.P.; supervision, M.A. and L.K.; funding acquisition, M.A., L.K. and K.G.P.

Funding: This research was supported by the Estonian Ministry of Education and Research under projects IUT19-29, the European Regional Fund, project number 2014-2020.4.01.16-0183 (Smart Industry Centre), ETAG18012, MOBERC15 and by base finance project B56 and SS427 of Tallinn University of Technology.

Conflicts of Interest: The authors declare no conflict of interest.

References

1. Khan, M.A.; Williams, R.L.; Williams, D.F. In-vitro corrosion and wear of titanium alloys in the biological environment. *Biomaterials* **1996**, *17*, 2117–2126. [[CrossRef](#)]
2. Zhuravleva, K.; Boenisch, M.; Prashanth, K.G.; Hempel, U.; Health, A.; Gemming, T.; Caling, M.; Scudino, S.; Schultz, L.; Eckert, J.; et al. Production of porous β -type Ti-40Nb alloy for biomedical applications: Comparison of selective laser melting and hot pressing. *Materials* **2013**, *6*, 5700–5712. [[CrossRef](#)] [[PubMed](#)]
3. Schwab, H.; Prashanth, K.G.; Loeber, L.; Kuehn, U.; Eckert, J. Selective laser melting of Ti-45Nb alloy. *Metals* **2015**, *5*, 686–694. [[CrossRef](#)]
4. Attar, H.; Loeber, L.; Funk, A.; Calin, M.; Zhang, L.C.; Prashanth, K.G.; Scudino, S.; Zhang, Y.S.; Eckert, J. Mechanical behavior of porous commercially pure Ti and Ti-TiB composite materials manufactured by selective laser melting. *Mater. Sci. Eng. A* **2015**, *625*, 350–356. [[CrossRef](#)]
5. Attar, H.; Prashanth, K.G.; Zhang, L.C.; Calin, M.; Okulov, I.V.; Scudino, S.; Yang, C.; Eckert, J. Effect of powder particle shape on the properties of in situ Ti-TiB composite powders produced by selective laser melting. *J. Mater. Sci. Technol.* **2015**, *31*, 1001–1005. [[CrossRef](#)]
6. Van Lith, R.; Baker, E.; Ware, H.; Yang, J.; Cyrus Farsheed, A.; Sun, C.; Ameer, G. 3D-Printing Strong High-Resolution Antioxidant Bioresorbable Vascular Stents. *Adv. Mater. Technol.* **2016**, *1*, 1600138. [[CrossRef](#)]
7. Seitz, H.; Rieder, W.; Irsen, S.; Leukers, B.; Tille, C. Three-dimensional printing of porous ceramic scaffolds for bone tissue engineering. *J. Biomed. Mater. Res.* **2005**, *74*, 782–788. [[CrossRef](#)] [[PubMed](#)]
8. Wysocki, B.; Idaszek, J.; Szlazak, K.; Strzelczyk, K.; Brynk, T.; Kurzydowski, K.J.; Świąszkowski, W. Post Processing and Biological Evaluation of the Titanium Scaffolds for Bone Tissue Engineering. *Materials* **2016**, *9*, 197. [[CrossRef](#)]
9. Kamboj, N.; Rodríguez, M.A.; Rahmani, R.; Prashanth, K.G.; Hussainova, I. Bioceramic scaffolds by additive manufacturing for controlled delivery of the antibiotic vancomycin. *Proc. Est. Acad. Sci.* **2019**, *68*, 185–190. [[CrossRef](#)]
10. Afshar, M.; Pourkamali Anaraki, A.; Montazerian, H.; Kadkhodapour, J. Additive manufacturing and mechanical characterization of graded porosity scaffolds designed based on triply periodic minimal surface architectures. *J. Mech. Behav. Biomed. Mater.* **2016**, *62*, 481–494. [[CrossRef](#)]
11. Kadkhodapour, J.; Montazerian, H.; Darabi, A.C.; Anaraki, A.P.; Ahmadi, S.M.; Zadpoor, A.A.; Schmauder, S. Failure mechanisms of additively manufactured porous biomaterials: Effects of porosity and type of unit cell. *J. Mech. Behav. Biomed. Mater.* **2015**, *50*, 180–191. [[CrossRef](#)]
12. Afshar, M.; Pourkamali Anaraki, A.; Montazerian, H. Compressive characteristics of radially graded porosity scaffolds architected with minimal surfaces. *Mater. Sci. Eng. C* **2018**, *92*, 254–267. [[CrossRef](#)] [[PubMed](#)]
13. Abueidda, D.W.; Bakir, M.; Abu Al-Rub, R.K.; Bergström, J.S.; Sobh, N.A.; Jasiuk, I. Mechanical properties of 3D printed polymeric cellular materials with triply periodic minimal surface architectures. *Mater. Des.* **2017**, *122*, 255–267. [[CrossRef](#)]
14. Sallica-Leva, E.; Jardini, A.L.; Fogagnolo, J.B. Microstructure and mechanical behavior of porous Ti-6Al-4V parts obtained by selective laser melting. *J. Mech. Behav. Biomed. Mater.* **2013**, *26*, 98–108. [[CrossRef](#)] [[PubMed](#)]
15. Kapfer, S.C.; Hyde, S.T.; Mecke, K.; Arns, C.H.; Schröder-Turk, G.E. Minimal surface scaffold designs for tissue engineering. *Biomaterials* **2011**, *32*, 6875–6882. [[CrossRef](#)]

16. Van Bael, S.; Chai, Y.C.; Truscetto, S.; Moesen, M.; Kerckhofs, G.; Van Oosterwyck, H.; Kruth, J.P.; Schrooten, J. The effect of pore geometry on the in vitro biological behavior of human periosteum-derived cells seeded on selective laser-melted Ti6Al4V bone scaffolds. *Acta Biomater.* **2012**, *8*, 2824–2834. [[CrossRef](#)] [[PubMed](#)]
17. Xiao, D.; Yang, Y.; Su, X.; Wang, D.; Luo, Z. Topology optimization of microstructure and selective laser melting fabrication for metallic biomaterial scaffolds. *Trans. Nonferrous Met. Soc. China* **2012**, *22*, 2554–2561. [[CrossRef](#)]
18. Yan, C.; Haob, L.; Hussein, A.; Young, P. Ti-6Al-4V triply periodic minimal surface structures for bone implants fabricated via selective laser melting. *J. Mech. Behav. Biomed. Mater.* **2015**, *51*, 61–73. [[CrossRef](#)]
19. Vijayavenkataraman, S.; Zhang, L.; Zhang, S.; Ying Hsi Fuh, J.; Feng Lu, W. Triply Periodic Minimal Surfaces Sheet Scaffolds for Tissue Engineering Applications: An Optimization Approach toward Biomimetic Scaffold Design. *ACS Appl. Bio Mater.* **2018**, *1*, 259–269. [[CrossRef](#)]
20. Yoo, D. New paradigms in hierarchical porous scaffold design for tissue engineering. *Mater. Sci. Eng. C* **2013**, *33*, 1759–1772. [[CrossRef](#)]
21. Paital, S.R.; Dahotre, N.B. Laser surface treatment for porous and textured Ca-P bio-ceramic coating on Ti-6Al-4V. *Biomater. Mater.* **2007**, *2*, 274. [[CrossRef](#)] [[PubMed](#)]
22. Prashanth, K.G.; Damodaram, R.; Scudino, S.; Wang, Z.; Prasad Rao, K.; Eckert, J. Friction welding of Al-12Si parts produced by selective laser melting. *Mater. Des.* **2014**, *57*, 632–637. [[CrossRef](#)]
23. Qin, P.T.; Damodaram, R.; Maity, T.; Zhang, W.W.; Yang, C.; Wang, Z.; Prashanth, K.G. Friction welding of electron beam melted Ti-6Al-4V. *Mater. Sci. Eng. A* **2019**, *761*, 138045. [[CrossRef](#)]
24. Zhang, W.; Qin, P.; Wang, Z.; Yang, C.; Kollo, L.; Grzesiak, D.; Prashanth, K.G. Superior wear resistance in EBM-processed TC4 alloy compared with SLM and forged samples. *Materials* **2019**, *12*, 782. [[CrossRef](#)] [[PubMed](#)]
25. Bandyopadhyay, A.; Espana, F.; Balla, V.K.; Bose, S.; Ohgami, Y.; Davies, N.M. Influence of porosity on mechanical properties and in vivo response of Ti6Al4V implants. *Acta Biomater.* **2010**, *6*, 1640–1648. [[CrossRef](#)] [[PubMed](#)]
26. Rahmani, R.; Rosenberg, M.; Ivask, A.; Kollo, L. Comparison of mechanical and antibacterial properties of TiO₂/Ag ceramics and Ti6Al4V-TiO₂/Ag composite materials using combining SLM-SPS techniques. *Metals* **2019**, *9*, 874. [[CrossRef](#)]
27. Papynov, W.K.; Mayorov, V.Y.; Portnyagin, A.S.; Shichalin, O.O.; Koblyakov, S.P.; Kaidalova, T.A.; Nepomnyashiy, A.V.; Sokol'nitskaya, T.A.; Zub, Y.L.; Avramenko, V.A. Application of carbonaceous template for porous structure control of ceramic composites based on synthetic wollastonite obtained via Spark Plasma Sintering. *Ceramics Int.* **2015**, *41*, 1171–1176. [[CrossRef](#)]
28. Xue, W.; Liu, X.; Zheng, X.B.; Ding, C. In vivo evaluation of plasma-sprayed wollastonite coating. *Biomater.* **2005**, *26*, 3455–3460. [[CrossRef](#)]
29. Murphy, S.; Atala, A. 3D bioprinting of tissues and organs. *Nat. Biotech.* **2014**, *32*, 773–785. [[CrossRef](#)]
30. Rahmani, R.; Antonov, M.; Kollo, L. Wear Resistance of (Diamond-Ni)-Ti6Al4V Gradient Materials Prepared by Combined Selective Laser Melting and Spark Plasma Sintering Techniques. *Adv. Tribol.* **2019**, *2019*, 5415897. [[CrossRef](#)]
31. Slaughter, W.S. *The Linearized Theory of Elasticity*; Springer: Berlin/Heidelberg, Germany, 2002.
32. Prashanth, K.G.; Loeber, L.; Klauss, H.-J.; Kuehn, U.; Eckert, J. Characterization of 316L steel cellular dodecahedron structures produced by selective laser melting. *Technologies* **2016**, *4*, 34. [[CrossRef](#)]
33. Wan, X.; Hu, A.; Li, M.; Chang, C.; Mao, D. Performances of CaSiO₃ ceramic sintered by spark plasma sintering. *Mater. Charact.* **2008**, *59*, 256–260. [[CrossRef](#)]
34. Simonelli, M.; Tse, Y.Y.; Tuck, C. Effect of the build orientation on the mechanical properties and fracture modes of SLM Ti-6Al-4V. *Mater. Sci. Eng. A* **2014**, *616*, 1–11. [[CrossRef](#)]
35. Murr, L.E.; Esquivel, E.V.; Quinones, S.A.; Gaytan, S.M.; Lopez, M.I.; Martinez, E.Y.; Medina, F.; Hernandez, D.H.; Martinez, E.; Martinez, J.L.; et al. Microstructures and mechanical properties of electron beam-rapid manufactured Ti-6Al-4V biomedical prototypes compared to wrought Ti-6Al-4V. *Mater. Charact.* **2009**, *60*, 96–105. [[CrossRef](#)]
36. Maskery, I.; Aboulkhair, N.T.; Aremu, A.O.; Tuck, C.J.; Ashcroft, I.A. Compressive failure modes and energy absorption in additively manufactured double gyroid lattices. *Addit. Manuf.* **2017**, *16*, 24–29. [[CrossRef](#)]

37. Truscello, S.; Kerckhofs, G.; Van Bael, S.; Pyka, G.; Schrooten, J.; Van Oosterwyck, H. Prediction of permeability of regular scaffolds for skeletal tissue engineering: A combined computational and experimental study. *Acta Biomater.* **2012**, *8*, 1648–1658. [[CrossRef](#)]
38. Li, H.; Chang, J. Fabrication and characterization of bioactive wollastonite/PHBV composite scaffolds. *Biomaterials* **2004**, *25*, 5473–5480. [[CrossRef](#)]
39. Rahmani, R.; Antonov, M.; Kollo, L. Selective Laser Melting of Diamond-Containing or Postnitrided Materials Intended for Impact-Abrasive Conditions: Experimental and Analytical Study. *Adv. Mater. Sci. Eng.* **2019**, *2019*, 4210762. [[CrossRef](#)]
40. Rahmani, R.; Antonov, M.; Kamboj, N. Modelling of impact-abrasive wear of ceramic, metallic, and composite materials. *Proc. Est. Acad. Sci.* **2019**, *68*, 191–197. [[CrossRef](#)]



© 2019 by the authors. Licensee MDPI, Basel, Switzerland. This article is an open access article distributed under the terms and conditions of the Creative Commons Attribution (CC BY) license (<http://creativecommons.org/licenses/by/4.0/>).

Publication IV

R. Rahmani; M. Antonov; L. Kollo; Selective Laser Melting of Diamond-Containing or Postnitrided Materials Intended for Impact-Abrasive Conditions: Experimental and Analytical Study, *Advances in Materials Science and Engineering* (2019) 1-11.

Research Article

Selective Laser Melting of Diamond-Containing or Postnitrided Materials Intended for Impact-Abrasive Conditions: Experimental and Analytical Study

Ramin Rahmani , Maksim Antonov, and Lauri Kollo

Tallinn University of Technology, Department of Mechanical and Industrial Engineering, Ehitajate Tee 5, Tallinn 19086, Estonia

Correspondence should be addressed to Ramin Rahmani; ramin.rahmaniahranjani@ttu.ee

Received 31 October 2018; Revised 17 May 2019; Accepted 15 June 2019; Published 26 June 2019

Academic Editor: Tomasz Trzepieciński

Copyright © 2019 Ramin Rahmani et al. This is an open access article distributed under the Creative Commons Attribution License, which permits unrestricted use, distribution, and reproduction in any medium, provided the original work is properly cited.

Materials with higher wear resistance are required in various applications including cutting elements (drag bits) of soft ground tunnel boring machines (TBM) to increase the productivity and to reduce the risk for workers involved in exchange operations (dangerous hyperbolic conditions). In recent work, two types of materials were produced by combining 3D printing (selective laser melting, SLM) of cellular lattice structures and spark plasma sintering (SPS) methods. The lattices were printed from (1) 316L stainless steel with diamond and (2) Ti6Al4V with nitriding. The effect of diamond content (5%, 10%, and 20%; nickel-coated particles) and unit cell size on performance was studied. The titanium alloy lattice was nitrided to increase its hardness and wear resistance. The effect of nitriding temperature (750°C, 900°C, and 1050°C) and lattice volume fraction (6%, 15%, and 24%, vol.) was investigated, and the optimized conditions were applied. The lattices were filled with 316L and Ti6Al4V powders, respectively, and consolidated by SPS. Samples were tested with the help of laboratory impact-abrasive tribodevice. Laboratory results have shown that both reinforcing approaches are beneficial and allow improvement of wear resistance in impact-abrasive conditions with great potential for TBM or similar applications. Modelling with the help of finite element method has shown that lattice structure enables reduction of peak local stresses in scratching and impact conditions.

1. Introduction

The combination of simultaneous production methods allows production of materials with improved properties. Materials with higher wear resistance are required in various applications including mining, cutting, drilling, and tunnel boring machines (TBM) to increase the productivity and to reduce the risk for employees and time required for exchange operations. Selective laser melting (SLM) and electron beam melting (EBM) are becoming the most popular techniques in additive manufacturing technology that are developed quickly during the recent decade. Very popular directions are solid prototype complex parts, porous electrothermal and acoustic materials, and lightweight metallic cellular lattice structures. The possibility to create structures with varied lattice cell size, volume

fraction, layer thickness, and strut diameter from various metallic alloys has been very useful for the needs of biomedical, dental, and aerospace industries [1–3]. Starting from the invention of the SLM method, the most researched materials from the groups of stainless steel, titanium, and aluminium alloys were 316L [4], Ti6Al4V [5], and AlSi10Mg [6] due to their rounded shape of powders, good fluidity, great number of suitable applications, and high mechanical properties. Not many studies have been reported regarding other alloyed metals or composite materials. For example, 3D printing of diamond particles (as the hardest material with super hard crystals) needs extremely high temperature, pressure, and laser current. Since it is not possible with current 3D printers, designing special printers or mixing diamond particles with other powders is inevitable. Hence, a combination of lattice 3D

printing and additional postprocessing steps to improve lattice or to consolidate material allows achievement of improved properties required for wear resistance applications. Overall, SLM technique like all other technologies has advantages and drawbacks, such as using the same computer-aided design (CAD) model for printing, manufacturing of fully dense solid or porous parts, printing of complicated parts (implants, for example), ability of simultaneous duplication of the object with the same or various scales and required number versus high cost of powders and apparatuses, part dimension restrictions (to fit into volume of printer's chamber), long process duration for large parts, and required removal and postpolishing operations.

The gyroid periodic lattice structures manufacturability and influence of different unit cell sizes have been studied, and it was found that cell with size being as small as 2 mm can be built without supporting structures (self-supported) [7]. It is usually used to create the first level (*support*) of 3D printed materials adhering to the base platform. Then, there is commonly one solid layer (about 0.1 mm thick that corresponds to about four layers of 25 μm each) between support and following lattice structure to connect them that is called *spacer*. Finite element modelling of body-centred cubic (BCC) structure and the same one with a vertical pillar (BCC-Z) was discussed and compared with experimental samples to illustrate stress and stiffness under loading [8]. Support is helping to fix the printed structure to the platform without causing thermal stress-induced distortions. The effect of support dimensions, volume fraction, and unit cell size of lattice has been compared for gyroid and diamond lattice structure types [9]. Advanced gyroid-type 316L lightweight stainless steel lattice structures with a wide range of volume fractions, unit cell sizes, and orientations have been designed to avoid wastage of material powders to assure an acceptable coincidence of 3D printed and original CAD models [10]. The comparison between SLM-manufactured parts and a CAD model of self-supported diamond-type AlSi10Mg structures has been investigated, and good geometrical compliance and precise mechanical property prediction were demonstrated; however, lattice strut and pore size were slightly higher and lesser than the designed model, respectively [11]. An optimized Ti6Al4V open-cell lattice has been reported along with strain energy calculations, and strength to weight and stiffness to weight ratios [12].

Many of the recent articles more frequently have focused on the adaptation of analytical (finite element model or CAD design) and experimental (SLM manufacturing) results regarding the influence of strut size, cell size, support necessity, and optimum lattice type. Effect of laser power and scanning speed on strut diameter has been thoroughly investigated, and it is in direct proportion with laser power if constant scanning speed is used [13]. The study of AlSi10Mg gyroid-type cellular lattices has confirmed that an increase in the volume fraction of lattice material leads to rising of compressive strength while the increase in unit cell size leads to lower microhardness [14]. It was also found that build orientation of layered manufacturing and heat treatment condition of Ti6Al4V diamond-type cellular lattices under

high pressure of hot isostatic pressing (HIP) is of high importance [15]. Meanwhile, spark plasma sintering as the pulsed electric current method produces near theoretical densified and fast consolidated samples in comparison with conventional powder metallurgy methods. Passing electric current through graphite die has the potential of sintering ceramic-metal mixed powders in nanostructure scale.

Two types of materials were produced by combining 3D printing (SLM) of cellular lattice structures and spark plasma sintering (SPS) techniques (by adding diamond particles or by nitriding). Additionally, the effect of diamond particles content and unit cell size was evaluated to optimize materials for applications where resistance against impact-abrasive action is important (tunnelling, mining, geothermal drilling, etc.). The use of additive manufacturing in industrial applications can facilitate (enable) welding or fixation by bolting of new wear-resistant materials and production of lighter materials or components as it was demonstrated by the current work. The experimental data have supported the results of modelling (scratching and impacting) with the help of finite element (SOLIDWORKS/ANSYS) software. Shortage of finite element modelling of composites (lattice and hard material compact) produced by multistep processes (3D printing and powder metallurgy) under combined tribological loading (impact and abrasive) to assess machine components performance (buttons, inserts, drag bits, etc.) was the motivation of adding dynamic simulation (instead of static) in the current work.

2. Materials and Methods

Stainless steel grade AISI 316L is an austenitic iron-based (with chromium, nickel, and molybdenum additions), low carbon, and the nonmagnetic alloy used for corrosion resistance and additive manufacturing applications. The powders of 316L are spherical and have good flowability that is important for feeding of 3D metal printing machine. Powder (see Figure 1(a)) was supplied by Sandvik Osprey Ltd [16].

Ti6Al4V has excellent strength to weight ratio and a great potential for aerospace, biomedical, and surgical applications. Spherical Ti6Al4V powders (see Figure 1(b)) containing titanium, aluminium, and vanadium were supplied by TLS Technik GmbH [17].

Diamond-type cellular lattices have been printed by Realizer SLM50 machine from 316L and Ti6Al4V (Figures 2 and 3), respectively. The lattice structure was printed with the following parameters: the thickness of one printed layer: 25 μm , laser current: 3000 mA, exposure time: 600 μs , point distance: 1 μm , diameter: 20 mm, and height: 15 mm. Two new types of reinforcement approaches were investigated. The first type of materials was made of 316L stainless steel with a varied percentage of nickel-coated diamond particles. The reinforcement of the second materials was achieved by nitriding of Ti6Al4V lattice printed with different cell sizes. Six samples including two reference materials (316L and Ti6Al4V) with a description of SPS conditions are shown in Table 1. Reference samples (Nos. 5 and 6) are produced directly in the SPS without lattice structure inside. Spark

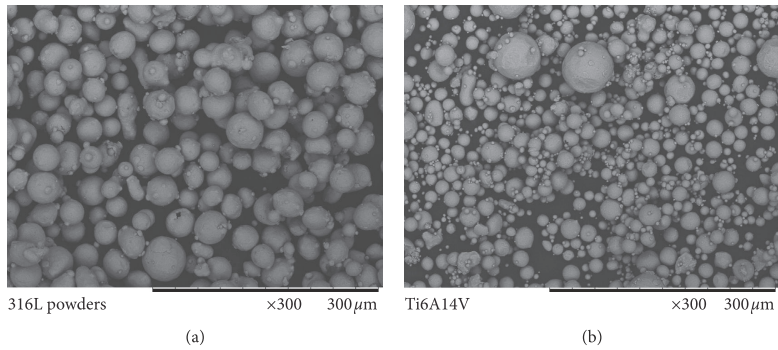


FIGURE 1: SEM micrographs of 316L and Ti6Al4V powders.

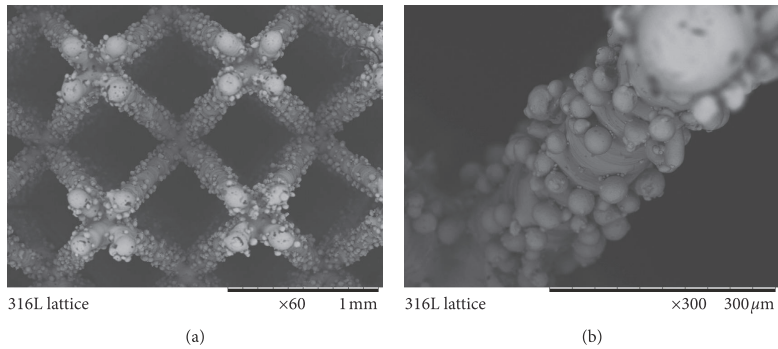


FIGURE 2: SEM micrographs of 3D printed 316L lattice.

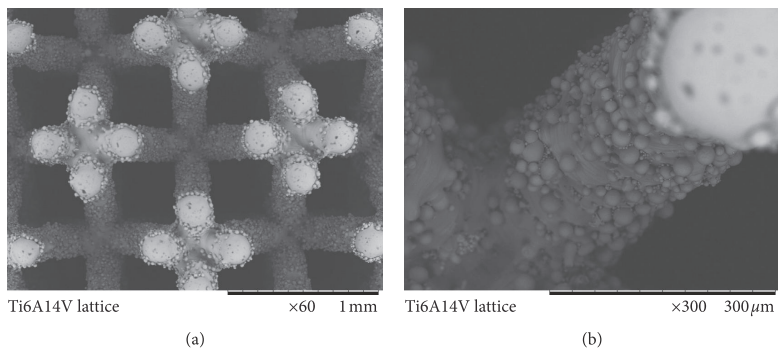


FIGURE 3: SEM micrographs of 3D printed Ti6Al4V lattice.

plasma sintering machine made by FCT Systeme, GmbH, was used for sintering of samples. Vacuum-nitriding furnace (VNF) made by R. D. WEBB, Ltd., was applied for nitriding of Ti6Al4V lattices at different temperatures.

In order to illustrate conditions in which the materials will perform (impact-abrasion), the cutterhead, drag bits, inserts, and buttons of TBM are schematically shown (CAD design) in Figure 4 according to [19, 20]. Additionally, the

insert prepared by traditional powder metallurgy methods and 3D-printed structure ready for filling and the following consolidation by HIP or SPS are given in Figures 5(a)–5(c), respectively.

The first approach of reinforcement was realized by adding diamond particles into AISI 316L metal matrix prior to 3D printing of lattice. Diamond particles were covered by nickel coating (56 wt.%) to reduce diamond transformation

TABLE 1: Description of samples and SPS conditions.

Sample	Printed lattice	Filling powder	SPS conditions: temperature, pressure, sintering time
No. 1	316L-5%wt. diamond	316L	900°C, 75 MPa, 14 min
No. 2	316L-10%wt. diamond	316L	900°C, 75 MPa, 14 min
No. 3	TiN, 1.00 mm unit cell	Ti6Al4V	900°C, 75 MPa, 14 min
No. 4	TiN, 0.75 mm unit cell	Ti6Al4V	900°C, 75 MPa, 14 min
No. 5*	Without lattice	316L	1000°C, 50 MPa, 10 min
No. 6*	Without lattice	Ti6Al4V	1000°C, 50 MPa, 10 min

*5 and 6 are reference samples.

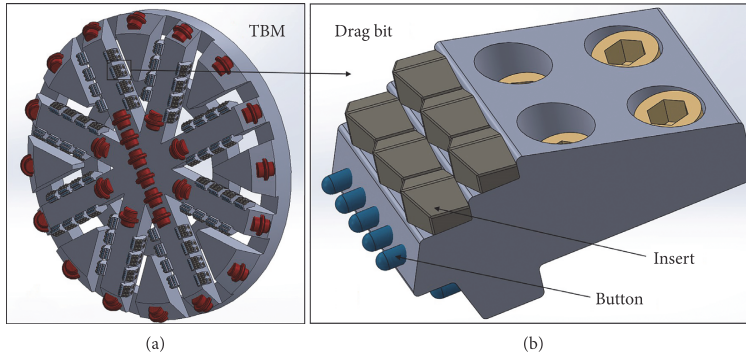


FIGURE 4: Schematic illustration of tunnel boring machine cutterhead (a), position of buttons and inserts in the drag bit (b) (TBM diameter is 3000 mm and drag bit dimension is 195 × 115 × 90 mm).

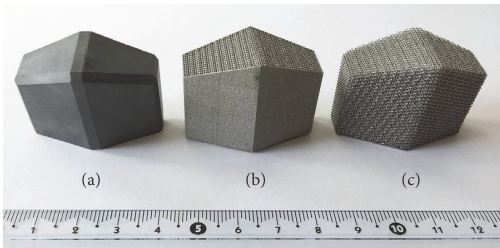


FIGURE 5: Tunnel boring machine insert produced by conventional powder metallurgy method (a), 3D printed structure for HIP (b), 3D printed structure ready for filling and following consolidation by SPS (c) (length, width and height of sample is 36 × 16 × 30 mm).

into graphite during 3D printing and sintering. Powder with 40–50 μm particle sizes was supplied by Vanmoppes & Sons Ltd. [18]. Stainless steel AISI 316L powder with $45 \pm 10 \mu\text{m}$ particle size was obtained from Sandvik Osprey Ltd. Printed lattices with varied content of diamond in the 316L matrix are shown in Figures 6(a)–6(f). Comparison of structures with 5%, 10%, and 20% of coated diamond in Figure 6 displays that increase of diamond content leads in general to higher strut diameter and lower strength of lattice structure. On the other hand, the comparison between Figures 2 (plain AISI 316L) and 6 (AISI 316L with diamond) demonstrates that sticking of unmelted original metallic particles is reduced in case of printing with higher diamond content.

The second reinforcement approach is based on the creation of a hard titanium nitride phase (layer) by nitriding

of titanium alloy lattice. Such reinforcement can provide improvement in wear and corrosion resistance of materials under study. Argon-atomized Ti6Al4V Grade 5 powders with $\leq 45 \mu\text{m}$ diameter and 4.429 gr/cm^3 density were used to print lattice structures with 30l/h argon consumption, 25 μm layer thickness, 2 mm unit cell size, and 6% volume fraction of the material. In the second step, the Ti6Al4V lattice was heated in VNF under nitrogen gas flowing with 10°C/min heating rate and 90 min holding time at the desired nitriding temperature. Digital optical photos and SEM photographs of Ti6Al4V lattice structures with 2 mm unit cell size and constant nitrogen flow and different nitriding temperatures (750°C, 900°C, and 1050°C) are shown in Figures 7 and 8, respectively. No defects (like cracks) were detected after nitriding (Figure 8). It was found that nitriding at 900°C gives sufficient thickness of the nitrided surface layer and this temperature was selected as optimal. Additionally, Ti6Al4V lattices nitrided at 900°C temperature with varied volume fractions are shown in Figure 9. After printing and nitriding, the lattice was fulfilled with Ti6Al4V powders, sintered in SPS device. Plain (unreinforced) solid Ti6Al4V reference samples were directly sintered from raw powder. Comparison between Figures 3 and 8 (before and after nitriding) shows that there are no significant changes in lattice appearance. Unmelted attached particles are also nitrided and can serve as reinforcement.

3. Results and Discussion

3.1. Results of Laboratory Testing. Two types of reinforcement approaches were proposed for improving wear

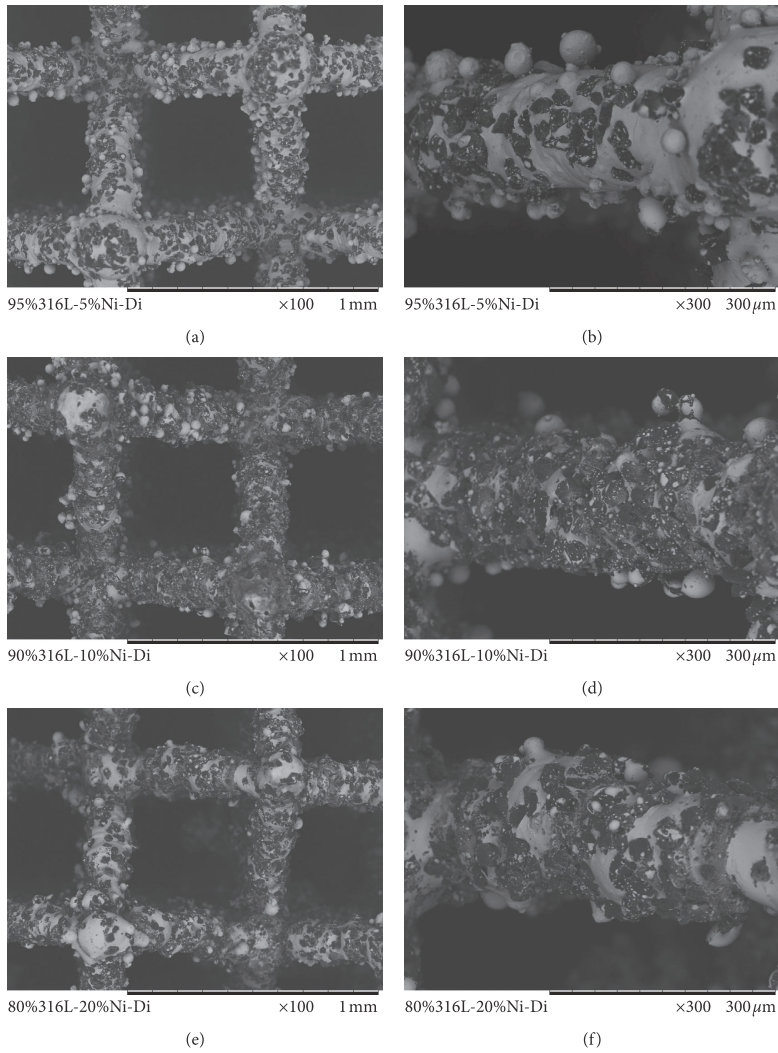


FIGURE 6: SEM images of 316L-diamond (nickel-coated) lattice.

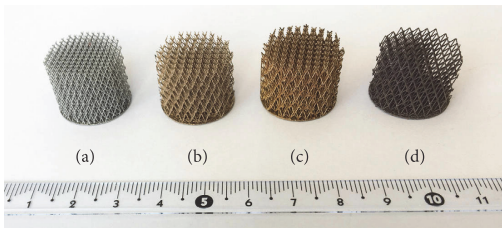


FIGURE 7: Digital photos of manufactured Ti6Al4V lattice (a) and heated and nitrided Ti6Al4V lattices at 750°C (b), 900°C (c), and 1050°C (d). Volume fraction and unit cell size are 6% and 2 mm, respectively (diameter of lattice structures is 20 mm, and length is 15 mm).

resistance and damage tolerance, namely, by diamond addition or nitriding. Possible arbitrary and/or uniform distribution of diamond particles in the metallic lattice and sample (Figure 6), finding the optimum condition for nitriding of Ti6Al4V lattice (Figure 7) and the effect of nitriding on microstructure of different metallic cell configurations (Figures 8 and 9), was introduced as novelty of recent research meant to improve wear resistance. After that, lattices were fulfilled by anticorrosive and ductile metals and sintered. Consequently, four samples have been prepared with the help of a combination of SLM and SPS techniques, and they are stated in Table 1.

Wear resistance of samples was evaluated via a custom-made patented impact-abrasive tribodevice (IATD) in

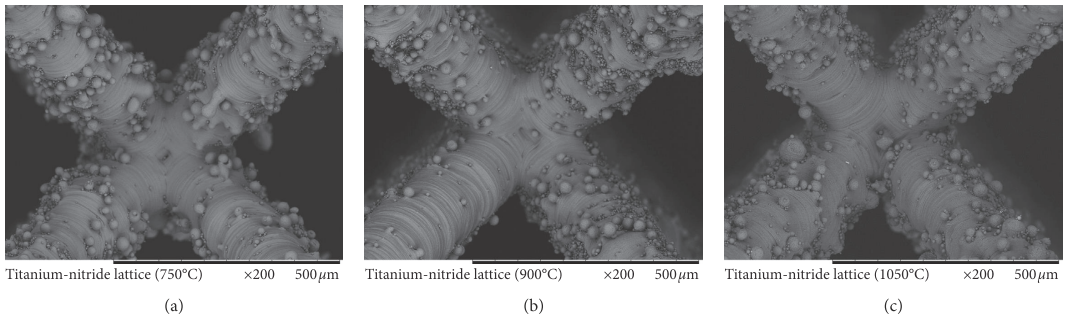


FIGURE 8: SEM images of Ti6Al4V lattices nitrided at various temperatures. Volume fraction and unit cell size are 15% and 1 mm, respectively.

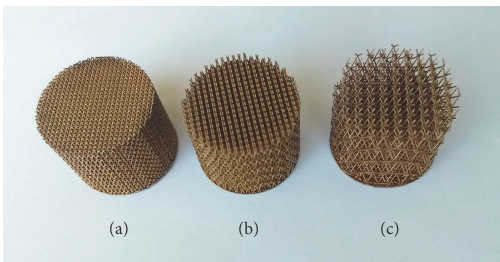


FIGURE 9: Digital optical photos of heated and nitrided Ti6Al4V lattices at 900°C with volume fraction and unit cell size of 26% and 0.75 mm (a); 16% and 1.00 mm (b); and 6% and 2.00 mm (c), respectively (diameter of lattice structures is 20 mm, and length is 15 mm).

Tallinn University of Technology [21]. Eventually, lost volume and a maximum depth of wear scar were evaluated by a *Brucker* optical surface profiler (OSP) ContourGT-K0+. Optical photographs of Sample No. 2 (as for example) after OSP assessment and also contour/perspective micrographs can be observed in Figure 10. Statistical results of lost volume as indicators of wear resistance of produced and tested materials are shown in Figure 11. The increase of coated diamond content improves the wear resistance of AISI 316L (compare Sample Nos. 1, 2, and 5). Hence, Sample No. 2 has better impact-abrasive behaviour than No. 1, and both of them are better than No. 5 (pure 316L without lattice as a benchmark). Combination of selective laser melting and spark plasma sintering has been introduced as a new approach for producing wear resistance material [22]. Hard material (diamond) coated by binder metal (nickel) filled inside cellular lattice structure (Ti6Al4V) showed anti-impact behaviour. Also, comparison between Sample Nos. 3, 4, and 6 shows that the nitriding enables improvement of wear resistance and a decrease of unit cell size (an increase of volume fraction) of Ti6Al4V-nitride lattice structure leads to higher wear resistance.

Postprocessing (nitriding or carburizing) can provide the increase in the Vickers hardness of metallic lattice structures up to 3 times [23]. Surface patterns of solid metallic structures have a significant role in controlling the friction coefficient [24]. Therefore, a cross section of

rods in both lattice structure and surface of solid structures are important in tribology. Maximum depth of wear scar of Sample No. 2 (best result obtained by the addition of coated diamond particles) demonstrated in Figure 10 was 191 μm . Such good result was obtained by applying optimal SPS conditions enabling minimization of graphitization of diamond particles in a lattice structure that can protect the matrix against abrasion. XRD pattern of sample No. 4 (best result for Ti6Al4V-nitrided lattices structure) is depicted in Figure 12, illustrating that titanium nitride is formed and can provide protection against wear.

3.2. Results of Finite Element Analysis. Two finite element models for demonstration of the benefits of the lattice-included structure of TBM machine wear-resistant components (Figure 4(b)) are simulated by SOLIDWORKS and ANSYS software. TBM drag bit insert's abrasion (scratching or sliding) (Figures 13–15) and the impact of a button (Figures 16–18) were considered. The wear resistance of the plain sample, lattice structure, and contact with abrasive particle has been modelled by finite element simulation [25]. The results show the ability of lattice to absorb energy and decrease the rising of local stresses. Solid diamond (without lattice) and diamond with Ti6Al4V lattice were compared in both cases. The first simulation includes sliding of TBM insert against the wall (steel) designed in SOLIDWORKS and is demonstrated in Figure 13(a). The steel material (as counterpart) was chosen to illustrate the behaviour in most critical conditions. The meshing of the components and defining of boundary conditions were done with the help of ANSYS workbench analyser and AUTODYN solver as it can be seen in Figure 13(b). Strut diameter of modelled lattice structure was 200 μm , and unit cell size was 1 \times 1 \times 1 mm. Sliding speed was set as 1 m/s, and distance was 1 m. Deformation and Von Mises stress distribution of pure diamond at the end of abrasion are demonstrated in Figure 14. It is possible to see that the stress exceeds that of compressive strength of diamond and pure diamond is broken in several locations while a diamond with lattice (Figure 15) experiences mainly minor deformation with some loss of extruded

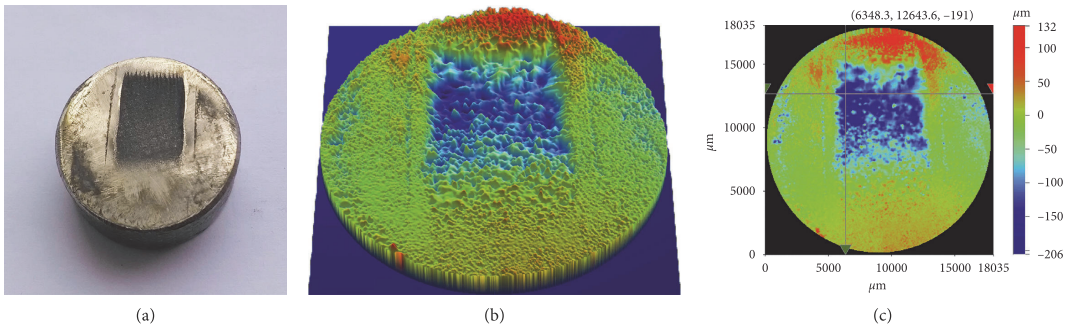


FIGURE 10: Optical image of Sample No. 2 after IATD test (a); OSP perspective micrograph (b); OSP height map micrograph (c).

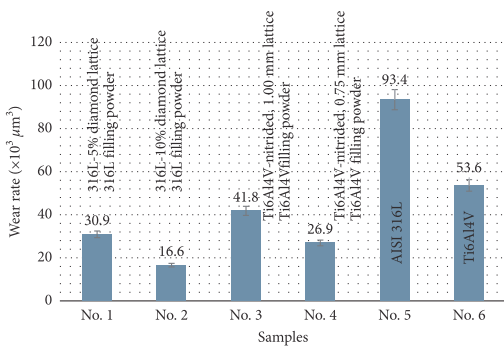


FIGURE 11: Wear rates of materials during impact-abrasive test.

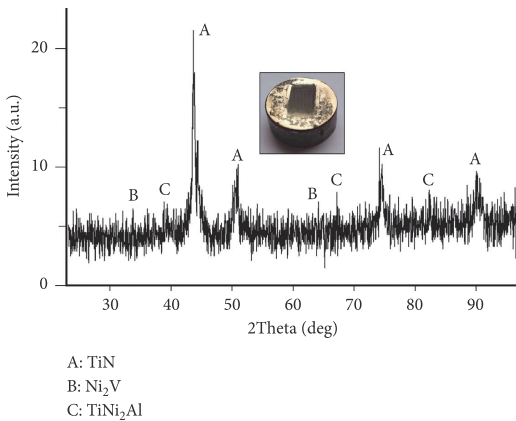
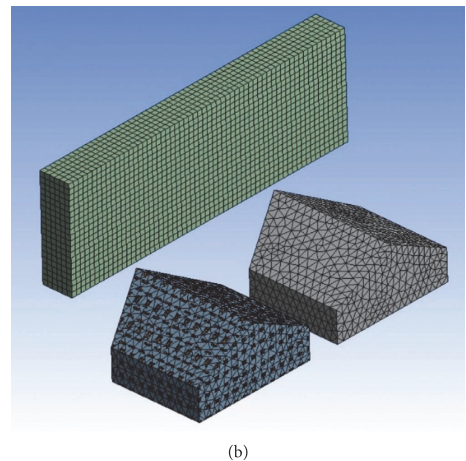
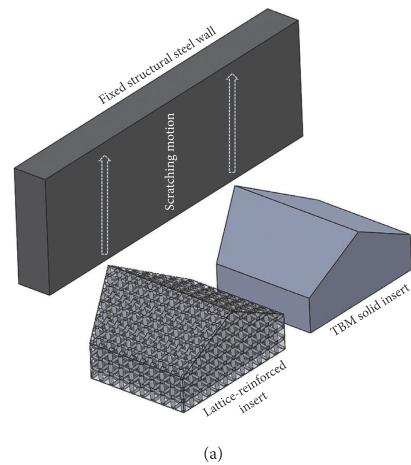


FIGURE 12: XRD pattern of Sample No. 4 (as example).

metal lattice (diamond fragments were not lost). The area of the heavily affected zone of the insert with lattice structure is smaller (Figure 15(c)).

The second simulation was performed to analyse the process of the dynamic interaction of single TBM drag bit button with big stone to show the performance of material

FIGURE 13: SOLIDWORKS design of solid diamond and diamond with lattice inserts (a); ANSYS mesh of solid and lattice-containing inserts (b).

containing lattice against impact (Figure 16). The inertia of the button (inertia of cutterhead) and that of the stone were added to bring the conditions of modelling as close as

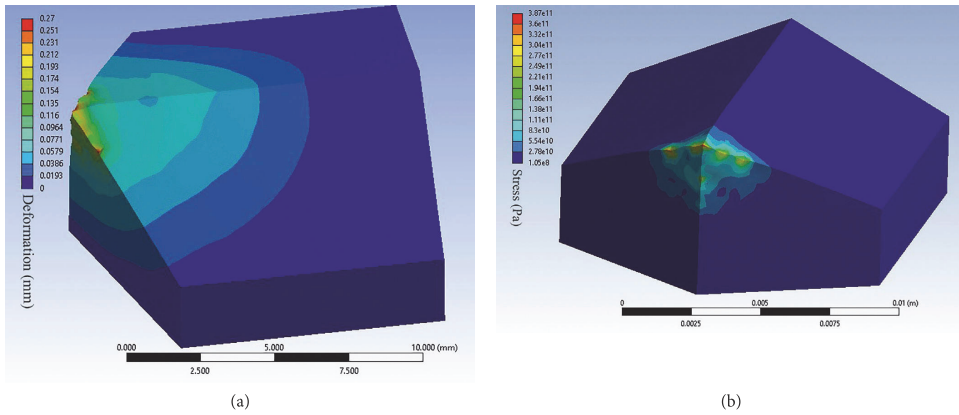


FIGURE 14: Deformation (a) and Von Mises stress distribution (b) of solid diamond insert.

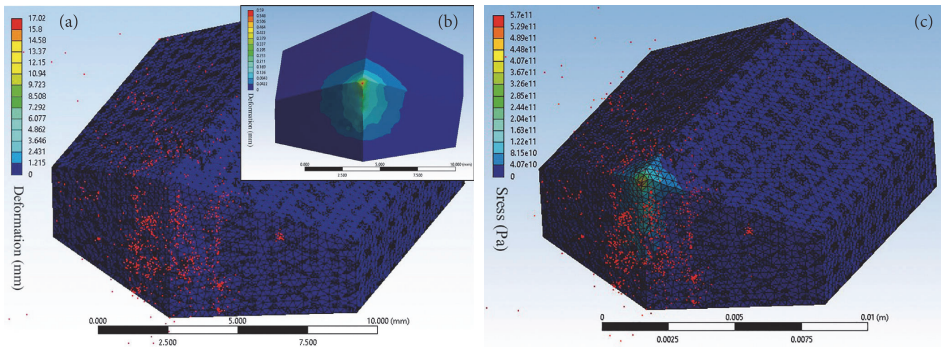


FIGURE 15: Deformation (a, b) and Von Mises stress distribution (c) of insert made of diamond with lattice. Red points of images (a) and (c) illustrate the fine particles of metal lattice that are relocated from the original position. Image B shows deformation of the material with excluded relocated particles.

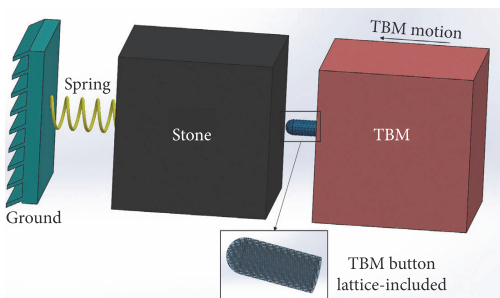


FIGURE 16: Schematic illustration of the modelling conditions of button impacting stone. The button and the stone are both modelled with inertia.

possible to the real ones. It was set that TBM button has a speed of 1 m/s while the stone was moving with a speed close to zero (0.1 mm/s). The results of deformation and Von Mises stress calculations for pure diamond and Ti6Al4V lattice-included diamond are shown in Figures 17

and 18, respectively. For pure diamond (Figure 17), deformation and stress concentration are located mainly in the tip area of a button and with a size of about 1 mm. The lattice-enhanced structure of diamond-based material transfers the deformation and stress concentration to the end of a button (Figure 18) where it is fixed to the TBM cutterhead (Figure 16) and consequently absorbs the impact intensity and increases the lifetime value of buttons. The performance of lattice during abrasion by insert and impact by button is illustrated in Figures 19(a) and 19(b), respectively. The results show that the whole lattice structure of the part is affected by abrasion or impact and helps to redistribute the stresses and increase the damage tolerance.

4. Conclusion

This study has described two novel approaches for reinforcement of the materials intended for improvement of performance in impact-abrasive conditions. Impact energy absorptive Ti6Al4V lattice along with diamond particles or

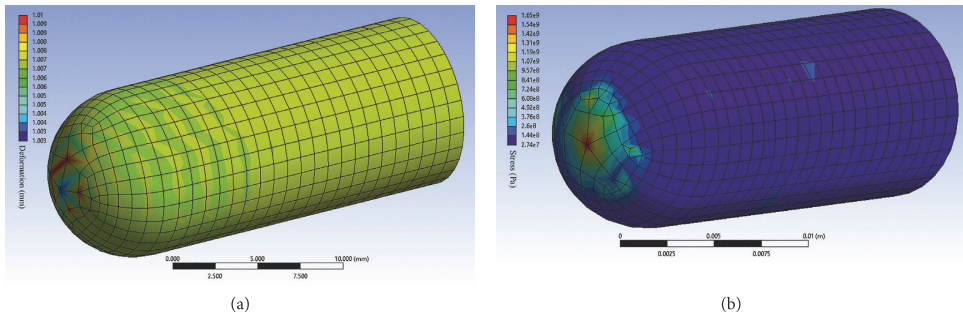


FIGURE 17: Deformation (a) and Von Mises stress distribution (b) of solid diamond TBM button.

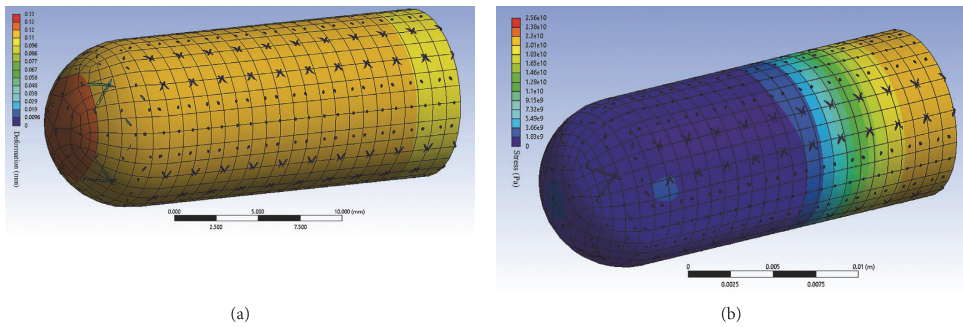


FIGURE 18: Deformation (a) and Von Mises stress distribution (b) of button made of solid diamond with Ti6Al4V lattice.

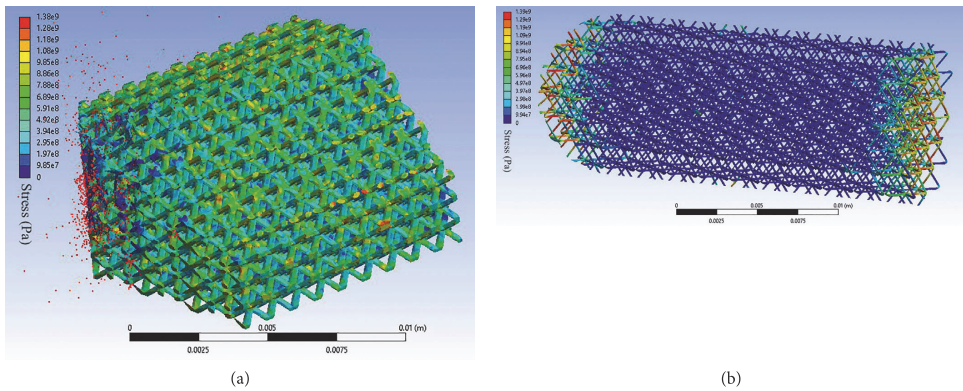


FIGURE 19: Von Mises stress distribution of lattices shown separately for the conditions of abrasion (a) and impact (b).

nitrides improving wear resistance is introduced for the production of inserts and buttons of tunnelling machine:

- (1) It was confirmed by laboratory testing that both approaches are providing up to 2.0 and 5.6 times improvement in wear resistance in impact-abrasive conditions. The reinforcement by diamond particles was providing the best improvement while

reinforcement by nitriding of the lattice was less efficient. The lattice for both approaches was printed with the help of the SLM machine and later filled with powder and consolidated by applying the SPS method.

- (2) It was shown that the combination of 3D printing of 316L-diamond lattice and SPS method has

provided uniform distribution of diamond particles. It was also found that the material with higher diamond content provides higher wear resistance.

- (3) The use of diamond particles coated by nickel and fast-sintering time during SPS process helped to reduce graphitization of diamond that was confirmed by XRD and high performance of reinforced materials.
- (4) The optimal nitriding conditions of 3D printed Ti6Al4V lattice structures (90 min at 900°C) and the unit cell size of the lattice (0.75 mm) were found.
- (5) The modelling with the help of SOLIDWORKS/ ANSYS finite element method proved that lattice structure enables to improve performance of materials in abrasive and impact conditions similar to those experienced by inserts and buttons of drag bit of soft ground TBM or those found in other applications (mining or geothermal drilling, for example).

Data Availability

The materials, techniques, machines, references, and simulation data used to support the findings of this study are included within the article.

Disclosure

The founding sponsors had no role in the design of the study; in the collection, analyses, or interpretation of data; in the writing of the manuscript, and in the decision to publish the results.

Conflicts of Interest

The authors declare that there are no conflicts of interest regarding the publication of this paper.

Authors' Contributions

Methodology, experiments, software analysis, writing, investigation, and visualization were carried out by R. R. Project administration, reviewing, editing, and supervision were performed by M. A. Printing assistance and supervision were carried out by L. K.

Acknowledgments

This research was supported by the Estonian Ministry of Education and Research (IUT 19–29 and ETAG18012); TALTECH base finance project (B56 and SS427); the personal grant of the Estonian Research Council (PUT1063); the European Regional Fund (2014-2020.4.01.16-0183) (Smart Industry Centre); and ASTRA “TALTECH Institutional Development Programme for 2016–2022” Graduate School of Functional Materials and Technologies (2014-2020.4.01.16-0032). The authors would like to thank Rainer Traksmaa for the help with preparation of XRD measurements.

References

- [1] I. Yadroitsev and I. Smurov, “Selective laser melting technology: from the single laser melted track stability to 3D parts of complex shape,” *Physics Procedia*, vol. 5, pp. 551–560, 2010.
- [2] D. Dai and D. Gu, “Thermal behavior and densification mechanism during selective laser melting of copper matrix composites: simulation and experiments,” *Materials and Design*, vol. 55, pp. 482–491, 2014.
- [3] I. Yadroitsev, P. Krakhmalev, and I. Yadroitsava, “Selective laser melting of Ti6Al4V alloy for biomedical applications: temperature monitoring and microstructural evolution,” *Journal of Alloys and Compounds*, vol. 583, pp. 404–409, 2014.
- [4] Z. Sun, X. Tan, S. B. Tor, and W. Y. Yeong, “Selective laser melting of stainless steel 316L with low porosity and high build rates,” *Materials and Design*, vol. 104, pp. 197–204, 2016.
- [5] E. Brandl, U. Heckenberger, V. Holzinger, and D. Buchbinder, “Additive manufactured AlSi10Mg samples using Selective Laser Melting (SLM): microstructure, high cycle fatigue, and fracture behavior,” *Materials and Design*, vol. 34, pp. 159–169, 2012.
- [6] H. K. Rafi, N. V. Karthik, H. Gong, T. L. Starr, and B. E. Stucker, “Microstructures and mechanical properties of Ti6Al4V parts fabricated by selective laser melting and electron beam melting,” *Journal of Materials Engineering and Performance*, vol. 22, no. 12, pp. 3872–3883, 2013.
- [7] C. Yan, L. Hao, A. Hussein, and D. Raymont, “Evaluations of cellular lattice structures manufactured using selective laser melting,” *International Journal of Machine Tools and Manufacture*, vol. 62, pp. 32–38, 2012.
- [8] M. Smith, Z. Guan, and W. J. Cantwell, “Finite element modelling of the compressive response of lattice structures manufactured using the selective laser melting technique,” *International Journal of Mechanical Sciences*, vol. 67, pp. 28–41, 2013.
- [9] A. Hussein, L. Hao, C. Yan, R. Everson, and P. Young, “Advanced lattice support structures for metal additive manufacturing,” *Journal of Materials Processing Technology*, vol. 213, no. 7, pp. 1019–1026, 2013.
- [10] C. Yan, L. Hao, A. Hussein, P. Young, and D. Raymont, “Advanced lightweight 316L stainless steel cellular lattice structures fabricated via selective laser melting,” *Materials and Design*, vol. 55, pp. 533–541, 2014.
- [11] C. Yan, L. Hao, A. Hussein, S. L. Bubb, P. Young, and D. Raymont, “Evaluation of light-weight AlSi10Mg periodic cellular lattice structures fabricated via direct metal laser sintering,” *Journal of Materials Processing Technology*, vol. 214, no. 4, pp. 856–864, 2014.
- [12] V. J. Challis, X. Xu, L. C. Zhang, A. P. Roberts, J. F. Grotowski, and T. B. Sercombe, “High specific strength and stiffness structures produced using selective laser melting,” *Materials and Design*, vol. 63, pp. 783–788, 2014.
- [13] C. Qiu, S. Yue, N. J. E. Adkins et al., “Influence of processing conditions on strut structure and compressive properties of cellular lattice structures fabricated by selective laser melting,” *Materials Science and Engineering: A*, vol. 628, pp. 188–197, 2015.
- [14] C. Yan, L. Hao, A. Hussein, P. Young, J. Huang, and W. Zhu, “Microstructure and mechanical properties of aluminium alloy cellular lattice structures manufactured by direct metal laser sintering,” *Materials Science and Engineering: A*, vol. 628, pp. 238–246, 2015.

- [15] R. Wauthle, B. Vrancken, B. Beynaerts et al., "Effects of build orientation and heat treatment on the microstructure and mechanical properties of selective laser melted Ti6Al4V lattice structures," *Additive Manufacturing*, vol. 5, pp. 77–84, 2015.
- [16] <https://www.materials.sandvik/en/>.
- [17] <http://www.tls-technik.de/>.
- [18] <http://www.vanmoppes.ch/en/>.
- [19] <http://www.nfm-technologies.com/>.
- [20] T. Camus and S. Moubarak, "Maintenance Robotics in TBM Tunnelling, ISARC," in *Proceedings of the International Symposium on Automation and Robotics in Construction*, Oulu, Finland, February 2015.
- [21] M. Antonov, R. Veinthal, D.-L. Yung, D. Katušin, and I. Hussainova, "Mapping of impact-abrasive wear performance of WC-Co cemented carbides," *Wear*, vol. 332-333, pp. 971–978, 2015.
- [22] R. Rahmani, M. Antonov, and L. Kollo, "Wear resistance of (diamond-Ni)-Ti6Al4V gradient materials prepared by combined selective laser melting and spark plasma sintering techniques," *Advances in Tribology*, vol. 2019, Article ID 5415897, 12 pages, 2019.
- [23] Y. Holovenko, L. Kollo, M. Jõelet, R. Ivanov, T. Soloviova, and R. Veinthal, "Production of metal-ceramic lattice structures by selective laser melting and carburizing or nitriding," *Proceedings of the Estonian Academy of Sciences*, vol. 68, no. 2, pp. 131–139, 2019.
- [24] Y. Holovenko, M. Antonov, L. Kollo, and I. Hussainova, "Friction studies of metal surfaces with various 3D printed patterns tested in dry sliding conditions," *Proceedings of the Institution of Mechanical Engineers, Part J: Journal of Engineering Tribology*, vol. 232, no. 1, pp. 43–53, 2018.
- [25] R. Rahmani, M. Antonov, and N. Kamboj, "Modelling of impact-abrasive wear of ceramic, metallic, and composite materials," *Proceedings of the Estonian Academy of Sciences*, vol. 68, no. 2, pp. 191–197, 2019.

Publication V

R. Rahmani; M. Antonov; L. Kollo; Wear Resistance of (Diamond-Ni)-Ti6Al4V Gradient Materials Prepared by Combined Selective Laser Melting and Spark Plasma Sintering Techniques, *Advances in Tribology* (2019) 1-12.

Research Article

Wear Resistance of (Diamond-Ni)-Ti6Al4V Gradient Materials Prepared by Combined Selective Laser Melting and Spark Plasma Sintering Techniques

Ramin Rahmani , Maksim Antonov, and Lauri Kollo

Tallinn University of Technology, Department of Mechanical and Industrial Engineering, Ehitajate tee 5, Tallinn 19086, Estonia

Correspondence should be addressed to Ramin Rahmani; ramin.rahmaniahranjani@ttu.ee

Received 11 September 2018; Revised 15 January 2019; Accepted 21 February 2019; Published 4 March 2019

Guest Editor: Mikael Olsson

Copyright © 2019 Ramin Rahmani et al. This is an open access article distributed under the Creative Commons Attribution License, which permits unrestricted use, distribution, and reproduction in any medium, provided the original work is properly cited.

An approach of sintering 3D metal printed lattices and diamond nickel-coated particles is proposed which can be used for the production of tunnel boring machine (TBM) cutters and mining equipment blades. Nickel-coated diamond particles are mixed with titanium powder and incorporated into a lightweight Ti6Al4V (3D printed) lattice with the help of spark plasma sintering (SPS) method. Effect of Ti6Al4V lattices size, diamond particles size, and nickel coating layer thickness on wear resistance of composites is discussed. Functionally graded lattice (FGL) structures were produced by selective laser melting (SLM) method, representing an increasingly growing additive manufacturing engineering area introduced in material engineering. Impact-abrasive tribo-device (IATD), scanning electron microscopy (SEM), X-ray diffraction (XRD), energy-dispersive spectroscopy (EDS), and optical surface profiler (OSP) were used to characterize samples. An ab initio design of diamond-metal composite is based on the improvement of impact and abrasive wear resistance of Ti6Al4V by adding diamond particles and by applying of gradient lattice structure. The specimen with larger size of the diamond particle and thicker Ni coating has better wear resistance. In addition, ANSYS software simulations were done to analyze the effect of the presence of 3D printed lattice via nonlinear finite element AUTODYN solver under impact test. Diamond-based gradient composite material produced by combined SLM-SPS methods can be applied in applications where resistance against impact-abrasive wear is important.

1. Introduction

Ti6Al4V is the most applicable titanium alloy that has been extremely used in biomedicine, osteology, aerospace, marine, and additive manufacturing industries due to low density and high mechanical properties. Adding ≈ 6.75 wt. % of aluminum and ≈ 4.5 wt. % of vanadium to titanium makes it more applicable than pure titanium for corrosive wear resistance applications. Additive manufactured titanium alloys have motivated in deep *in vivo* corrosion research for recovering fractures of knee and hip bones [1]. It was recently demonstrated that 3D printed materials can provide improved tribological performance (lower coefficient of friction, stable performance) in sliding conditions [2]. Diamond is the hardest known, expensive, valuable, and versatile material for several industries. Synthetic polycrystalline diamond (PCD) is cost-effective and advantageous powder that can be coated by metals like cobalt, nickel, titanium, and

copper and is usually used in grinding, polishing, and boring applications with sufficient cooling and without impacts. Diamond-containing metal matrix composites (MMCs) are made with the help of chemical/physical vapor deposition (CVD/PVD) techniques and they are considered because of their high thermal conductivity and mechanical properties [3]. Selective laser melting/sintering (SLM/SLS) is one of the new additive manufacturing techniques that is applied for production of complex metal shapes, lattice structures, and rapid prototyping. The SLM ability of creation lightweight metallic cellular structure with different unit cell structure, strut, and pore sizes is used as a more efficient approach to antishock/impact energy absorption, lightweight aerospace structure, electrothermal conductivity, fracture toughness enhancement, and acoustic insulation application [4, 5]. AISI 316L stainless steel, Ti6Al4V titanium, and AlSi10Mg aluminum are three highly demanded metal lattice structures due to high strength to weight ratio. Nowadays, Spark

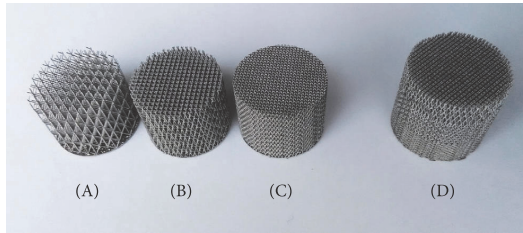


FIGURE 1: (A) Low, (B) average, (C) high volume fraction lattice structures, and (D) functionally graded lattice (FGL) structure used in the current research for samples No. 5 and No. 6 exclusively (diameter of lattice structures are 20 mm).

plasma sintering (SPS) is extensively used method based on pulsed DC electric current, high heating rates, programmable isostatic pressures, and short heating/cooling times [6]. The SPS process enables higher heating rate and sintering at lower temperature to provide consolidation of wide range of material including metals, ceramics, and cermets that is its main important advantage over conventional powder metallurgy techniques [7]. Phase degradation is almost avoided during SPS sintering. Pulsed electric current passes through a mold and conductive particles of material to be sintered. Based on pressure and temperature, it is possible to use graphite or tungsten mold and different diameter or thickness to realize desired production shape that is a suitable option in several industries. Temperature and pressure can be controlled by pyrometer/thermocouple and upper/lower punch electrode pushing force in a vacuum chamber, respectively. To avoid either graphitization of diamond or metal-coating surface oxidation, simultaneous increasing of temperature and pressure is required in SPS. Shrinkage of the powder, limited grain growth, and near-theoretical densification take place during sintering. Cellular lattice structure should be adjusted to take into account the shrinkage. The SLM parameters like cell size, lattice layer thickness, and laser current are important for the performance of the final material in test and field conditions. SLM method has been applied in recent study due to production possibility of metallic matrix in desired shapes (for example in SPS mold size or drag bits of tunneling machines) and possibility to fill spaces between the lattice rods with hard material particles (for example, diamond, cubic boron nitride, or WC-Co).

The main aims of this research were focused to optimize the composition of nickel-coated diamond and titanium powders for materials with and without titanium functionally graded lattice (FGL) structure to provide sufficient resistance against impacts and to improve abrasive wear resistance. FGL is a progressive multilayer lattice structure with different volume fraction section in longitudinal or circumferential directions so that the sections stand on each other or are embedded, respectively. Another novelty of current research is the combination of SLM and SPS methods to produce a new generation of multicomponent structures that can be used similarly to hard metals in various applications where wear resistance is of high importance. In this study, the influence of diamond particle and lattice cell sizes along with SPS parameters (temperature, pressure, and time) on tribological

results is discussed. Samples were evaluated by combined impact-abrasive tribo-device (IATD), volumetric wear was measured with the help of optical surface profiler (OSP) analyzer, and composition of obtained materials was analyzed by X-ray diffraction (XRD) method.

2. Experimental Materials and Test Methods

Cellular lattice structures were fabricated from argon atomized Ti6Al4V Gd5 powders with size $\leq 45 \mu\text{m}$ and density 4429 kg/m^3 supplied by *TLs Technik GmbH*, Germany. Polycrystalline diamond powder with 30 and 56 wt. % of nickel coating and fractions of 6-12, 20-30, and 40-50 μm were supplied by *Van Moppes & Sons Ltd.*, Swiss. Nickel coating usually contains 8-12 % of phosphorous and has 1455°C melting point (according to powder producer [8]). *Realizer SLM50* 3D metal printer machine (construction volume has a diameter of 70 mm and height of 80 mm, the thickness of layer was 20-50 μm , and argon consumption was 30 l/h) was used for preparing low, average, and high volume fraction (VF) Ti6Al4V lattices and FGL structures shown in Figure 1. Circumferential to longitudinal (C:L) cell size proportion for cylindrical lattices (Figures 1(A)–1(C)) with a diameter of 20 mm and initial height of 18 mm (final height of ≈ 10 -12 mm) were 1:2 due to significant vertical shrinkage during SPS process. It was decided that final C:L and VF for lattice shown in Figures 1(A), 1(B), and 1(C) were 2:4 and 6 %, 1:2 and 15 %, and 0.75:1.5 and 24%, respectively. FGL structure (Figure 1(D)) is composed of three equal parts as a novel applicable lattice with 20 mm diameter and 18 mm initial height of sections with 1:1, 1:2, and 1:3 C:L proportion. The schematic of the desired FGL structure obtained by combined SLM and SPS is given in Figure 2. From bottom to top, reduction of Ti6Al4V lattice structure and enhancement of diamond particles before SPSing has been shown (Figure 2). Three most important parameters for printing of Ti6Al4V lattices by SLM method were set as follows: (1) laser current (LC=3000 mA, 72 W power), (2) exposure time (ET=600 μs), and (3) point distance (PD=1 μm). In addition, these parameters for solid parts (for example, 0.1 mm thick spacer between support and lattice) were as follows: LC=2500 mA, ET=25 μs , and PD=25 μm . The thickness of every layer was 25 μm and argon was applied as a protective gas during a process inside the printing chamber.

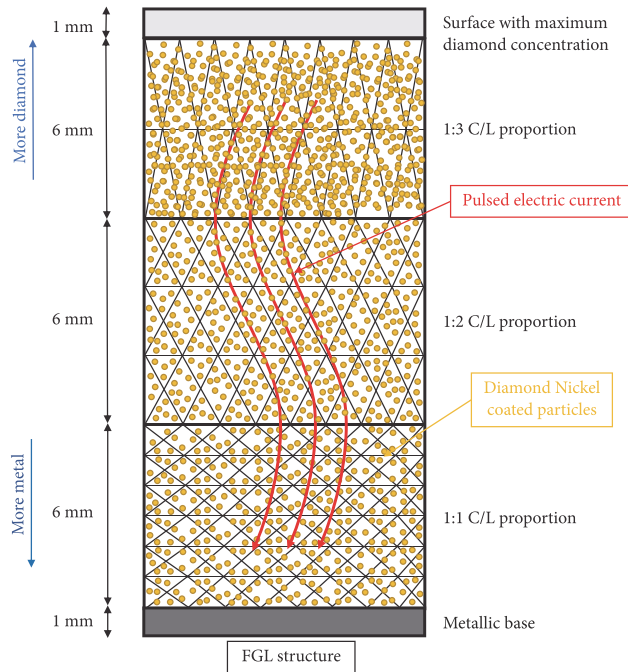


FIGURE 2: Schematic of material with FGL structure (during preparation before SPSing).

TABLE 1: Composition of samples and SPS sintering conditions.

Sample	Composition, wt. %	Diamond grain size, μm	Extent of Ni coating on D particle, wt. % [8]	Sintering pressure, MPa	Duration of sintering, min
1	29D-37Ni-34TA	40-50	56	50	9
2	29D-37Ni-34TA	6-12	56	100	6
3	29D-13Ni-58TA	40-50	30	50	9
4	29D-13Ni-58TA	20-30	30	100	6
5	26D-32Ni-24TA-18L	6-12	56	100	6
6	26D-11Ni-45TA-18L	20-30	30	100	6
7	100TA	Not-included	Not-included	50	10

- Preheating was performed at 260°C, 10 MPa and 6 Min. Sintering was done at 860°C for samples No. 1-6 and 1000°C for No. 7.

- D=diamond, TA= Ti6Al4V titanium alloy powder, and L is added in case of Ti6Al4V lattice.

- For No. 5 and No. 6, the average composition is stated due to gradient configuration.

In order to assess the influence of diamond particles size, nickel coating percentage (coating thickness), and lattice parameters, six samples were produced and are described in Table 1. The samples were designed so that each pair of samples can be compared to trace some specific effect. Sample No. 2 had finer diamond particles size than No. 1; heating/sintering time was shorter and the pressure was higher for sample No. 2 to reduce the risk of graphite formation. A similar effect can be studied with the help of samples No. 3 and No. 4 while these two samples were having thinner Ni coating on diamond particles that allows

tracing this effect as well. Samples No. 1-4 and No. 7 were lattice-free, whereas lattice-included No. 5 and No. 6 had similar composition (diamond grain size and nickel coating thickness) and sintering conditions as No. 2 and No. 4, respectively (Table 1). In order to provide similar diamond particle content in composite materials of No. 5 and No. 6 with Ti6Al4V lattice structure, the titanium powder content was reduced during SPS (Table 1).

The sintering device that was used for consolidation of nickel-coated diamond particles with titanium lattice structures was made by FCT Systeme GmbH. Such a device

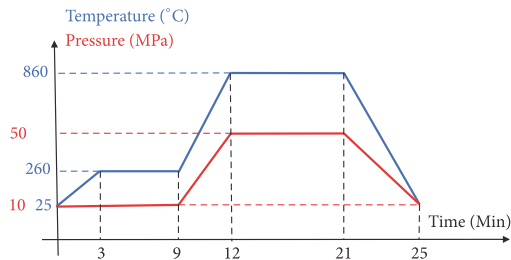


FIGURE 3: SPS conditions.

can enable 1000°C/min heating rate and 100 MPa (32 kN force for 20 mm diameter mold) pressure for samples. The machine is installed into glovebox form *MBRAUN Systeme GmbH* to perform all powder charging and weighting operations in a nitrogen atmosphere (to avoid their oxidation). Exemplary SPS sequence for sample No. 1 is presented in Figure 3. The main challenge regarding diamond particles incorporation into composites with a metallic or ceramic matrix with high melting temperature is discussed in the literature as graphitization phenomena [9]. In order to prevent graphitization, the SPS temperature of diamond-containing samples was kept below 900°C. However, some graphitization is not a major problem [10]. In order to remove the possible presence of water or hydrogen, the powders were preheated to 260°C and hold at 10 MPa pressure as it is shown in Figure 3. It was experimentally proved that such a step is improving consolidation and resulting in a lower level of graphitization and better properties (porosity, strength, and hardness) of the final composite material. Most important differences of SPS rather than conventional powder metallurgy techniques were fast heating, fast cooling, and simultaneous application of pressure and temperature. The increase in temperature to 860°C and pressure up to 50 MPa (Figure 3) enabled achieving high densification level (> 98 %).

The combined impact-abrasive wear tribo-device [11] was applied to test samples, with impact energy of 5.6 J and frequency of impacts being 27.5 Hz provided by impact generator (industrial hammer drill from Makita). The sample was experiencing reciprocative movement and was pressed (by the dead-weight system) against the rotating wheel (made from WC-Co) with a force of 49 N; linear abrasion velocity was 1 m/s. Ottawa sand (same as used in ASTM G65 standard [12]) was serving as abrasive. The particle size was 0.2-0.3 mm and feeding rate was the same as used during ASTM G65 test. The abrasive was supplied from a hopper through the pipe and nozzle into the contact region between wheel and sample. The duration of the test was 5 minutes corresponding to 300 m of sliding distance. The surface of the samples was cleaned by low angle incidence alumina particles jet after SPSing for SEM imaging. The observational study and characterization of samples were performed with the help of a Hitachi TM-1000 Scanning electron microscopy (SEM), 3D optical surface profiler (OSP) Contour GT-K0+ from Bruker, and X-ray diffraction (XRD) analyzer Bruker AXS D5005 equipped with Cu-K α radiation. In addition, elements distribution in wear-tested region was mapped by energy-dispersive spectroscopy

(EDS) Zeiss EVO MA15 with INCA Energy 350 X-ray micro-analyser.

3. Results and Discussions

SEM images of nickel-coated diamond particles are shown in Figure 4. Nickel as a ductile transition metal was used as a binder metal is produced and tested metal matrix composite. Use of nickel-coated diamond particles was preferable in comparison with pure polycrystalline diamond due to resulting higher homogeneity of distribution of diamond in composite after sintering (Figure 5). Theoretically, Ti6Al4V FGL solid continuous cellular structure during SPS process should facilitate uniform heating due to its better electrical conductivity than the set of powder particles. It was tested and it can be suggested to keep maximum temperature of SPS procedure less than 900°C to avoid melting and escape of nickel from the gaps of the mold [13]. However, the volume of added nickel powder must be adjusted according to the requirements of the specific application. In this research, the content of Ni was varying between 11 and 37 wt. % due to variation in the thickness of Ni coating around diamond particles. Higher Ni content provides better sintering and densification for diamond particles.

In the SEM images (Figure 5) the dark diamond particles are visible. In Figures 5(a)–5(c) the difference of particles size is well seen and the homogeneity of distribution is acceptable. Sample No. 4 shown in Figure 5(d) has a less homogeneous distribution of diamond particles but the appearance of the surface of the samples can be influenced by its preparation (polishing) procedure before imaging. In addition, SEM micrograph of lattice structure in sample No. 6 is shown in Figure 6 after SPS and after IATD test. EDS color mapping (Figure 6(c)) shows distribution of elements. A random spectrum in tested area was chosen to define elements distribution. EDS elemental mapping results showed C 59.91 %, Ti 28.28 %, Ni 7.32 %, Al 1.87 %, V 1.34 %, P 0.79 %, Sn 0.36 %, and Si 0.13 % (all results in weight percentage).

XRD diffraction pattern (Figure 7) of sample No. 1 shows that material has diamond remained after the SPS process. There is also the minor presence of graphite that was either formed due to graphitization of diamond or appeared due to sintering in a graphite mold. There is also the minor content of new phases formed during SPS as result of reacting of initial components, namely, TiC and Al₂O₃, that are favorable for increasing of wear resistance of the composite material.

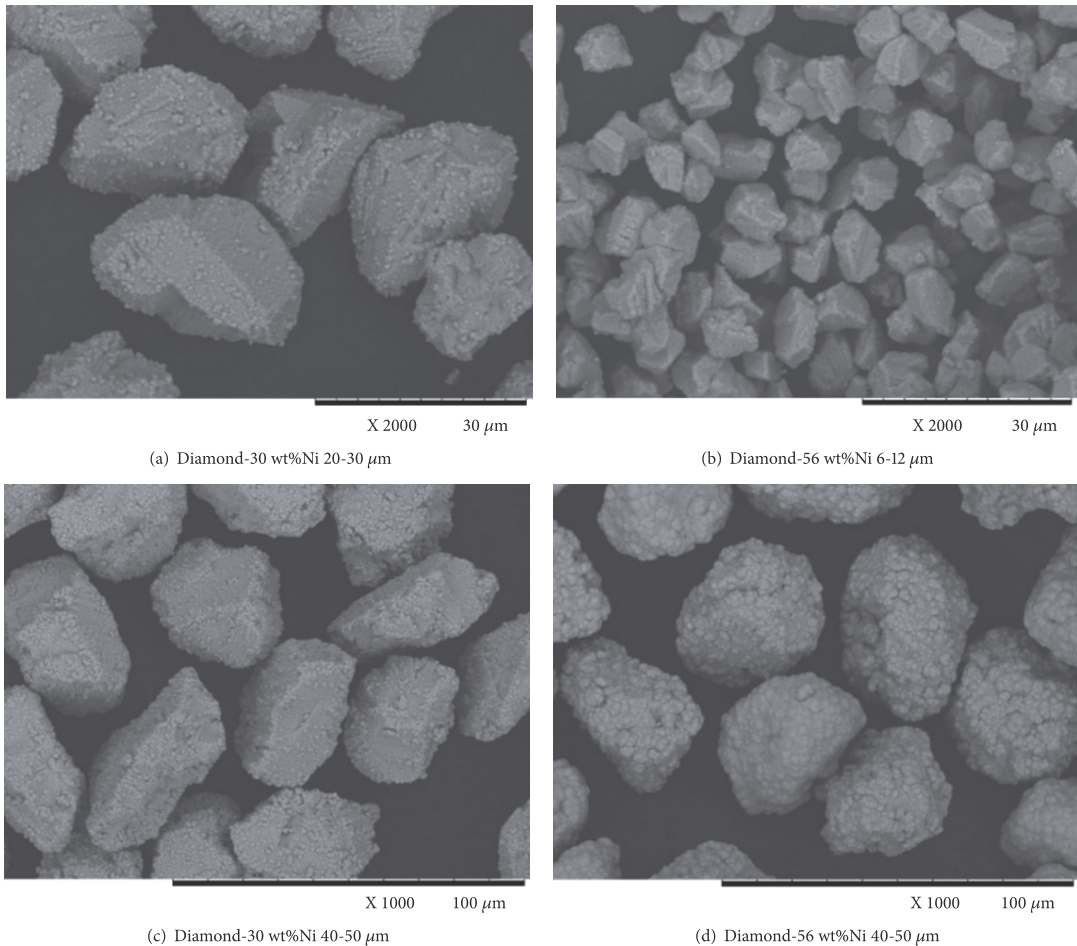


FIGURE 4: SEM micrographs of nickel-coated diamond particles.

3D OSP was applied for surface scanning of samples and the profile of the area with a diameter of 17 mm around the tested area was obtained and analyzed by software to calculate the missing volume. In a photograph after IATD test, 3D OSP results of sample No. 1 (top and perspective views) are given in Figure 8. In order to illustrate the severity of the damage, it is possible to indicate that the maximum depth of the wear scar of sample No. 1 (29D-37Ni-34TA, 40-50 μm diamond grain size) was $\approx 300 \mu\text{m}$. The red region shows intact zone while the blue zone was produced by sand particles passing between the wheel and sample during the IATD test. The results of wear rate measurements are shown in Figure 9. The IATD tests were repeated three times and results averaged. The best performer among the samples without lattice in impact-abrasive conditions was samples No. 1 and No. 2 (29D-37Ni-34TA, 6-12 μm diamond grain size) (if missing volume of material is considered). The sample No.

6 (26D-11Ni-45TA-18L, 20-30 μm diamond grain size) has illustrated better resistance than No. 5 (26D-32Ni-24TA-18L, 6-12 μm diamond grain size) among the samples with a lattice that is also shown in Figure 9. The best material (No. 1) had the largest size of diamond particles and the thickest Ni layer covering them. Material No. 3 (29D-13Ni-58TA, 40-50 μm diamond grain size) was also better due to larger diamond particle size (if compared to No.4 (29D-13Ni-58TA, 20-30 μm diamond grain size)). The same was valid for materials with lattice when No. 6 was better than No. 5. It could be concluded that, in case of materials with lattice, the size of diamond particles was more favorable than the thickness of Ni layer since No. 5 had thicker layer than No. 6.

In aggressive impact-abrasive conditions applied during the current test, the soft material No. 7 composed of pure titanium alloy had better resistance than No. 3 and No. 4. However, materials No. 5 and No. 6 with lattice were

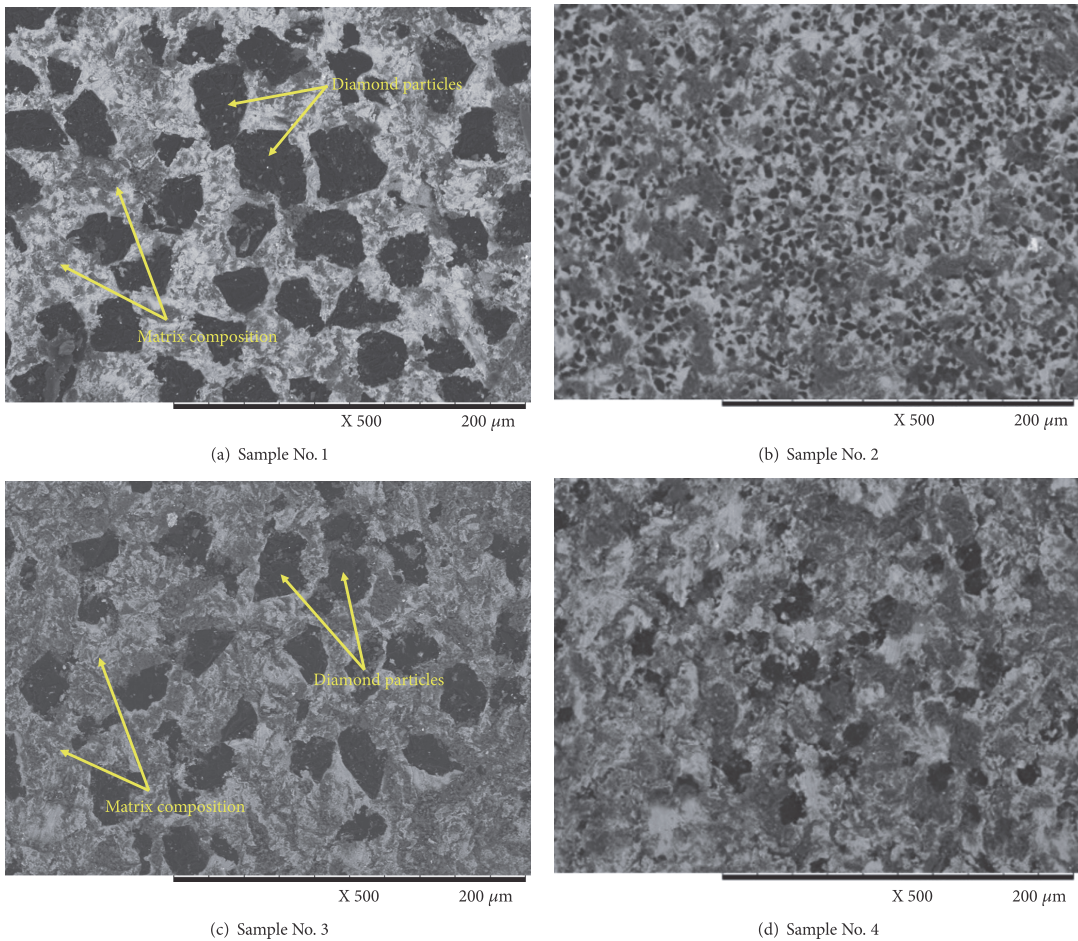


FIGURE 5: SEM micrograph of samples 1-4 after SPSing and cleaning by alumina particles jet.

having better wear resistance (than No. 7) in such impact-abrasive conditions and it is expected that in conditions with lower intensity or less frequent occurrences of impacts (typical for soft ground TBM applications) these materials will have significantly better wear resistance due to presence of diamond particles having extremely high resistance against abrasion.

The comparison between material No. 2 and No. 5 and between No. 4 and No. 6 provides the information about the effect of lattice on wear resistance. It is possible to conclude that in case of fine ($6\text{--}12\ \mu\text{m}$) diamond particles (No. 2 versus No. 5) the addition of lattice is not favorable while in case of average ($20\text{--}30\ \mu\text{m}$) size of diamond particles the use of lattice (No. 4 versus No. 6) provides significant improvement of wear resistance of the composite material. The composite material with a large size of diamond particles should be investigated in future since it should provide the best resistance in impact-abrasive conditions.

An important outcome of this study was to demonstrate the effect of diamond particle size, the thickness of the Ni coating, and the effect of metallic lattice structure on wear resistance. This was proved by XRD and by SEM images that diamond particles are present after the SPS process and after wear testing (Figures 5, 6, and 7). Various shapes of FGL structures can be produced by 3D printing and suitable SPS molds can be done in required shapes to develop required composite materials for industrial applications, i.e., wear resistant parts for mining or soft ground tunnel boring machines.

An advantage of FGL structure is that it is having more metal in bottom of sample for better connection of components (for example, insert to drag bit in TBM by bolting [14]), better absorption of impact due to increased ductility and gradual change of composition from prevailing very brittle diamond to prevailing ductile metal. High diamond

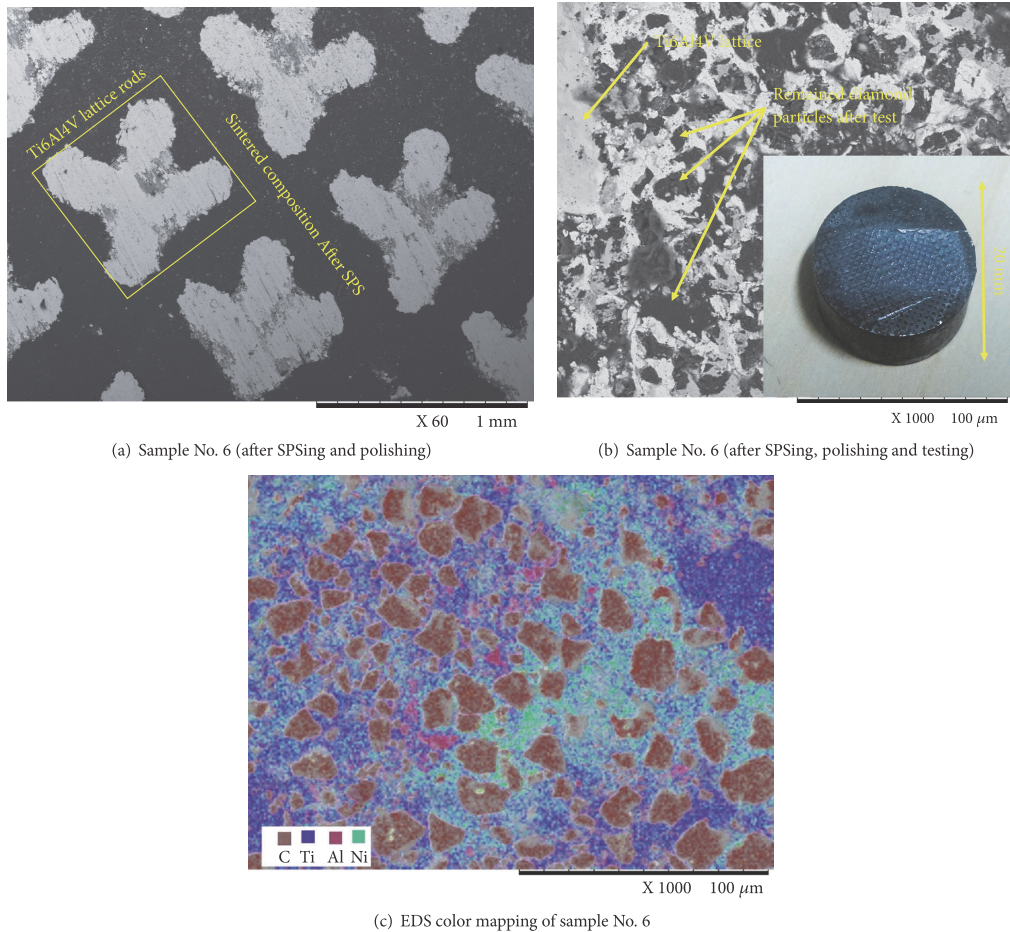


FIGURE 6: SEM micrograph of sample No. 6 (a) after SPS and (b) after impact-abrasive test (c) EDS color mapping.

content in top layer provides extreme hardness and higher wear resistant.

Consequently, combinability of SLM and SPS techniques has enabled the creation of composites focused on the diversity of lattice structures, foreseeing all kind of possible future improvements in design and cost, by adjusting the fraction of desired phases to provide further improvement in hardness, fracture toughness, and corrosive behavior.

4. Simulation Study

In order to analyze the performance of the lattice structure, an impact test has been simulated using SOLIDWORKS design, ANSYS software, and AUTODYN solver. The first sample was simulated as made from solid diamond while the second one was simulated as being made from a metallic lattice with diamond located between the elements of the lattice. The wheel of the device was simulated as being made

from WC-Co cemented carbide and the lattice structure was modeled as a Ti6Al4V nonlinear finite element, respectively (Figure 10). Samples diameter was set as 20 mm and thickness as 10 mm. The simulation performed for material without lattice is shown in Figure 11. The second simulated sample having a $2 \times 2 \times 2$ mm lattice scaffold is illustrated in Figure 12. During normal operation of the tribo-device (Figure 10(c)) [11] both rotation of the wheel (abrasive action) and impact between the sample and the wheel are provided but for current simulation, it was important to demonstrate the extreme case with impacting only (Figure 10(a)). The position of impacting was also changed. During the normal operation, the contact spot is located in the center of the sample while during the simulation the center of the impact spot was located exactly at the bottom edge of the sample to provide the most unfavorable leading resulting in brittle chipping or fracturing. The wheel was impacting the sample with the energy of 1000 and 5000 Joules (corresponding to different

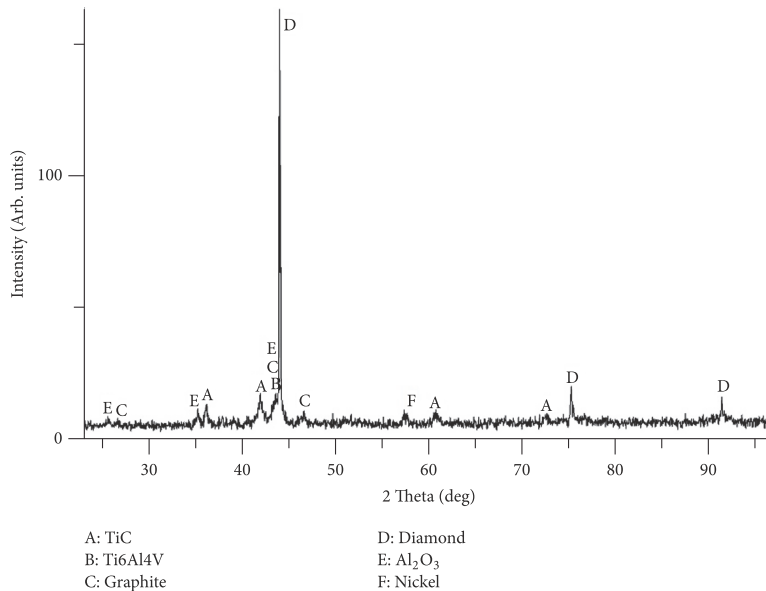


FIGURE 7: An exemplary XRD diffraction pattern of sample No. 1 before wear testing.

velocities of the wheel); the analysis time and other boundary conditions were equal for both tests (with or without lattice). The von Mises equivalent stress comparison between samples without and with lattice structure is shown in Figures 11 and 12 for low and high impact energy. According to the results of both simulations (Figures 11 and 12), it is possible to say that in case of low impact energy the maximum Von Mises stresses are approximately ten times higher in case of pure diamond material than in case of a composite material with metallic lattice and diamond reinforcing particles. In case of high-energy impact, the pure diamond sample experienced fracturing and resulting extreme displacement of contact surface up to $\approx 3700 \mu\text{m}$, while the composite material had only plastic deformation. Nonlinear finite element high-velocity contact modeling of sample's edge is a proper approach to evaluate energy absorption of materials [15]. The ability of impact energy absorption has grown up significantly with the addition of lattice structure as shown in Figure 13.

5. Conclusions

The present study is an attempt to introduce a new approach toward the production of wear resistant materials by the combination of selective laser melting and spark plasma sintering. The current work seeks to address the following results.

(1) The combined approach for the production of composite materials by the 3D printing of lattice (SLM) and sintering/consolidating (SPS) to incorporate metal-coated diamond particles has been described. It was concluded that it could be used for the production of soft ground TBM or mining parts.

(2) According to the results of wear testing in impact-abrasive conditions, either the larger size of the diamond particle or thicker Ni coating of diamond is favorable due to the reduction of the possibility of graphitization. The size of the diamond particles was found to have the strongest effect due to the harder removal of large diamond particles during the impact-abrasive process.

(3) Work on the creation of functionally graded lattice (FGL) composites is still in progress. It was found that diamond particles with larger size and thicker coating are more favorable for such materials. FGL structure provides the gradient change of metallic lattice extent from 0 % to 100 % that improves the resistance of such materials against impacts, allows predefining location of metallic phase responsible for ductility, and can enable fixation of such materials by welding or by bolting that is impossible for ceramics or other ultrahard materials.

(4) Finite element analysis was applied to illustrate benefits of lattice structure. Lattice-included material showed better response (stress, deformation, impact energy absorption, and the possibility of plastic deformation) than plain hard material against impact.

Data Availability

The materials, techniques, machines, references, and simulation data used to support the findings of this study are included within the article.

Conflicts of Interest

The authors declare that there are no conflicts of interest regarding the publication of this paper. The founding

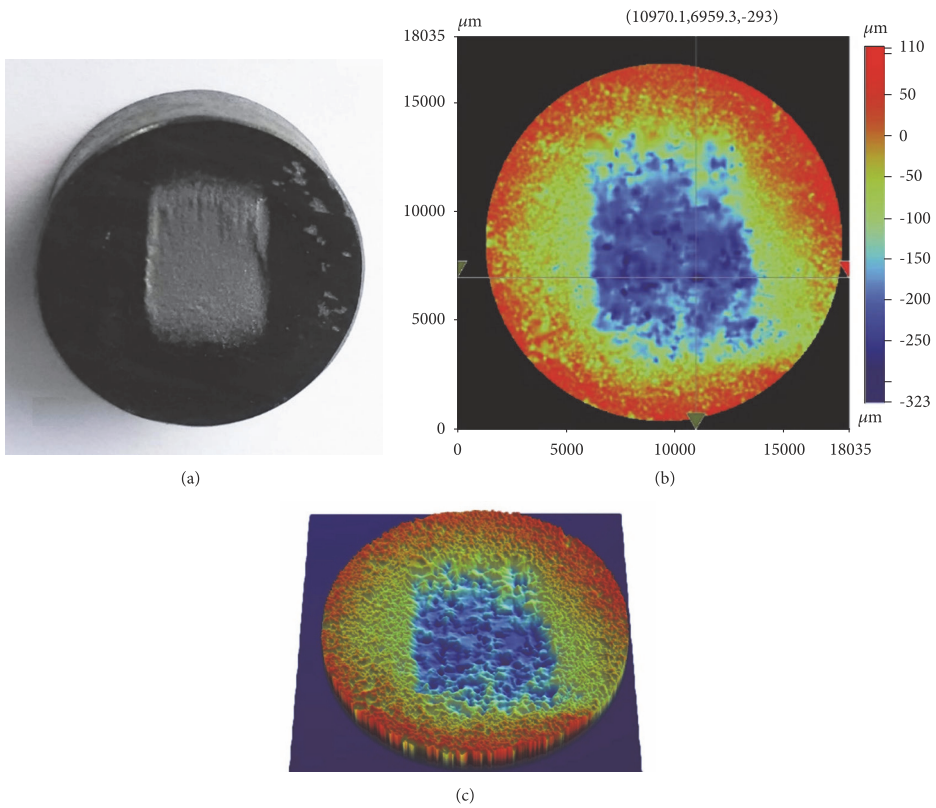


FIGURE 8: Sample No.1 after impact-abrasive test (a) photograph, (b) 3D OSP contour micrograph, and (c) 3D OSP perspective micrograph.

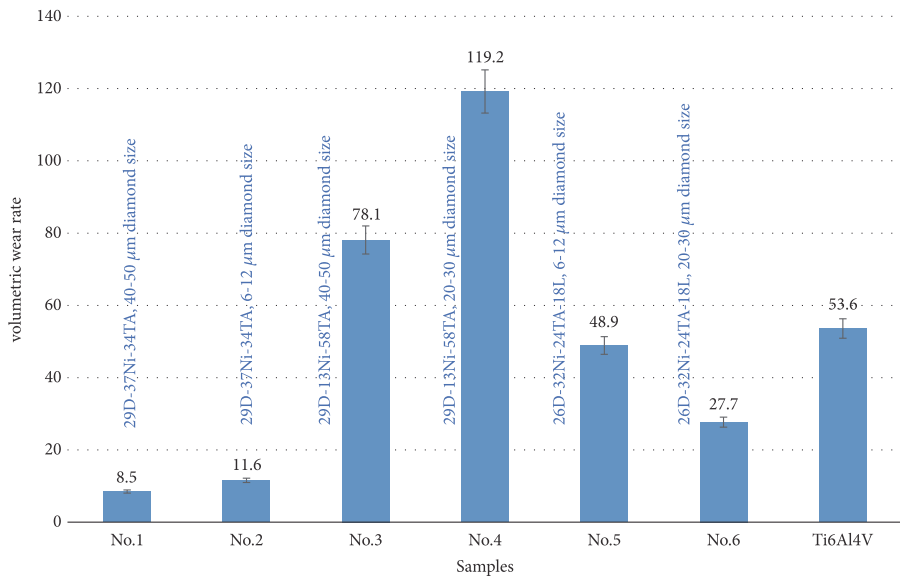


FIGURE 9: Volumetric wear rate (missing volume) of samples during impact-abrasive test measured by 3D OSP, $\times 10^3 \mu\text{m}^3$.

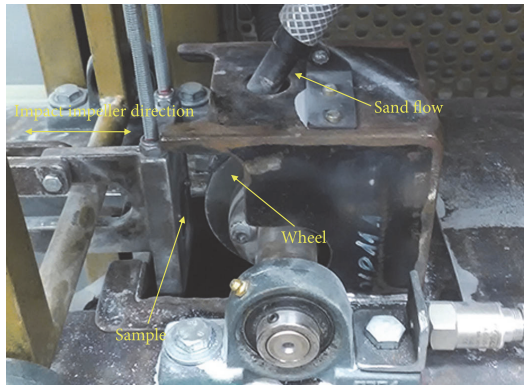
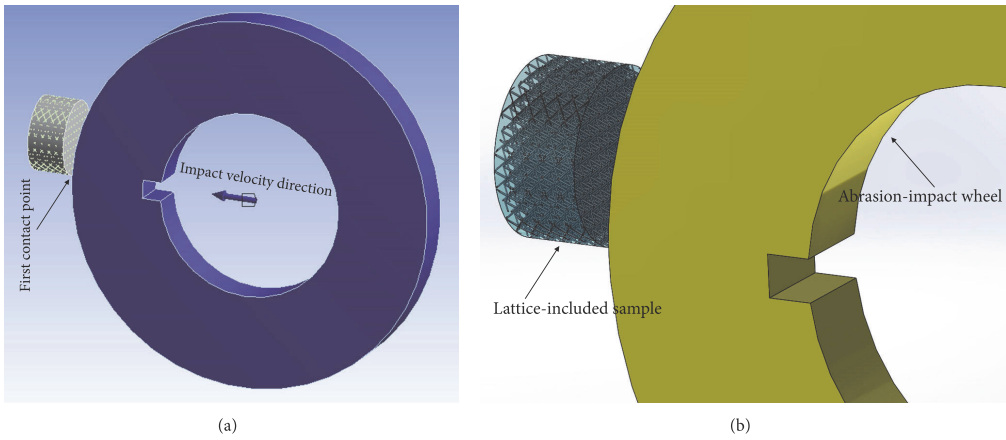


FIGURE 10: (a) Simulation mechanism, only horizontal impact motion, (b) schematic of wheel and lattice-included sample, and (c) position of sample and wheel in tribo-device laboratory [11].

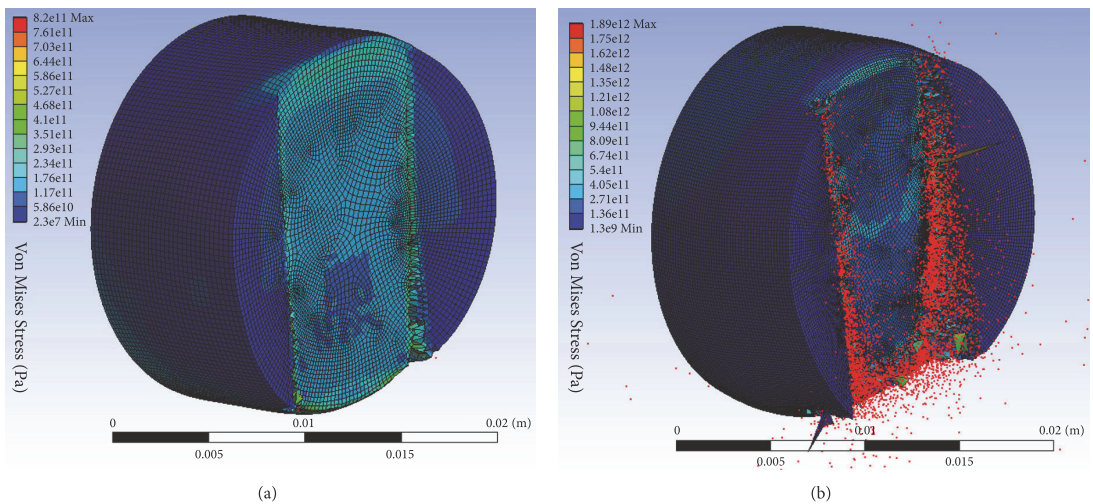


FIGURE 11: Stresses resulting from impact simulation of pure diamond sample without lattice: (a) 1000 J and (b) 5000 J impact energy.

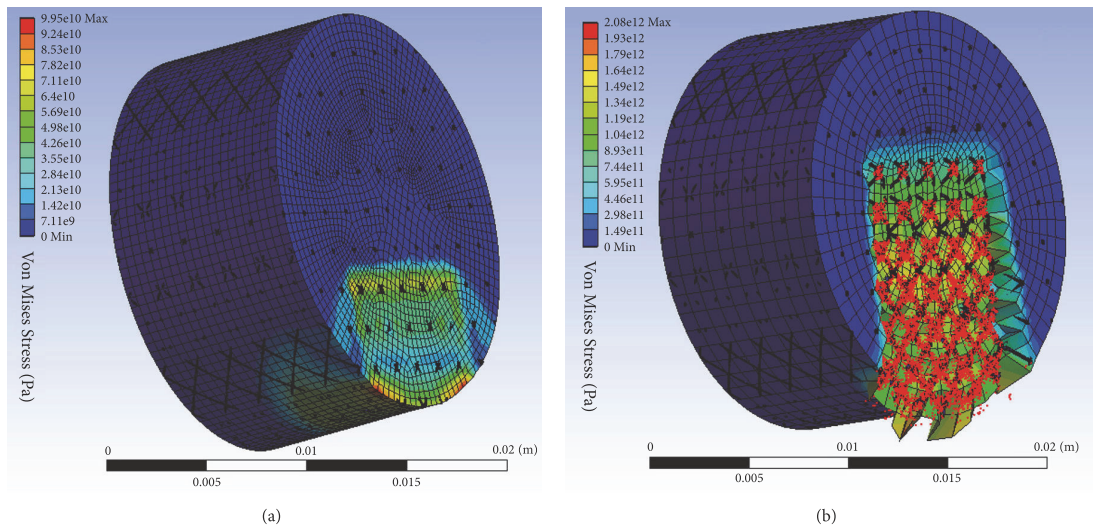


FIGURE 12: Stresses resulting from impact simulation of sample consisting of diamond and Ti6Al4V lattice structure: (a) 1000 J and (b) 5000 J impact energy.

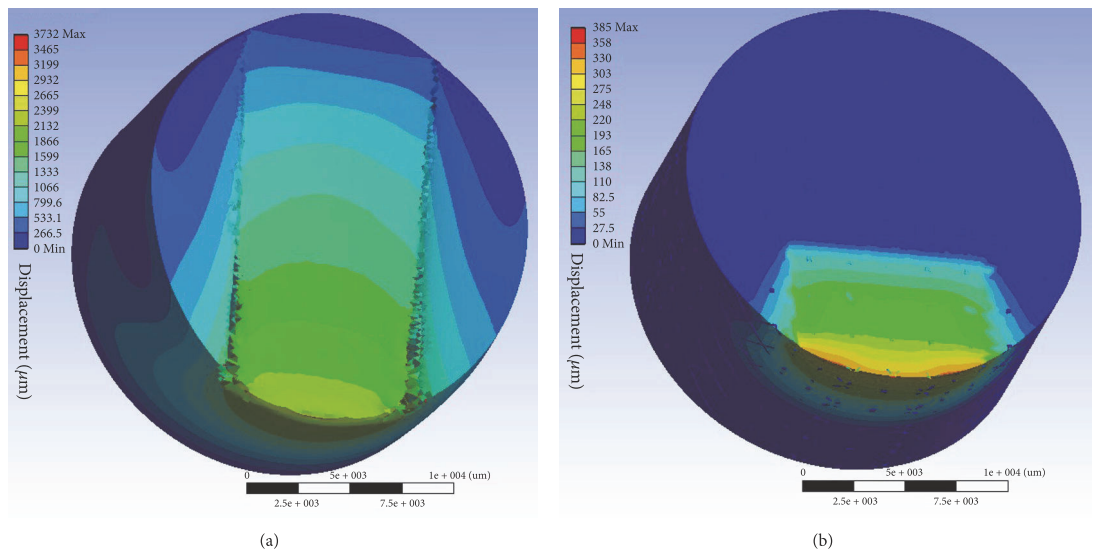


FIGURE 13: Displacement of 1000 J impact simulation of samples: (a) pure diamond and (b) diamond and Ti6Al4V lattice.

sponsors had no role in the design of the study; in the collection, analyses, or interpretation of data; in the writing of the manuscript; and in the decision to publish the results.

Authors’ Contributions

Ramin Rahmani was responsible for methodology, experiments, software analysis, writing, investigation, and visualization; Maksim Antonov was responsible for review, editing,

project administration, and supervision; Lauri Kollo was responsible for experiments, validation, and supervision.

Acknowledgments

The authors would like to thank Heinar Vagiström for the help with surface cleaning of samples via alumina nanoparticles, Rainer Traksmäa for the help with preparation of XRD measurements, and Mart Viljus for the help with

EDS mapping. This research was supported by the Estonian Ministry of Higher Education and Research under Projects (IUT19-29 and ETAG18012) and TTÜ base finance project (B56 and SS427).

- [15] P. Qiao, M. Yang, and F. Bobaru, "Impact mechanics and high-energy absorbing materials: Review," *Journal of Aerospace Engineering*, vol. 21, no. 4, pp. 235–248, 2008.

References

- [1] G. Li, L. Wang, W. Pan et al., "In vitro and in vivo study of additive manufactured porous Ti6Al4V scaffolds for repairing bone defects," *Scientific Reports*, vol. 6, article no 34072, 2016.
- [2] Y. Holovenko, M. Antonov, L. Kollo, and I. Hussainova, "Friction studies of metal surfaces with various 3D printed patterns tested in dry sliding conditions," *Proceedings of the Institution of Mechanical Engineers, Part J: Journal of Engineering Tribology*, vol. 232, no. 1, pp. 43–53, 2018.
- [3] D. F. Grech, S. Abela, M. Attard, and E. Sinagra, "Coating of diamond particles for production of metal matrix composites," *Surface Engineering*, vol. 29, no. 3, pp. 244–246, 2013.
- [4] C. Yan, L. Hao, A. Hussein, P. Young, J. Huang, and W. Zhu, "Microstructure and mechanical properties of aluminum alloy cellular lattice structures manufactured by direct metal laser sintering," *Materials Science & Engineering A*, vol. 628, pp. 238–246, 2015.
- [5] C. Yan, L. Hao, A. Hussein, P. Young, and D. Raymond, "Advanced lightweight 316L stainless steel cellular lattice structures fabricated via selective laser melting," *Materials and Corrosion*, vol. 55, pp. 533–541, 2014.
- [6] Z. A. Munir, U. Anselmi-Tamburini, and M. Ohyanagi, "The effect of electric field and pressure on the synthesis and consolidation of materials: a review of the spark plasma sintering method," *Journal of Materials Science*, vol. 41, no. 3, pp. 763–777, 2006.
- [7] A. Balbo and D. Sciti, "Spark plasma sintering and hot pressing of ZrB_2 - $MoSi_2$ ultra-high-temperature ceramics," *Materials Science and Engineering A*, vol. 475, no. 1-2, pp. 108–112, 2008.
- [8] <http://www.vanmoppes.ch/en/>.
- [9] L. Jaworska, M. Szutkowska, P. Klimczyk et al., "Oxidation, graphitization and thermal resistance of PCD materials with the various bonding phases of up to 800°C," *International Journal of Refractory Metals and Hard Materials*, vol. 45, pp. 109–116, 2014.
- [10] W. Z. Shao, V. V. Ivanov, L. Zhen, Y. S. Cui, and Y. Wang, "A study on graphitization of diamond in copper-diamond composite materials," *Materials Letters*, vol. 58, no. 1-2, pp. 146–149, 2004.
- [11] M. Antonov, R. Veinthal, D.-L. Yung, D. Katušin, and I. Hussainova, "Mapping of impact-abrasive wear performance of WC-Co cemented carbides," *Wear*, vol. 332-333, pp. 971–978, 2015.
- [12] "ASTM G65-04 standard test method for measuring abrasion using the dry sand/rubber wheel apparatus, annual book of ASTM standards," 2004, <https://compass.astm.org/Standards/HISTORICAL/G65-04.htm>.
- [13] T. Borkar and R. Banerjee, "Influence of spark plasma sintering (SPS) processing parameters on microstructure and mechanical properties of nickel," *Materials Science and Engineering: A Structural Materials: Properties, Microstructure and Processing*, vol. 618, pp. 176–181, 2014.
- [14] T. Camus and S. Moubarak, "Maintenance robotics in TBM tunnelling," in *Proceedings of the 32nd International Symposium on Automation and Robotics in Construction and Mining: Connected to the Future, ISARC 2015, Finland, June 2015*.

Publication VI

R. Rahmani; M. Antonov; N. Kamboj; Modelling of impact-abrasive wear of ceramic, metallic, and composite materials, Proceedings of the Estonian Academy of Sciences 68 (2019) 191-197.



Modelling of impact-abrasive wear of ceramic, metallic, and composite materials

Ramin Rahmani*, Maksim Antonov, and Nikhil Kamboj

Department of Mechanical and Industrial Engineering, Tallinn University of Technology, Ehitajate tee 5, 19086 Tallinn, Estonia

Received 25 February 2019, accepted 19 March 2019, available online 23 April 2019

© 2019 Authors. This is an Open Access article distributed under the terms and conditions of the Creative Commons Attribution-NonCommercial 4.0 International License (<http://creativecommons.org/licenses/by-nc/4.0/>).

Abstract. The behaviour of materials was investigated using finite element modelling software (SOLIDWORKS and COMSOL). Three types of materials were studied: (1) ceramic (diamond), (2) metallic (titanium), and (3) composite (consisting of ceramic and metallic phases). Finite element modelling allows illustrating deformation and stressing the distribution of the test material during a single impact of the tribodevice with or without abrasive particles. The impact energy absorption was investigated. Real composite materials were produced by a combination of 3D printing (selective laser melting) of the lattice structure (Ti6Al4V) followed by addition of a hard ceramic phase with the help of the spark plasma sintering technique. The produced samples were tested by a laboratory impact-abrasive tribodevice. The results of modelling and laboratory testing were compared. The effect of modelling variables is illustrated. It is explained why composite materials showed better performance in impact-abrasive conditions and are suitable for tunnelling and mining applications.

Key words: additive manufacturing, spark plasma sintering, selective laser melting, impact-abrasive simulation, SOLIDWORKS software, COMSOL software, diamond–Ti6Al4V composite.

1. INTRODUCTION

Combination of computer-aided design (CAD), finite element analysis, and 3D printing of metal alloys is a high-potential additive manufacturing approach converting conventional metallurgy to modern powder metallurgy. Focus on the simulation of prototypes and experiments can lead to better results and reduced costs of manufacturing, e.g. sintering or consolidation of material powders and printer parameters as well as compressive, tensile, impact, and abrasion tests. The influence of scanning strategies (hatching and concentric) and printer parameters (laser power and pulse duration) of CoCr alloy powders for stent placement feasibility in cardiology has resulted in selective laser melting (SLM) [1]. Advantages of concentric scanning for having a fine

mesh and also electrochemical polishing for post-processing are shown in this study. Manufacturability of the gyroid- and diamond-type triply periodic minimal surface (TPMS) scaffold design for biomaterials (bone implant) application is investigated in [2]. Visual and quantifiable comparisons by 3D reconstructed and 3D CAD modelled Ti6Al4V TPMS lattices show an acceptable reproduction design. Compressive strength, stress/strain distribution, and the failure occurrence mechanisms of cellular structures can be successfully analysed by the finite element method [3].

A nonlinear transient (thermo-mechanical field) model is developed via the ANSYS parametric design language (APDL) in [4]. This finite element analysis considers temperature and stress fields caused by the overhanging and floating of a 316L stainless steel layer built in a powder bed without support.

* Corresponding author, ramin.rahmaniahranjani@ttu.ee

Lightweight metallic TPMS sheets/shells (primitive, diamond, and gyroid) are fabricated by SLM and compared to body-centred cubic lattices in [5]. Simulation results illustrate uniform stress distributions for diamond- and gyroid-type lattices under compression loading. The powder spreading/distribution process is an important research field in additive manufacturing. Some simulations in this area to illustrate induced flow, velocity, solidification or discontinuous track, and temperature contours of particles in solid bed have been developed [6,7].

In this work, the modelling ability of SOLIDWORKS and COMSOL software is introduced for prototype samples under impact and abrasive loadings [8–10]. The combination of SLM (for metallic lattice) and spark plasma sintering (SPS, for reinforcing by diamond) techniques is used for preparing an optimized sample.

2. MATERIALS, MACHINES, AND METHODS

Various Ti6Al4V cellular lattice structures were modelled by SOLIDWORKS software. These can be fabricated via SLM or 3D printing (Figs 1 and 2). A BCC-type 1 mm unit cell (diamond-type) lattice structure (Figs 1A

and 2A) was printed by *Realizer SLM50* metal printer from Ti6Al4V powder in the size of 20–63 μm (supplied by SLM Solution Group) and are studied in the current work. A *FCT Systeme* SPS machine was used for adding diamond particles with the size of 40–50 μm (supplied by Vanmoppes & Sons Ltd), which filled the space between the lattice structure (Fig. 3). Wear resistance and damage tolerance of the Ti6Al4V–diamond composite were evaluated via a custom-made patented impact-abrasive tribology tester in Tallinn University of Technology [8] (Fig. 4A). During the real testing, the WC-15Co rotating wheel was driven by an electrical motor, but in the current simulation study only an impact generator was used with 1 m/s velocity and range of impact energy (Fig. 4B). The abrasive was introduced into the region between the wheel and the sample by a nozzle. The wheel diameter was 100 mm, and the cylindrical sample was modelled to be of 20 mm diameter and 10 mm height.

COMSOL software was applied for stress and displacement simulation. The surface stress distribution and deformation of the solid diamond sample with a single impact (without the abrasive particle) in the centre is shown in Fig. 5. Figure 6 illustrates the diamond

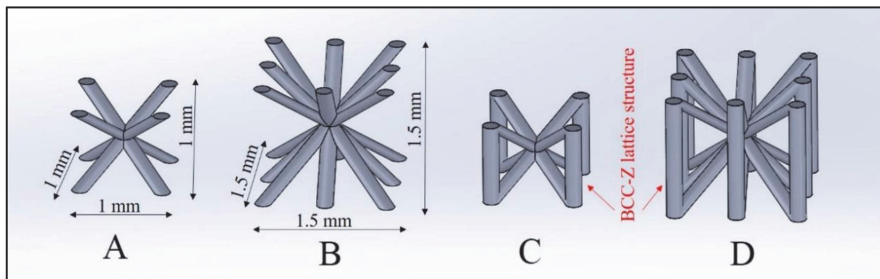


Fig. 1. Lattice structure design: (A) body-centred cubic (BCC) (diamond-type) lattice, 1 mm unit cell; (B) BCC, 1.5 mm unit cell; (C) body-centred cubic with vertical scaffolds (BCC-Z), 1 mm unit cell; (D) BCC-Z, 1.5 mm unit cell.

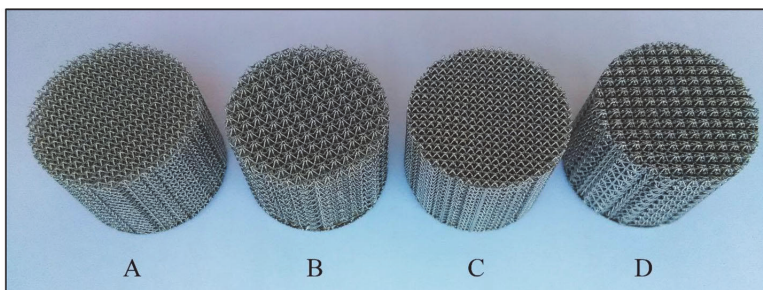


Fig. 2. Examples of cellular lattice structures: (A) BCC, 1 mm unit cell; (B) BCC, 1.5 mm unit cell; (C) BCC-Z, 1 mm unit cell; (D) BCC-Z, 1.5 mm unit cell (dimensions of printed objects are diameter 20 mm and height 15 mm).

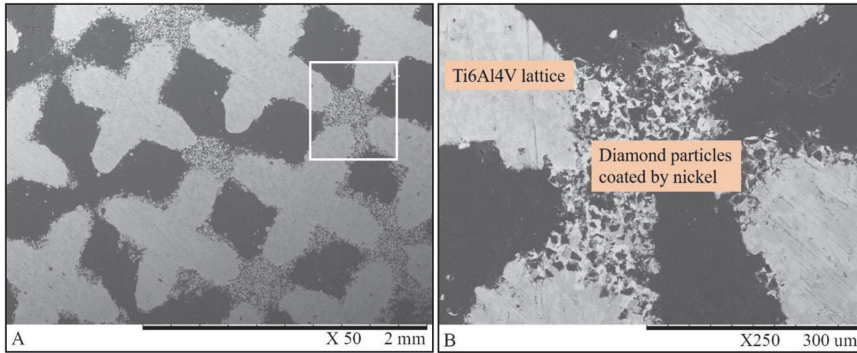


Fig. 3. SEM micrograph of diamond-Ti6Al4V sample after SPS and polishing.

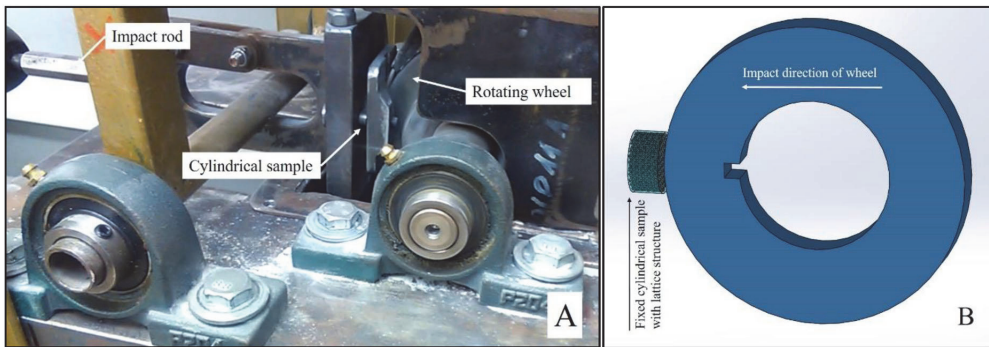


Fig. 4. (A) Position of the sample, wheel, and rod of the impacting device; (B) simulation mechanism; only horizontal impact motion [8,9].

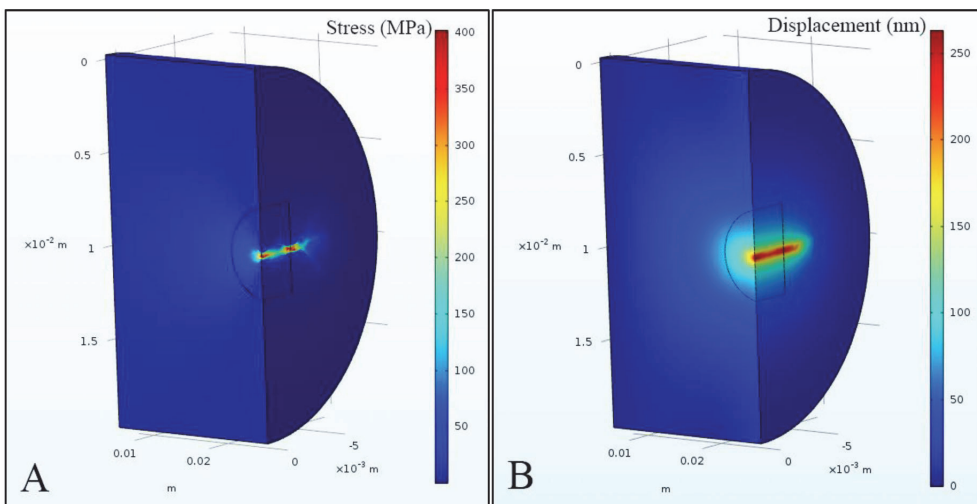


Fig. 5. (A) Stress and (B) deformation resulting from impact simulation of a solid diamond (without the abrasive particle).

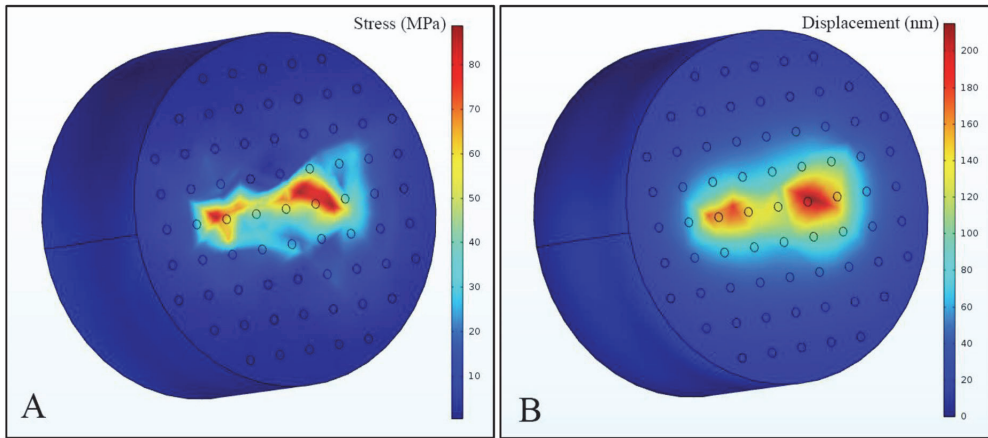


Fig. 6. (A) Stress and (B) deformation resulting from the impact simulation of the diamond embedded lattice structure (without the abrasive particle).

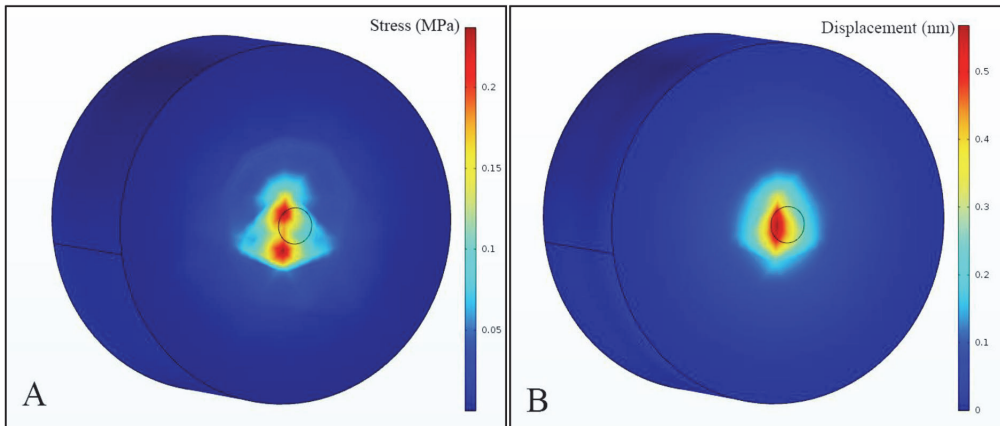


Fig. 7. (A) Stress and (B) deformation resulting from the impact simulation of a solid diamond in contact with the abrasive particle.

sample reinforced by a Ti6Al4V lattice structure. The modelling of the impact of the SiO₂ abrasive particle with a diameter of 2 mm, trapped between the wheel and the sample, is depicted in Fig. 7.

3. RESULTS AND DISCUSSION

Three simulations of composite samples were considered for the assessment of wear resistance, impact energy absorption, and damage tolerance, respectively, of a solid diamond, a diamond embedded Ti6Al4V

lattice structure, and a diamond in contact with a SiO₂ abrasive particle. The von Mises equivalent stress distribution and displacement of samples are shown in Figs 5–7. For the solid diamond, symmetry of the model is used to save time and to obtain a finer mesh configuration (Fig. 8). However, in the two next simulations, a complete model was preferred for consideration because of the boundary condition of the lattice and the sample and the triply contact of the wheel/sample/particle. The possibility of applying a wide range of metals, ceramics, and composites, different diameters and shapes of the samples and abrasive particles, and varied velocity/

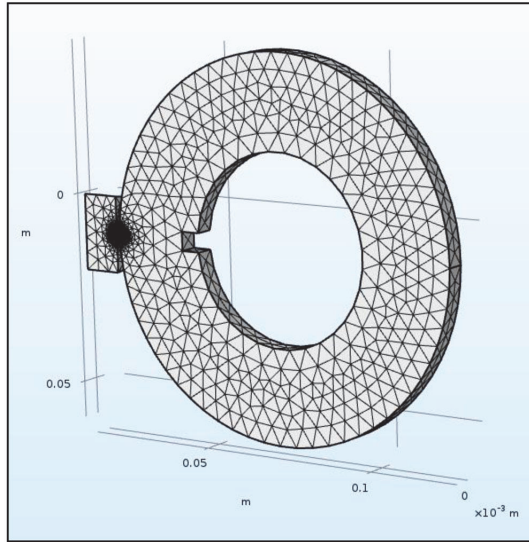


Fig. 8. Mesh configuration of symmetry of the model with a finer mesh in the contact region.

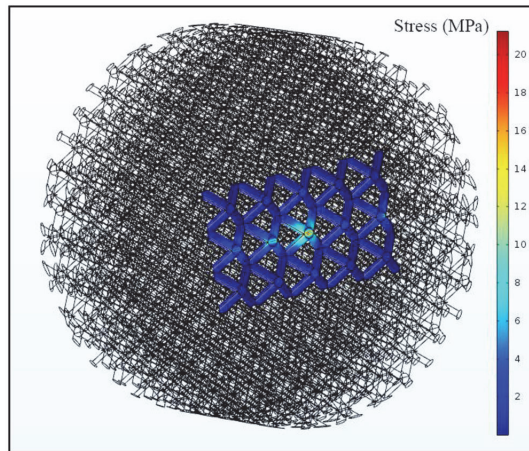


Fig. 9. Stress distribution of the lattice structure under impact in the contact region.

energy of impact and using finite element is an advantage of this method. Horizontal and linear distribution of the stress/deformation is the reason of the cracking/splitting of solid diamond samples under high impact rates (see Fig. 5).

The pivotal role of the lattice structure in impact absorption and in increasing damage tolerance is con-

sidered in Figs 6 and 9. Comparison of Figs 5 and 6 demonstrates a significant reduction of stress in the solid sample. Figures 10–12 illustrate statistical comparison of solid diamond and diamond embedded Ti6Al4V lattice. Either decrease of stress and deformation or increase of impact energy absorption is clear in the graphs.

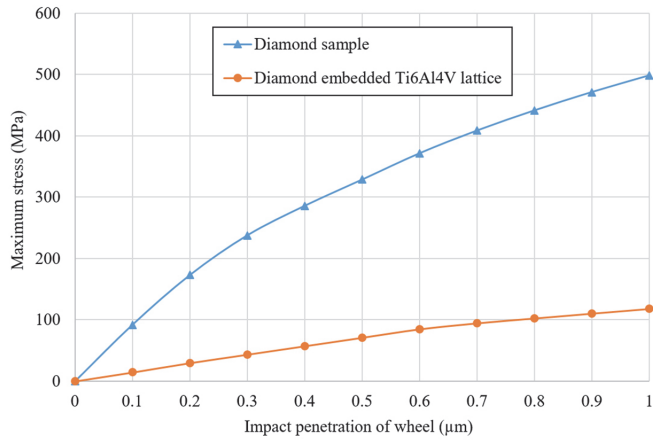


Fig. 10. Comparison of maximum stress of diamond and diamond–Ti6Al4V samples during impacting.

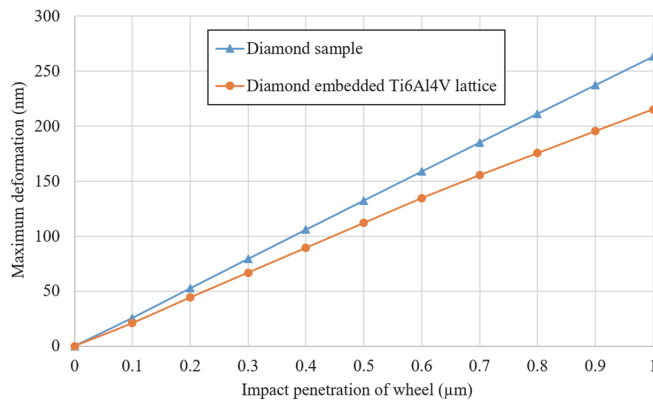


Fig. 11. Comparison of maximum deformation of diamond and diamond–Ti6Al4V samples during impacting.

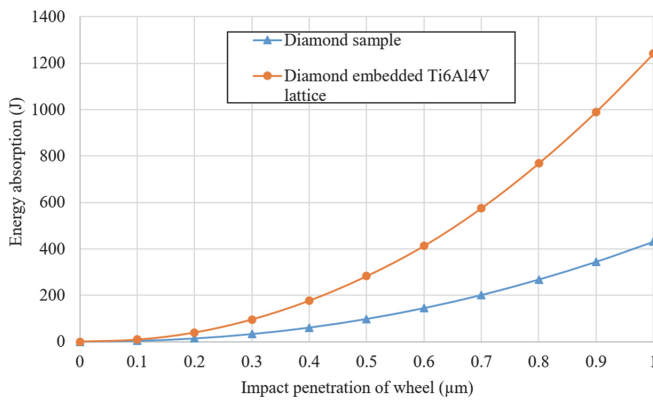


Fig. 12. Comparison of energy absorption of diamond and diamond–Ti6Al4V samples during impacting.

4. CONCLUSIONS

This study describes three cases of the simulation of impact-abrasive wear, namely, of solid diamond, Ti6Al4V lattice structure with diamond, and diamond in contact with an abrasive particle. Combination of laser melting and spark plasma sintering is a novel method, which can be considered for any kind of ceramics and composites.

- SOLIDWORKS and COMSOL finite element software help to design samples for 3D printing and to predict the behaviour of composite materials (deformation and stress distribution) before production. All steps of the additive manufacturing process starting from design, 3D metal printing, impact-abrasive tests, and custom-made modelling can be improved with the help of finite element simulation.
- Metallic lattice performs as an impact absorption structure to decrease local stress/deformation and delays plastic deformation in comparison with the lattice-free sample. Use of the cellular lattice structure decreases downtime required for changing parts due to improved wear resistance.
- It was found that traditional powder metallurgy can be substituted by a combination of SLM and SPS methods to produce wear-resistant parts for impact-abrasive applications. More than four times reduction of the stress level in the diamond sample was achieved as a result of applying the Ti6Al4V lattice structure.

ACKNOWLEDGEMENTS

This research was supported by the Estonian Ministry of Education and Research under projects IUT19-29 and ETAG18012 and by base finance project B56 and SS427 of Tallinn University of Technology. The publication costs of this article were covered by the Estonian Academy of Sciences.

REFERENCES

1. Demir, A. G. and Previtali, B. Additive manufacturing of cardiovascular CoCr stents by selective laser melting. *Mater. Design*, 2017, **119**, 338–350.
2. Yan, C., Hao, L., Hussein, A., and Young, P. Ti-6Al-4V triply periodic minimal surface structures for bone implants fabricated via selective laser melting. *J. Mech. Behav. Biomed. Mater.*, 2015, **51**, 61–73.
3. Yang, L., Yan, C., Han, C., Chen, P., Yang, S., and Shi, Y. Mechanical response of a triply periodic minimal surface cellular structures manufactured by selective laser melting. *Int. J. Mech. Sci.*, 2018, **148**, 149–157.
4. Hussein, A., Hao, L., Yan, C., and Everson, R. Finite element simulation of the temperature and stress fields in single layers built without-support in selective laser melting. *Mater. Design*, 2013, **52**, 638–647.
5. Zhang, L., Feih, S., Daynes, S., Chang, S., Wang, M. Y., Wei, J., and Lu, W. F. Energy absorption characteristics of metallic triply periodic minimal surface sheet structures under compressive loading. *Addit. Manuf.*, 2018, **23**, 505–515.
6. Haeri, S., Wang, Y., Ghita, O., and Sun, J. Discrete element simulation and experimental study of powder spreading process in additive manufacturing. *Powder Technol.*, 2016, **306**, 45–54.
7. Khairallah, S. A. and Anderson, A. Mesoscopic simulation model of selective laser melting of stainless steel powder. *J. Mater. Process. Tech.*, 2014, **214**, 2627–2636.
8. Antonov, M., Veinthal, R., Yung, D. L., Katušin, D., and Hussainova, I. Mapping of impact-abrasive wear performance of WC–Co cemented carbides. *Wear*, 2015, **332**, 971–978.
9. Rahmani, R., Antonov, M., and Kollo, L. Wear resistance of (diamond-Ni)-Ti6Al4V gradient materials prepared by combined selective laser melting and spark plasma sintering techniques. *Adv. Tribol.*, 2019, article ID 5415897.
10. Badisch, E., Ilo, S., and Polak, R. Multivariable modeling of impact-abrasion wear rates in metal matrix-carbide composite materials. *Tribol. Lett.*, 2009, **36**, 55–62.

Keraamiliste, metsete ja komposiitmaterjalide abrasiivkulumise modelleerimine

Ramin Rahmani, Maksim Antonov ja Nikhil Kamboj

Käesolevas uuringus oli vaatluse all materjalide käitumine, kasutades lõplike elementide modelleerimise tarkvara (SOLIDWORKS ja COMSOL). Uuriti kolme liiki materjale: 1) keraamika (teemant), 2) metall (titaan) ja 3) komposiit (keraamilis-metallne). Modelleerimine lõplike elementide meetodil võimaldab näidata deformatsiooni ja pingete jaotust uuritavas materjalis üksiklöögi toimel triboseadmes abrasiivosakesega ning ilma. Uuriti löögienergia neeldumist. Reaalsed materjalid olid valmistatud titaanisulamist Ti6Al4V võrestruktuuri 3D printimise ja sellesse järgneva kõva keraamikafaasi lisandamisega sädeplasma paagutuse teel. Valmistatud proovikehi katsetati laboratoorsel lõökabrasiivtriboseadmel. Võrreldi modelleerimise ja laboratoorsete katsetuste tulemusi. Muutujate mõju modelleerimisel on illustreeritud vastavate diagrammidega. On välja selgitatud, miks komposiitmaterjalidel on lõökabrasiivkulumise tingimustes parem vastupanu ja on sobivad kasutamiseks tunneliehituses ning kaevandamisel.

Curriculum Vitae

Personal data

Name: Ramin Rahmani Ahranjani

Date of Birth: 22.09.1982

Place of Birth: Iran

Contact data

ramin.rahmaniahranjani@taltech.ee, +372 519 88504

ramin.rahmaniahranjani@gmail.com, +98 911 343 5043

Education

2016 – 2020 Tallinn University of Technology – PhD

2005 – 2007 Kashan University – MSc

2000 – 2004 Guilan University – BSc

Language competence

Persian – Fluent

English – Fluent

Turkish – Fluent

Estonian – Basic

German – Basic

Arabic – Basic

Projects

IUT19-29: “Multistage structured ceramic-based composite materials for use in extreme conditions (1.01.2014-31.12.2019)”, Jakob Kübarsepp, Tallinn University of Technology, Faculty of Mechanical Engineering, Tallinn University of Technology, Faculty of Engineering, Department of Mechanical and Industrial Engineering.

ETAG18012: “Ultra-durable ceramic composites for wear-resistant cutting tools (1.09.2018-31.08.2021)”, Maksim Antonov, Tallinn University of Technology, Faculty of Engineering, Department of Mechanical and Industrial Engineering.

Elulookirjeldus

Isikuandmed

Nimi: Ramin Rahmani Ahranjani
Sünniaeg: 22.09.1982
Sünnikoht: Iraan

Kontaktandmed

ramin.rahmaniahranjani@taltech.ee, +372 519 88504
ramin.rahmaniahranjani@gmail.com, +98 911 343 5043

Hariduskäik

2016 – 2020 Tallinna Tehnikaülikool – PhD
2005 – 2007 Kashani ülikool – MSc
2000 – 2004 Guillani ülikool – BSc

Keelteoskus

Pärsia – Kõrgtase
Inglise keel – Kõrgtase
Türgi keel – Kõrgtase
Eesti keel – Kesktase
Saksa keel – Kesktase
Araabia keel – Kesktase

Projektid

IUT19-29: “Mitmeastmelised struktureeritud keraamilistel komposiitmaterjalidel kasutamiseks äärmuslikes tingimustes (1.01.2014–31.12.2019)”, Jakob Kübarsepp, Tallinna Tehnikaülikool, Tallinna Tehnikaülikooli mehaanikateaduskond, ehitusteaduskond, Masinaehituse ja tööstustehnoloogia osakond.

ETAG18012: “Eriti vastupidavad keraamilised komposiidid kulumiskindlatele lõikeriistadele (1.09.2018–31.08.2021)”, Maksim Antonov, Tallinna Tehnikaülikool, ehitusteaduskond, mehaanika- ja tööstustehnoloogia osakond.